



# Durham E-Theses

---

## *Perturbative Corrections in SHERPA*

HALL, OLIVER,ALEXANDER

### How to cite:

---

HALL, OLIVER,ALEXANDER (2014) *Perturbative Corrections in SHERPA*, Durham theses, Durham University. Available at Durham E-Theses Online: <http://etheses.dur.ac.uk/10557/>

### Use policy

---

The full-text may be used and/or reproduced, and given to third parties in any format or medium, without prior permission or charge, for personal research or study, educational, or not-for-profit purposes provided that:

- a full bibliographic reference is made to the original source
- a [link](#) is made to the metadata record in Durham E-Theses
- the full-text is not changed in any way

The full-text must not be sold in any format or medium without the formal permission of the copyright holders.

Please consult the [full Durham E-Theses policy](#) for further details.

# Perturbative Corrections in SHERPA

Oliver Hall

A Thesis presented for the degree of  
Doctor of Philosophy



Institute for Particle Physics Phenomenology  
Department of Physics  
University of Durham  
England

September 2013

# Perturbative Corrections in SHERPA

Oliver Hall

Submitted for the degree of Doctor of Philosophy

September 2013

## Abstract

The use of Monte Carlo event generators for the simulation of LHC collider experiments, has in recent years driven a demand for greater accuracy of predictions in such generators. This thesis will be concerned with the addition of certain perturbative corrections in the event generator SHERPA.

In this vein a framework for the automatic calculation of the real correction terms is presented, based on the subtraction mechanism of Frixione, Kunszt and Signer. This resulting framework is implemented in the matrix element generator AMEGIC++, which will then allow the calculation of the real components of an NLO QCD for any process; this can be supplemented with virtual corrections to provide a full NLO QCD prediction. This implementation is then rigorously tested and found to be consistent with known NLO results.

This subtraction framework is then utilized to perform a series of tests on the relative efficiency of the FKS and Catani Seymour subtraction methods; these tests are conducted over multiple processes and the affect of the multiplicity of the state is investigated.

In addition the contribution of photon induced processes to lepton and  $W$  boson production is discussed, taking into account contributions from the QED part of parton distribution functions and from equivalent photons in the Weizsaecker–Williams approximation. Typically these processes contribute on the per cent level compared to standard quark and gluon-induced processes; however, when applying various cuts this picture may change and the photon induced processes may become significant.

# Declaration

The work in this thesis is based on research carried out at the Institute for Particle Physics Phenomenology, the Department of Physics, Durham, England. The work in this thesis was carried out in collaboration with Professor Frank Krauss, my supervisor. Parts of this thesis therefore either will be seen or have been seen previously:

- The majority of work in part II of this thesis is in preparation as:  
O.Hall, F.Krauss, and M.Schoenherr *Photon-induced production processes at hadron colliders with SHERPA*

No part of this thesis has been submitted elsewhere for any other degree or qualification and it is all my own work unless referenced to the contrary in the text.

**Copyright © 2013 by Oliver Hall.**

“The copyright of this thesis rests with the author. No quotations from it should be published without the author’s prior written consent and information derived from it should be acknowledged”.

# Acknowledgements

I would like to begin by thanking my supervisor Frank Krauss for his time and patience over these four years, without which none of this could have occurred. I also extend my gratitude to Marek Schoenherr and other collaborators and within SHERPA for their generous support. I would also like to thank my fellow denizens of OC118, particularly Steven Wells, Daniel Busbridge and Matthew Yip for many useful (and not so useful) and stimulating discussions as well as Jonathan Davis for his help with various technical issues. Additionally I would like to thank Dr. Daniel Farrow for his good humour and many accounts of his battles with Pan-STARRS, both of which have been a consistent source of amusement. Finally I wish to thank my father Stephen Hall for his care in reading this thesis, and his timeless ability to discern where a semi-colon ought to appear.

# Contents

<b>Abstract</b>	<b>ii</b>
<b>Declaration</b>	<b>iii</b>
<b>Acknowledgements</b>	<b>iv</b>
<b>I NLO Calculations in SHERPA</b>	<b>2</b>
<b>1 The Foundations of QCD</b>	<b>5</b>
1.1 QCD as a Gauge Theory . . . . .	5
1.2 Renormalisation of QCD . . . . .	8
1.3 Unresolved Limits of QCD Matrix Elements . . . . .	13
1.3.1 Notation . . . . .	13
1.3.2 Explicit Expressions . . . . .	14
1.4 Collider Physics and the QCD Parton Model . . . . .	17
1.4.1 Naïve Parton Model . . . . .	17
1.4.2 The Parton Model and QCD . . . . .	18
1.5 Jet Algorithms . . . . .	21
1.5.1 Infrared Safety . . . . .	22
1.5.2 Generalised $k_T$ Clustering Algorithms . . . . .	23
<b>2 Next-to Leading Order Calculations</b>	<b>25</b>
2.1 Motivation . . . . .	25
2.2 Schematics of NLO calculations . . . . .	28

---

2.3	Virtual Contributions . . . . .	29
2.4	Real Emission Contributions . . . . .	31
2.5	PDFs and Partonic Cross Sections at NLO . . . . .	33
2.6	Subtraction . . . . .	34
2.6.1	Overview of Catani Seymour Dipoles . . . . .	36
<b>3</b>	<b>Review of FKS Subtraction</b>	<b>40</b>
3.1	Structure of FKS subtraction . . . . .	41
3.2	Constructing the Subtraction Terms . . . . .	43
3.3	Real Subtraction Terms . . . . .	46
3.3.1	Soft Term . . . . .	48
3.3.2	Collinear Term . . . . .	49
3.3.3	Soft Collinear Term . . . . .	50
3.4	Integrated terms . . . . .	50
3.4.1	Soft Term . . . . .	51
3.4.2	Final state collinear terms . . . . .	52
3.4.3	Initial state collinear term . . . . .	53
<b>4</b>	<b>Implementation</b>	<b>55</b>
4.1	Partitioning Functions . . . . .	56
4.1.1	Some efficiencies . . . . .	57
4.2	Integrated Terms . . . . .	58
4.2.1	Initial state terms . . . . .	59
4.3	Real Subtraction Terms . . . . .	61
4.3.1	Organisation of the Calculation . . . . .	61
4.3.2	Kinematics . . . . .	62
4.3.3	Final State Collinear Map . . . . .	64
4.3.4	Initial State Soft map . . . . .	66
4.3.5	Final State soft map . . . . .	69
4.3.6	Initial state Collinear map . . . . .	71
4.4	Technical Cutoff . . . . .	73

<b>Contents</b>	<b>vii</b>
4.5 Tests of the Implementation . . . . .	74
4.5.1 Parameter Variation . . . . .	74
4.5.2 Convergence test for Subtraction Terms . . . . .	81
4.5.3 Comparison with Catani Seymour Cross Sections . . . . .	82
<b>5 Comparison with Catani Seymour</b>	<b>84</b>
5.1 Comparison of the Subtraction Terms . . . . .	84
5.2 Results . . . . .	87
<b>6 Conclusions to Part I</b>	<b>97</b>
<b>II Simulating Photon Induced Processes</b>	<b>99</b>
<b>7 Simulating Processes in SHERPA</b>	<b>103</b>
7.1 Event Generation in SHERPA . . . . .	103
7.2 Parton Showers . . . . .	104
7.2.1 Parton Showering in SHERPA . . . . .	110
7.2.2 NLO calculations and Parton Showers . . . . .	113
7.2.3 Merging Matrix Elements with Parton Showers . . . . .	118
7.3 Hadronisation in SHERPA . . . . .	121
<b>8 Photon Induced Processes</b>	<b>122</b>
8.1 Photon PDFs . . . . .	122
8.1.1 QED Corrections to Parton Showering . . . . .	125
8.2 Equivalent Photon Approximation . . . . .	126
<b>9 Photon Induced Processes Results</b>	<b>128</b>
9.1 Lepton-pair production . . . . .	129
9.1.1 Inclusive lepton pair production . . . . .	129
9.1.2 Jet activity . . . . .	133
9.2 $W$ -pair production . . . . .	134
9.2.1 ATLAS analysis . . . . .	135

---

9.2.2 High-mass tail . . . . .	140
<b>10 Conclusions to Part II</b>	<b>144</b>
<b>Appendix</b>	<b>145</b>
<b>A Details of the Experimental Analyses</b>	<b>146</b>
A.1 ATLAS $WW$ Analysis [1] . . . . .	146
A.2 CMS Drell-Yan Analysis [2,3] . . . . .	149
A.3 Drell-Yan ATLAS Analysis [4] . . . . .	149
A.4 Lepton Pair Jet Analysis . . . . .	150
<b>B FKS Expressions</b>	<b>152</b>
B.1 Massive Partons in the Integrated Soft Term . . . . .	152
B.2 The Reduced Matrix element from Collinear Limits . . . . .	153

# List of Figures

1.1	The one loop Feynman diagrams contributing to the self energy of quarks and gluons . . . . .	9
2.1	Scale Errors shown for LO and NLO for Drell Yan mass peak . . . . .	27
2.2	One loop diagram representing the virtual contribution at NLO of the process $q\bar{q} \rightarrow \gamma^*$ . . . . .	29
4.1	The variation of the NLO cross section for $e^+e^- \rightarrow jj$ as calculated by the FKS implementation with the soft cutoff parameter $\xi_{\text{cut}}$ . The Integrated and Real terms are plotted separately to display their variation	75
4.2	The variation of the NLO cross section for $e^+e^- \rightarrow jj$ as calculated by the FKS implementation with the collinear cutoff parameter $Y_{\text{cut}}$ . The Integrated and Real terms are plotted separately to display their variation . . . . .	76
4.3	The variation of the NLO cross section for $e^+e^- \rightarrow jjj$ as calculated by the FKS implementation with the soft cutoff parameter $\xi_{\text{cut}}$ . The Integrated and Real terms are plotted separately to display their variation . . . . .	77
4.4	The variation of the NLO cross section for $e^+e^- \rightarrow jjj$ as calculated by the FKS implementation with the collinear cutoff parameter $Y_{\text{cut}}$ . The Integrated and Real terms are plotted separately to display their variation . . . . .	78

- 
- 4.5 The variation of the NLO cross section for  $jj \rightarrow e^+e^-$  as calculated by the FKS implementation with the soft cutoff parameter  $\xi_{\text{cut}}$ . The Integrated and Real terms are plotted separately to display their variation 79
- 4.6 The variation of the NLO cross section for  $jj \rightarrow e^+e^-$  as calculated by the FKS implementation with the collinear cutoff parameter  $Y_{\text{cut}}$ . The Integrated and Real terms are plotted separately to display their variation . . . . . 80
- 4.7 The subtracted real term,  $\sigma^{(RS)}$  calculated for the process  $e^+e^- \rightarrow jj$  in FKS for different numerical cutoff values,  $\alpha_{\text{min}}$ , in the integration. FKS cutoff parameters,  $\xi_{\text{cut}}$  and  $Y_{\text{cut}}$  set to 1,2 respectively such that only phase space cuts are the result of  $\alpha_{\text{min}}$ . . . . . 81
- 4.8 The subtracted real term,  $\sigma^{(RS)}$  calculated for the process  $jj \rightarrow e^+e^-$  in FKS for different numerical cutoff values,  $\alpha_{\text{min}}$ , in the integration. FKS cutoff parameters,  $\xi_{\text{cut}}$  and  $Y_{\text{cut}}$  set to 1,2 respectively such that only phase space cuts are the result of  $\alpha_{\text{min}}$ . . . . . 82
- 5.1 The number of function calls for the integration of  $\sigma^{(RS)}$  to 0.1% accuracy for the process  $e^+e^- \rightarrow jj$  for both FKS and Catani Seymour. These are shown against the FKS soft and collinear cutoff parameters  $\xi_{\text{cut}}$  and  $Y_{\text{cut}}$ . . . . . 89
- 5.2 The number of function calls for the integration of  $\sigma^{(RS)}$  to 1% accuracy for the process  $jj \rightarrow e^+e^-$  for both FKS and Catani Seymour. These are shown against the FKS soft and collinear cutoff parameters  $\xi_{\text{cut}}$  and  $Y_{\text{cut}}$ . . . . . 90
- 5.3 The number of function calls for the integration of  $\sigma^{(RS)}$  to 1% accuracy for the process  $e^+e^- \rightarrow jjj$  for both FKS and Catani Seymour. These are shown against the FKS soft and collinear cutoff parameters  $\xi_{\text{cut}}$  and  $Y_{\text{cut}}$ . . . . . 91

- 
- 5.4 The number of function calls for the integration of  $\sigma^{(RS)}$  to 1% accuracy for the process  $e^+e^- \rightarrow jjjj$  for both FKS and Catani Seymour. These are shown against the FKS soft and collinear cutoff parameters  $\xi_{\text{cut}}$  and  $Y_{\text{cut}}$ . . . . . 92
- 5.5 The real subtraction calculated in the Catani Seymour subtraction scheme, calculated with  $\alpha_{\text{dip}} \in \{1, 0.1\}$  . . . . . 93
- 9.1 Invariant lepton-pair mass spectra as measured by ATLAS [4] (left, and for  $ee$  final states) and by CMS [2] (right, and for lepton-lepton final states). The experimental data is compared with SHERPA simulations, starting from a baseline QCD sample simulated with the MC@NLO implementation in SHERPA (black); the QED PDF (green and blue) and EPA (red) contributions are successively added. . . . . 130
- 9.2 Invariant lepton-pair mass spectra as measured by CMS [3] (left for  $ee$ , right for  $\mu\mu$  final states). The experimental data is compared with SHERPA simulations, starting from a baseline QCD sample simulated with the MC@NLO implementation in SHERPA (black); the QED PDF (green and blue) and EPA (red) contributions are successively added. 131
- 9.3 Average number of jets emitted per mass bin for Drell-Yan Process The SHERPA simulations, starting from a baseline QCD sample simulated with the MENLOPS implementation in SHERPA (black); the QED PDF (green and blue) and EPA (red) contributions are successively added. 134
- 9.4 The normalised fiducial differential  $WW$  cross section as a distribution in leading lepton  $p_{\perp}$  as measured by [5]. The experimental data is compared with SHERPA simulations, starting from a baseline QCD sample simulated with the MC@NLO implementation in SHERPA (black); the QED PDF (green and blue) and EPA (red) contributions are successively added. . . . . 138

- 
- 9.5 Distribution of  $WW$  production events for leading lepton transverse momentum and the azimuthal decorrelation of the lepton pair as measured by [5] (left for  $p_{\perp}$ , right for  $\phi_u$ ). The experimental data is compared with SHERPA simulations, starting from a baseline QCD sample simulated with the MC@NLO implementation in SHERPA (black); the QED PDF (green and blue) and EPA (red) contributions are successively added. . . . . 139
- 9.6 Differential cross section for  $WW$  production with respect to the transverse momentum (left) and invariant mass (right) of the lepton pair, simulated at 14 TeV with an analysis framework consistent with [5]. The SHERPA simulations, starting from a baseline QCD sample simulated with the MC@NLO implementation in SHERPA (black); the QED PDF (green and blue) and EPA (red) contributions are successively added. . . . . 141
- 9.7 Ratio of 1-jet to 0-jet rates in  $WW$  production, shown as a distribution transverse momentum (left) and invariant mass (right) of the lepton pair and simulated at 14 TeV with an analysis framework consistent with [5]. The SHERPA simulations, starting from a baseline QCD sample simulated with the MC@NLO implementation in SHERPA (black); the QED PDF (green and blue) and EPA (red) contributions are successively added. . . . . 142

# List of Tables

4.1	The Born and real components of the NLO cross sections calculated with the Catani-Seymour and FKS implementations within AMEGIC++ [6], which in each case has been run with one million events. . . . .	83
A.1	A summary of pseudorapidity and $p_{\perp}$ cuts on leptons as described in ATLAS analysis [1] . . . . .	147
A.2	Isolation criteria on leptons as described in ATLAS analysis [1]. All isolation criteria are taken within a cone of radius $\Delta R < 0.3$ . . . . .	147
A.3	Summary of cuts on jet pseudorapidity and transverse momentum in addition to the jet veto requirements from ATLAS analysis [1] . . . . .	148
A.4	Summary of channel specific cuts on the mass of lepton pairs and relative missing energy from ATLAS analysis [1] . . . . .	148
A.5	Isolation criteria on leptons as described in CMS analyses [2] and [3]. All isolation criteria are taken within a cone of radius $\Delta R < 0.3$ . . . . .	149
A.6	Summary of pseudorapidity and $p_{\perp}$ cuts on electrons as described by the ATLAS analysis [4] . . . . .	150

# Introduction

The threshold of high energy physics is currently being pushed back by experiments at the LHC at CERN. This has enabled discoveries at the high energy frontier, including what appears to be the long elusive Higgs boson. Such discoveries are made possible by a wealth of theoretical work that enables the accurate modelling of desired signals and backgrounds.

The modelling of such effects for collider purposes is incorporated into programs known collectively as Monte Carlo event generators. These provide the link between experiments such as the LHC and the theoretical community, with their ability to provide simulations of collider events. Such tools are used extensively for the analysis and interpretation of collider data, in addition to the determination of experimental signatures of new theoretical models. This thesis is focused on development for and use of the event generator SHERPA.

The fundamental task of a Monte Carlo event generator is to provide predictions for events seen in colliders, as such it must predict what is measured experimentally. The fundamental experimental quantity to compute in a collider environment is a cross section,  $\sigma$ , which can be measured, for a given process, as the number of events over the integrated luminosity (total number of particles per unit area); this is expressed as  $\sigma = \frac{N}{L}$ . To undertake this task a Monte Carlo must utilize a mixture of fundamental physical theory and phenomenological models, the stages of this modelling can be seen in the figure given below. The first of these is to employ cross section calculations of fundamental, free particles. These are based on the matrix element of the desired process, which is computed using quantum field theory. The

cross section is then calculated, in essence, by performing a phase space integral of the squared matrix element over all the final state momenta of the process with the constraint of momentum conservation between initial and final states; this is expressed below

$$\sigma_{ab \rightarrow X}(p_1, p_2) = \frac{1}{2E_1 E_2} \prod_i \int \frac{d^3 k_i}{(2\pi)^3} \frac{1}{2E_i} (2\pi)^4 \delta^{(4)}(p_1 + p_2 - \sum_i k_i) |\mathcal{M}(ab \rightarrow X)|^2$$

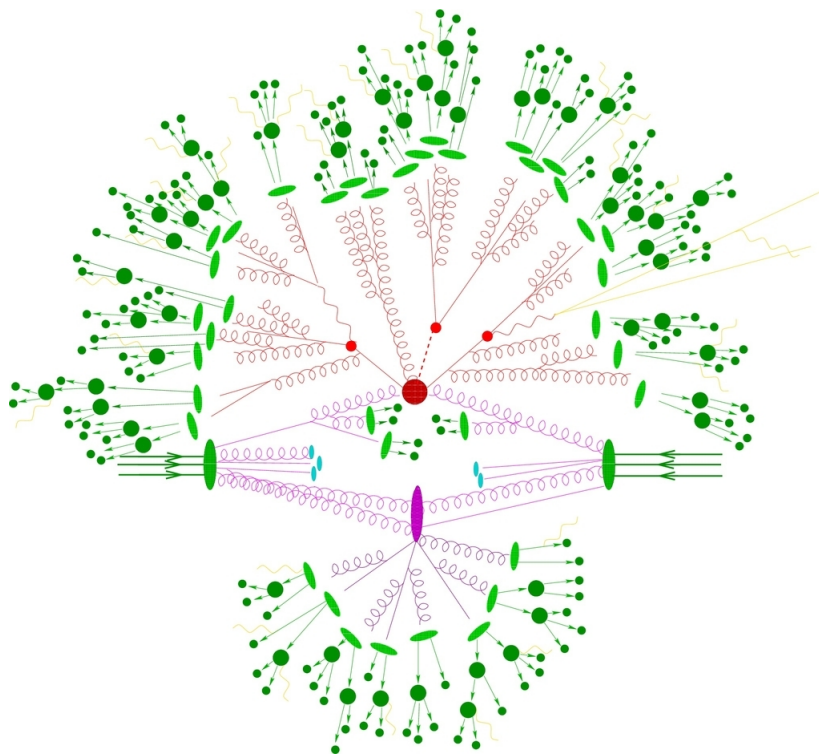
In the case of hadron colliders such as the LHC, the initial states to be described in the cross section are bound states, such as protons, of more fundamental particles; this complicates the computation of cross sections. However for the case of the high-energy collisions that are of interest here, hadronic bound states can be interpreted as distributions of free particles, each with a fraction of the total hadronic momenta. Such distributions can be computed from experimental results and are, rather tautologically, known as parton distribution functions. The use of PDFs in Monte Carlo's is represented in the figure by blue partons emanating from the incoming hadrons (large green blobs in the figure). The computation of the hadronic cross section proceeds by employing the cross sections of the constituent particles convolved with their respective distribution functions, this is naturally expressed as

$$\sigma_{\text{Hadronic}} = \sum_{a,b} \int_0^1 d\eta_1 \int_0^1 d\eta_2 f_a^{H1}(\eta_1) f_b^{H2}(\eta_2) \hat{\sigma}_{ab \rightarrow X}(\eta_1 P_1, \eta_2 P_2)$$

where  $f_a^{Hi}(\eta_i)$  represent the PDFs and  $\eta_i$  is the partonic fractions. The task of a Monte Carlo is not yet complete however, as the final states measured by colliders provide a picture that is more complicated than can adequately be computed from the 'free unbound' cross sections so far described. There are two observations that are worth considering from such events; in the first instance such events have large multiplicities of particles, so much so that it is not feasible to calculate the precise matrix element, and additionally that these particles are often bound hadronic states. Such events are described in the Monte Carlo by utilizing the simple cross section set up to describe a hard process, essentially one which involves significant momentum transfers, represented in the figure by the intersection of partonic lines in a large red dot. The partons involved in this process are then subject to a parton shower.

A parton shower simply evolves such a parton from the hard process to a lower energy scale at which it is observed; as this evolution occurs the parton successively branches into multiple partons and as such is similar to the the emission of x-rays by high energy electrons as they decelerate. Diagrammatically this can be seen from the successive branching of parton lines moving away outward from the hard process. In using this technique the high multiplicity of final state events is described. The problem of hadronisation of final state particles is the least well described aspect of the collider event, and entirely relies on phenomenological models fitted from data. In a Monte Carlo these models would kick in below a certain hadronisation scale, below which the parton shower would cease and partons would transform into hadrons based on the parameters in the hadronisation model. This stage can again be seen diagrammatically through the transformation, at the edges of the figure, of partonic lines into various green 'blobs' which represent the hadrons.

Hadronic collisions can also contain an additional component that is the result of the secondary interactions of the hadrons, in addition to the hard process. This is known as the underlying event of the interaction, and cannot be modelled directly from basic theory. As a result, similarly to hadronisation, this is modelled with various phenomenologically inspired models which must be fitted to data. The underlying event is diagrammatically represented in the figure, by the purple 'blob' and resulting purple partonic lines.



Diagrammatic representation of collider process as modelled in a monte carlo event generator ([www.sherpa-mc.de](http://www.sherpa-mc.de)). The stages of monte carlo modelling can be seen in this diagram; the large red centre represents the hard process, which then decays and showers into multiple partons, finally these hadronise in the 'green' stage

Part one of this thesis will then be concerned with the calculation of next to leading order corrections in QCD. Such calculations are principally motivated by the reduction of errors associated with perturbative scale choices, such as the factorization and renormalisation scales which result from performing such calculations. A drawback for such corrections is the often time consuming nature of such calculations. The automatic calculation of such corrections is therefore well motivated; in this vein general algorithms for the calculation of the real component of NLO corrections, such as the subtraction mechanism of Frixione, Kunszt and Signer, are of interest. Additionally, while such mechanisms undoubtedly improve the efficiency of such calculations, the phase space integration of corrections calculated from such mechanisms can be computationally costly in particular for higher multiplicity processes. This is to some extent unavoidable however, given that there is not a prescribed method for such calculations. Knowledge of the relative efficiency of various NLO calculational schemes can be of use in minimising this cost.

In this context this thesis will provide an overview of perturbative QCD, and will emphasise material relevant to the discussion of next to leading order corrections and Monte Carlo event generators. It will then provide a detailed overview of next to leading order calculations, including the motivation of such calculations, and describe how the real part of such calculations can be calculated using subtraction schemes. A detailed explanation of the subtraction mechanism of Frixione Kunszt and Signer is then undertaken, as a prelude to the description, in the following chapter, of the implementation of this method into the AMEGIC++ matrix element generator for NLO calculations of generic processes. Tests of this implementation are presented, including consistency under various parameter variations as well as comparisons with calculations based on different mechanisms. Finally this implementation is used to compare the relative efficiency of the FKS subtraction scheme with the method of Catani and Seymour for a number of processes. The relative efficiency of the FKS method is found to be larger in cases of larger partonic multiplicity.

Part two of this thesis will consider the applications of photon-photon induced

processes to observables at the LHC. The motivation for such considerations is the need for increasing accuracy on observables at the LHC, which is necessary to set increasingly stringent bounds on new physics beyond the Standard Model. On this basis it is not unreasonable that high level accuracy is an important for a number of processes; it is argued that examples of such processes include the high mass Drell Yan tail and the leptonic decay channels of  $W$  pair production. The calculation of photon-photon induced processes, which are formally part of the next to next to leading order electro-weak correction (the full electro-weak corrections are not considered), is undertaken based on the observation that a more modern set of PDFs which correct for QED effects has recently become available, namely the NNPDF2.3QED set allowing a comparison to be made with the standard MRST2004QED set.

These QED corrected PDFs calculate the photonic component to parton distribution functions allowing photon-photon induced processes to be calculated in the same fashion as partonic ones. Additionally the production of particles associated with strong electromagnetic fields of the colliding protons, which can be modelled by the equivalent photon approximation (EPA) or Weizsaecker Williams method, is considered. It is clear that this component, which is often overlooked, provides a contribution to photon-photon induced processes. The work considering such processes in this thesis is thus summarized; the background simulation set up in SHERPA for the photon-photon induced processes, based on both the QED PDFs and the EPA contributions is described in addition to the partonic baselines. The use of this set up for the case of Drell-Yan and  $W$  pair production is presented. For both processes the simulation set up is directly compared to ATLAS and CMS data, with details of analysis cuts provided. The contribution of the photon channels is then discussed.

# Part I

## NLO Calculations in SHERPA

# Introduction to Part I

The calculation of fixed order cross sections in perturbative QCD is central to efforts to model collider events, particularly in the context of Monte Carlo Event generators such as SHERPA. Improvements to these calculations, in terms of accuracy and reduction of errors, is therefore of primary importance for increasing the predictive power of collider models. Next to leading order corrections provide such an improvement, compared with leading order cross sections; in the first instance they provide a formally higher perturbative accuracy to the cross section, this improvement in perturbative accuracy also has the effect of a reduction in certain errors associated with scales.

Formally speaking the use of fixed order calculations introduces a dependence upon artificial scales, and as such the higher the perturbative order of the calculation the lower such a dependence is. The usual drawback of calculating such corrections is that they are often time consuming to perform and include singularities, which while cancel, can often make such computations difficult to perform, especially when using numerical methods. As such general algorithms for the calculation of the real component of the NLO correction, such as the subtraction mechanism of Frixione, Kunszt and Signer are of interest. In addition the existence of general algorithms allows the possibility of tools to calculate such corrections automatically. However, while the use of such algorithms undoubtedly improves efficiency for NLO calculations, they also include components that can become computationally expensive to calculate. While this is to some extent unavoidable, given that there is not a prescribed method for such calculations; knowledge of the relative efficiency of various NLO calculational schemes can be of use in minimising this cost.

The first part of this thesis is structured thus: An introduction is presented to perturbative QCD, in which the theoretical background relevant for NLO calculations is described and in addition includes discussions relevant to collider physics and Monte Carlos. A review of next to leading order calculations is then shown, where the primary motivations for such corrections are discussed in detail and calculation details of such corrections presented. The concept of a subtraction mechanism is discussed, which allows the numerical computation of the real part; the Catani-Seymour subtraction formalism is described as an example of such a computation. The subtraction scheme of Frixione, Kunszt and Signer is then reviewed in detail, with formulae necessary for computations presented.

A discussion is then presented detailing the implementation of the FKS subtraction mechanism in the AMEGIC++ matrix element generator, a component of SHERPA, allowing the automatic computation of the real component of the NLO correction to be made. The technical details necessary for this implementation, such as kinematic mappings are explicitly shown. The implementation is then subjected to testing to determine its validity; including its performance under numerical cutoffs, its consistency with other calculational methods and its variation under internal parameters. The FKS implementation is used in conjunction with an implementation of the Catani-Seymour formalism, also in AMEGIC++, to investigate the relative efficiency of both methods for conducting NLO calculations. As such results are presented for both methods concerning the computational speed of the subtracted real component of the calculations, which, time-wise can often be the bottleneck for NLO calculations. This is conducted for the processes  $e^+e^- \rightarrow jj$ ,  $e^+e^- \rightarrow jjj$ ,  $e^+e^- \rightarrow jjjj$  and  $jj \rightarrow e^+e^-$ , for both methods. Both are varied over a large range of internal parameters which can affect the result. The results are then discussed, with reference to process dependent factors. Finally the findings of this work are summarised and relevant conclusions drawn.

# Chapter 1

## The Foundations of QCD

Quantum Chromodynamics, the theory of strong interactions, is the foundation of most of the material presented in this work. It is the main theoretical backdrop to any attempts to describe the physics of high energy hadronic colliders, especially in the LHC era. There is a vast literature associated with the theory, most of which is beyond the bounds of this work.

### 1.1 QCD as a Gauge Theory

At its foundations, QCD is a non-Abelian quantum field theory, defined in the first instance by its classical Lagrangian density [7]

$$\mathcal{L}_{\text{Classical}} = -\frac{1}{4}F^{\mu\nu, a}F_{\mu\nu}^a + \sum_{\text{flavours}} \bar{q}_i^f (i\not{D} - m_f)_{ij} q_j^f \quad (1.1)$$

where the index  $f$  denotes the flavours of quark, with  $m_f$  denoting their masses (for most purposes in this work  $m_f$  can be safely set to zero).

The fields  $\{q_i\}$ , which describe the quarks are represented by spinors, a spin  $\frac{1}{2}$  representation of the Lorentz group and can be shown to have mass-dimensionality of  $[q_i] = \frac{3}{2}$  [8]; these are by construction anti-commuting objects which ensure that quarks are fermionic. The indices,  $i$  on the quark fields, indicate the colour states of the quarks; as these fields lie in the fundamental (or conjugate fundamental for  $\{\bar{q}_i\}$ )

representation of the SU(3) colour group, they can take the values  $i \in \{r, g, b\}$ . The fields  $\{\mathcal{A}_\mu^a\}$  lie in the vector representation of the Lorentz group, and are thus spin 1 vector bosons or gauge bosons and can be shown to have mass-dimensionality of  $[\mathcal{A}_\mu^a] = 1$ ; in QCD these are known as gluons. The gluonic fields also have a colour index,  $a$ , which can take the values  $a = \{0, \dots, 8\}$ , these fields thus lie in the adjoint representation of the SU(3) colour group. The field strength tensor and the covariant derivative given in the Lagrangian are defined in terms of these fields as follows:

$$F_{\mu\nu}^a = \partial_\mu \mathcal{A}_\nu^a - \partial_\nu \mathcal{A}_\mu^a - g_s f^{abc} \mathcal{A}_\mu^b \mathcal{A}_\nu^c \quad (1.2)$$

$$\not{D}_{ij} = \delta_{ij} \gamma^\mu \partial_\mu - i g_s \gamma^\mu \mathcal{A}_\mu^a t_{ij}^a \quad (1.3)$$

The factor  $\gamma^\mu$  represents the set of gamma matrices, which act on spinor indices; they are defined as obeying the Clifford algebra  $\{\gamma^\mu, \gamma^\nu\} = 2g^{\mu\nu}$ . The factor  $g_s$  given in these expressions is the coupling constant of QCD, and will play a larger role later; the terms  $t^a$  represent the generators of SU(3) in its fundamental representation, and  $f^{abc}$  are the structure constants of SU(3), defined from the commutation relations of these generators

$$[t^a, t^b] = i f^{abc} t^c \quad (1.4)$$

The Lagrangian is defined to be invariant under a local gauge transformation of the colour group SU(3). Under a local gauge transformation, the quark and gluon fields are defined to transform as

$$q_i(x) \rightarrow U_{ij}(x) q_j(x) \quad (1.5)$$

$$\bar{q}_i(x) \rightarrow \bar{q}_j(x) U_{ji}^{-1}(x) \quad (1.6)$$

$$t^a \mathcal{A}_\mu^a(x) \rightarrow U(x) t^a \mathcal{A}_\mu^a(x) U(x)^{-1} + \frac{i}{g_s} (\partial U(x)) U^{-1}(x) \quad (1.7)$$

where  $U(x) = e^{i\lambda^a(x)t^a}$ . These definitions then lead to the following gauge transformations for  $D_\mu$  and  $F_{\mu\nu}^a$

$$D_\mu q_i \rightarrow U_{ij}(x) D_\mu q_j \quad (1.8)$$

$$t^a F_{\mu\nu}^a \rightarrow U(x) t^a F_{\mu\nu}^a U^{-1}(x) \quad (1.9)$$

From the definitions given in 1.5 to 1.9 it is then clear that the Lagrangian is invariant under the local SU(3) gauge transformations.

The notion of gauge invariance is sufficient to define the classical Lagrangian of QCD, however for a correct quantisation of this theory the gauge freedom must be constrained.

This is exemplified by attempts to define a propagator for the gluon field, in the gauge invariant theory. The propagator, which can be calculated as the Green's function of the classical equation of motion for the 'free' gluonic field (ie without any interaction terms with quarks), is defined as the vacuum expectation value of a pair of fields; the gluonic propagator is therefore defined by

$$\Delta_{\mu\nu}(x-y) = \delta_{ab} \langle 0 | [\mathcal{A}_\mu^a(x) \mathcal{A}_\nu^b(y)] | 0 \rangle \quad (1.10)$$

where  $\Delta_{\mu\nu}(x-y)$  is the propagator. The ('free') gluonic field, in the gauge invariant theory, obeys the equation of motion

$$(g^{\mu\nu} \partial^2 - \partial^\mu \partial^\nu) \mathcal{A}_\nu^a(x) = 0 \quad (1.11)$$

Hence the gluonic propagator defined in the gauge invariant theory would then have to obey

$$(g^{\mu\nu} \partial^2 - \partial^\mu \partial^\nu) \Delta_{\nu\rho}(x, y) = i \delta_{\mu\rho} \delta(x-y) \quad (1.12)$$

Given that the operators present in 1.12 are not invertible, computing the Greens function is not possible; hence the propagator cannot be computed in the gauge invariant theory. The quantisation procedure is therefore carried out after constraining the gauge freedom of the gluon field.

Generally this gauge fixing can take the form of some constraint on the gauge boson fields, this constraint can be expressed in terms of a Lagrange multiplier added to the classical Lagrangian, and is generally referred to as a gauge fixing term  $\mathcal{L}_{\text{gauge fixing}} = [G(\mathcal{A}_\mu^a)]^2$ . The standard choice for gauge fixing gives the contribution

$$\mathcal{L}_{\text{gauge fixing}} = -\frac{1}{2\xi} (\partial^\mu \mathcal{A}_\mu^a)^2 \quad (1.13)$$

which corresponds to the constraint  $\partial^\mu \mathcal{A}_\mu^a = 0$  (Lorentz gauge) and where the parameter  $\xi$  sets a choice of gauge, common choices are  $\xi = 1$  (Feynman gauge) or  $\xi = 0$

(Landau gauge).

The addition of this gauge fixing term to the Lagrangian of a non-Abelian gauge theory entails the introduction of the Faddeev-Popov, or ghost, terms to the Lagrangian. This constraint, when applied to the functional integral of the quantum field theory gives rise to additional contributions to the Lagrangian. Following the method of Faddeev and Popov, these contributions can be written in terms of additional fields, known as ghost fields and give the following addition to the Lagrangian [7].

$$\mathcal{L}_{\text{ghost}} = \partial_\mu \bar{\eta}^a \partial^\mu \eta^a - g_s f^{abc} \partial_\mu \bar{\eta}^a \eta^b \mathcal{A}^{\mu c} \quad (1.14)$$

The fields  $\eta$ , which are anti-commuting scalars, are not interpreted as representing physical particles; however in perturbative calculations they do give rise to contributions via internal lines as virtual particles. The addition of these terms in perturbative calculations cancels unphysical polarisations of gauge bosons, which otherwise appear and act to ensure the unitarity of the theory. The full Lagrangian for QCD, a combination of the classical part and additional terms due to the gauge fixing, can now be used to derive the Feynman rules for QCD [9].

## 1.2 Renormalisation of QCD

Renormalisation is a concept central to modern understanding of Quantum Field Theory and is a much richer subject than will be presented in this briefest of overviews, more thorough reviews can be found in [7] and [8]. Renormalisation has two principle consequences that are relevant for these purposes; the first is that it enables divergences in the virtual corrections associated with arbitrarily high momentum scales to be absorbed, meaning that perturbation theory remains a valid tool. Secondly it has the consequence of causing parameters in the theory to gain a scale dependence. The technicalities will not be discussed in detail, nor will subjects such as what constitutes a renormalisable QFT; it is sufficient for the purposes of this work to state the QCD is a renormalisable theory and to briefly discuss the procedure for QCD and its consequences.

The motivating factor for renormalisation is, as has been alluded to, the appearance

of apparent singularities in quantum corrections of perturbation theory, which involve integrals over unconstrained momenta known as loop contributions; clearly this is a significant problem for the use of perturbation theory in QCD (and other QFTs). These contributions are represented in terms of Feynman diagrams that contain com-

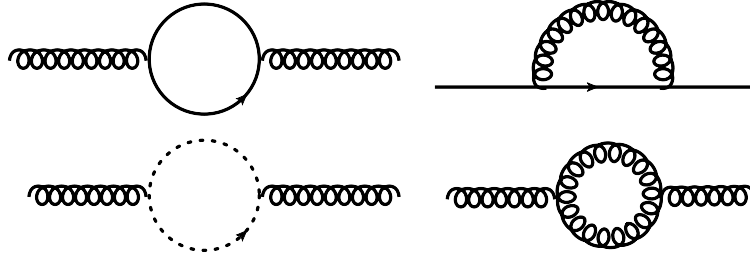


Figure 1.1: The one loop Feynman diagrams contributing to the self energy of quarks and gluons. From top right: the fermion loop contribution to gluon self energy, the gluon loop contribution to quark self energy, the ghost loop contribution to the gluon self energy and the gluon loop contribution to the gluon self energy.

plete loops of particles, typical one-loop Feynman diagrams are given in figure 1.1. In a renormalised theory bare parameters and fields present in the Lagrangian in 1.1, do not, in higher order perturbation theory, correspond to the physically measurable or renormalised quantities; perturbative calculations should then be performed with the renormalised, not bare quantities [7]. The reparamaterization of the theory in terms of renormalised quantities is mathematically carried out by a simple rescaling. For the parameters that are of interest, the quark and gluon fields and the strong coupling, this rescaling is given by:

$$q_0 = Z_q^{1/2} q_r \quad (1.15)$$

$$A_0^{\mu a} = Z_G^{1/2} A_r^{\mu a} \quad (1.16)$$

$$g_{s r}^2 = Z_{g_s} g_s^2 \quad (1.17)$$

if the rescaling parameters,  $Z_i$  are rewritten in the form  $Z_i = 1 + \delta_i$ , the bare Lagrangian can be split up in terms of a renormalised Lagrangian (the same as the bare  $\mathcal{L}$  but in terms of the renormalised quantities) and Lagrangian of counter terms:

$$\mathcal{L}_{0,\text{QCD}} = \mathcal{L}_{r,\text{QCD}} + \mathcal{L}_{\text{cnt},\text{QCD}} \quad (1.18)$$

The motivation for this re-writing is simply that the perturbative series in terms of the renormalised quantities, which will be of the same form as for the bare ones, now has counter terms which will be used to deal with singularities. This counter term Lagrangian can easily be obtained from performing the rescalings on parameters in 1.1, for example the quark gluon coupling term in  $\mathcal{L}_{\text{cnt,QCD}}$  is given by

$$\mathcal{L}_{\text{cnt,QCD}} = \left( \delta_q + \frac{1}{2}\delta_G + \delta_{g_s} \right) g_{s,r} \bar{q} \gamma^\mu \mathcal{A}_\mu^a t^a q \quad (1.19)$$

where contributions of the order  $\mathcal{O}(\delta_i \delta_j)$  have been ignored (the justification is that they contribute only at NNLO for the renormalisation of the strong coupling, which is not relevant for discussion of order NLO). The counter term Lagrangian now yields contributions to the perturbative calculations and, as has been stated, the idea is to use the counter terms to remove singularities from loop integrals.

To parametrise the singularities present, some form of regularisation is necessary for their representation; the conventional way to represent singularities in higher order QCD calculations is dimensional regularisation. In dimensional regularisation momentum integrals which would give divergent contributions are computed in  $4 - 2\epsilon$  dimensions, as opposed to four. The term  $\epsilon$ , is then taken to tend to zero, singularities are then expressed as poles in  $\epsilon$ . The momentum integrals are then re-written

$$d^4 k \rightarrow \mu^{2\epsilon} d^{4-2\epsilon} k \quad (1.20)$$

where the scale  $\mu$  is introduced to maintain the dimensionality of the couplings and fields; without this scale, couplings such as  $g_s$  become dimensionful to the  $\mathcal{O}(\epsilon)$ . The cancellation of singularities may also include the cancellation of finite pieces in addition to the poles in  $\epsilon$ ; a consistent choice of these finite terms is known as a renormalisation scheme. The simplest example of a renormalisation scheme is minimal subtraction, usually written as MS, which as its name suggests has no finite contributions, the cancellation of singularities then simply amounts to the cancellation of poles in  $\epsilon$ . To finite order in perturbation theory there exists a scheme dependence on results. The scheme used in this thesis is that of modified minimal subtraction  $\overline{\text{MS}}$ , in this scheme poles are represented as

$$\frac{1}{\bar{\epsilon}} = \frac{1}{\epsilon} + \log 4\pi - \gamma_E \quad (1.21)$$

where  $\gamma_E$  is the Euler gamma constant. The  $\overline{\text{MS}}$  pole can also be written in the form

$$\frac{1}{\bar{\epsilon}} = \frac{(4\pi)^\epsilon}{\Gamma(1-\epsilon)} \frac{1}{\epsilon} \quad (1.22)$$

which is often a convenient factor to subtract. It should be noted that dimensional regularisation also parametrises infra-red singularities, which will be the subject of much of this thesis.

The use of renormalisation conditions, which fix the renormalised parameters in the theory at a certain energy scale  $\mu_R$  (the renormalisation scale), then enables the counter terms to be set such that the cancellation of UV divergences takes place. The consequence of this is the introduction into the theory of scale dependence of parameters. This dependence upon scale is expressed in the form of renormalisation group equations which describe the running of parameters in the theory with scale; for the strong coupling this is described by

$$\mu_R \frac{\partial \alpha_s}{\partial \mu_R} = \beta(\alpha_s(\mu_R)) \quad (1.23)$$

where the strong coupling is written in terms of  $\alpha_s = \frac{g_s^2}{4\pi}$ , and the beta function is expressed as:

$$\beta(\alpha_s) = -\frac{\alpha_s^2}{2\pi} \beta_0 + \mathcal{O}(\alpha_s^3) \quad \beta_0 = \frac{11N_c - 2N_f}{6} \quad (1.24)$$

where for QCD  $N_c = 3$ . To  $\mathcal{O}(\alpha_s)$ , which is of interest as the main focus of this work are tools for NLO QCD, this yields the running of  $\alpha_s$ , from [9] to be

$$\alpha_s(\mu_R) = \frac{\alpha_s(\mu)}{1 + \beta_0 \frac{\alpha_s(\mu)}{2\pi} \log \frac{\mu_R}{\mu}} \quad (1.25)$$

The results of this running on  $\alpha_s$  have two clear, but profound, consequences; at high scales it can be seen that  $\alpha_s$  becomes small, a phenomena known as asymptotic freedom. It is assumed throughout this work that it is appropriate to treat QCD in perturbation theory, and it is clear that at sufficiently high scales this is an appropriate assumption. Conversely however at lower energy scales it is seen that  $\alpha_s$  becomes

larger, lower than around 500 MeV perturbation theory for  $\alpha_s$  is no longer appropriate as higher order terms become too large to ignore [9]. This low energy growth of  $\alpha_s$  is consistent with the phenomena of colour confinement, whereby coloured objects such as quarks are only found in bound colourless objects such as hadrons.

Renormalisation has the consequence of the introduction into the theory of a scale  $\mu_R$ ; the scale at which  $\alpha_s$  is fixed. The use of such a scale is to some extent an artifact of the calculation, physical observables should not have a dependence on such a scale which is introduced by hand. Reassuringly an all orders calculation in perturbative QCD does indeed remove any dependence upon  $\mu_R$  [9]; however in practical calculations the perturbative series is almost always truncated. A truncated perturbative calculation does retain a residual dependence upon  $\mu_R$ , the reason for this can be motivated from the form of the beta function; the variation of  $\alpha_s(\mu)$  with the scale  $\mu$  is at least  $\mathcal{O}(\alpha_s^2)$ , hence any scale variation can only be removed by additional contributions at higher orders. This can be explicitly seen by considering the expansion of  $\alpha_s$  in terms of a new scale.

$$\alpha_s(\mu) = \alpha_s(\mu_R) + \frac{\alpha_s^2(\mu_R)}{2\pi} \beta_0 \log \frac{\mu^2}{\mu_R^2} + \mathcal{O}(\alpha_s^3(\mu_R)) \quad (1.26)$$

The expansion of  $\alpha_s$  demonstrates that the variation due to the scale is an order of  $\alpha_s^2$  and higher; hence the inclusion of terms of at least  $\mathcal{O}(\alpha_s^{n+1})$  are required to remove the scale variation of terms of  $\mathcal{O}(\alpha_s^n)$ . The truncation of the series thus causes a residual dependence on the value of  $\mu_R$ , this dependence is notably reduced the higher the fixed order of the calculation, which provides additional motivation for performing higher order corrections.

The truncation of the perturbative series also leads to a dependence upon the renormalisation scheme of the calculation, and usually appears in the context of renormalised parameters such as  $\alpha_s$  in a similar fashion to the scale dependence. Again this is simply the result of the truncation of the perturbative series, any all orders calculation is free of such a dependence. As with scale dependence this can be

reduced with the inclusion of higher orders, although generally it is not as significant a source of error as the scale dependence.

## 1.3 Unresolved Limits of QCD Matrix Elements

Before proceeding with further discussion, it will prove useful to describe some useful results associated with QCD matrix elements (specifically leading order matrix elements) in the limit that one of the legs/particles somehow becomes kinematically unresolved from the other legs/particles in the process. The kinematics allow for this to occur in two distinct ways; the limit when a particle tends to zero energy and a limit where the angle separating two particles momenta tends to zero. The note that will be made here is that, for the discussion in this thesis, only one particle unresolved limits will prove useful; and the discussion in this section is strictly limited to such cases.

### 1.3.1 Notation

Before giving explicit expressions, it will prove useful to define some convenient notation, which takes inspiration from the conventions of [10]. First of all it is useful to define the shorthand  $r_n = a_1, \dots, a_n, k_1, \dots, k_n$ , where  $a_i$  is the flavour, and  $k_i$  momenta of particle  $i$ , for expressions where the particle and flavour content of matrix elements will change. Some constants from colour algebra are then expressed as

$$C(q) = C_F = \frac{N_c^2 - 1}{2N_c} \quad \gamma(q) = \frac{3}{2}C_F \quad (1.27)$$

$$C(g) = C_A = N_c \quad \gamma(g) = \frac{N_c^2 - 1}{2N_c} \quad T_F = \frac{1}{2} \quad (1.28)$$

The following definitions are made.

$$\mathcal{M}^{(n,0)}(r_n) = \frac{1}{2s} \frac{1}{\omega(a_1)\omega(a_2)} \sum_{\text{Colour,spin}} |\mathcal{A}^{(n,0)}(r_n)|^2 \quad (1.29)$$

$$\mathcal{M}_{kl}^{(n)}(r_n) = \frac{1}{2s} \frac{\delta_{kl} - 2}{\omega(1)\omega(2)} \sum_{\text{Colour,spin}} \mathcal{A}^{(n,0)}(r_n) \vec{Q}(a_k) \cdot \vec{Q}(a_l) \mathcal{A}^{(n,0)}(r_n)^* \quad (1.30)$$

Where  $\{\vec{Q}\}$  gives a representation of the colour algebra,  $t_{ij}^a$  for quarks and  $T_{bc}^a$  for gluons, so it can be shown that  $\vec{Q}(a_k) \cdot \vec{Q}(a_l) = \vec{Q}(a_l) \cdot \vec{Q}(a_k)$  and  $\vec{Q}(a_k) \cdot \vec{Q}(a_k) = C(a_k)$ . The factors,  $\omega(a_1)$  and  $\omega(a_2)$ , ensure that the spin and colour of initial state particles in  $\mathcal{M}$  is averaged over; thus for quarks  $\omega(a_1) = 2N_C = 6$  and for gluons  $\omega(g) = 2(N_C^2 - 1) = 16$ .

### 1.3.2 Explicit Expressions

The first unresolved limit that will be considered is the soft limit; physically this amounts to the additionally radiated particle in real amplitude tending to low (or zero) energy. Taking the soft limit of the matrix element squared is a well known result, and in QCD is given to be

$$\lim_{k_i \rightarrow 0} \mathcal{M}^{n+1}(\{k\}_{n+1}) = \delta_{ga_i} 4\pi\alpha_s \sum_{k \neq l} \frac{\hat{k}_k \cdot \hat{k}_m}{\hat{k}_k \cdot k_i \hat{k}_l \cdot k_i} \mathcal{M}_{kl}^n(\{\hat{k}\}_n) \quad (1.31)$$

where it is noted that this limit applies only for gluons. The soft limit involves a sum over all the momentum of all (coloured) particles, with no dependence on the species (quark or gluon) of the particle. The soft limit for quarks, although kinematically possible for massless quarks (which unless otherwise stated they will be in this work) does not lead to a divergent contribution and is therefore not considered. The result is clearly divergent for  $k_i \rightarrow 0$ , a result that will become more relevant in the next chapter.

The single unresolved limits of QCD matrix elements squared also include the collinear limit of two partons. In this limit  $\mathcal{M}$  factorises, in a form not unfamiliar to the soft limit above. In its most general form the factorisation is described by

$$\lim_{k_i \parallel k_j} \mathcal{M}^{(n+1)}(\{k\}_{n+1}) = \frac{4\pi\alpha_s}{k_i \cdot k_j} P_{a_j a_{ij}}^{\mu\nu}(z) \mathcal{M}_{\mu\nu}^{(n)}(r_{[i,j]}^{a_{ij}}, \{\hat{k}\}_n) \quad (1.32)$$

where collinear limits of this kind are dealt with in detail in [11], and  $r_{[i,j]}^{a_{ij}}$ , using the notation of the previous section, defines the set of  $n$  particles and momenta; where particles  $i$  and  $j$  are excluded and replaced by a combined parton  $a_{ij}$ . This combined particle has its flavour defined by a combination of the flavours of particles  $i$  and

$j$ . This limit, unlike the soft limit contains a spin dependence, symbolised by the tensorial notation of both terms, in addition to a splitting function dependence on the flavours of partons  $i$  and  $j$ . The splitting functions are universal for all processes, and are given as a function of  $z$ , which describes the fractional energy of one of the collinear partons, which in this case is labelled  $j$ . The splitting functions are labelled in terms of the flavours of one of the collinear partons and the combined parton, which completely describes the splitting process. The spin indices in the factorisation formula above are dependent upon the flavour of the combined parton which arises from the collinear limit; if this is a quark they take the form of spinor indices and for gluons they are Lorentz indices. For quark splittings the factorisation is spin independent and the splitting functions can therefore be written in the form

$$P_{aiq}^{ss'} = \delta_{ss'} P_{aiq}(z) \quad (1.33)$$

where  $P_{a_i a_j}(z)$  are the spin averaged, or Altarelli-Parisi splitting functions; for quark splittings they are given below.

$$P_{gq}(z) = C_F \left( \frac{1+z^2}{1-z^2} \right) \quad (1.34)$$

$$P_{qq}(z) = C_F \left( \frac{1+(1-z)^2}{z} \right) \quad (1.35)$$

The gluonic splitting functions retain a spin dependence, and are given by

$$P_{qg}^{\mu\nu}(z) = T_F \left[ -g^{\mu\nu} + 4z(1-z) \frac{k_{\perp}^{\mu} k_{\perp}^{\nu}}{k_{\perp}^2} \right] \quad (1.36)$$

$$P_{gg}^{\mu\nu}(z) = 2C_A \left[ -g^{\mu\nu} \left( \frac{z}{1-z} + \frac{1-z}{z} \right) - 2(1-\epsilon)z(1-z) \frac{k_{\perp}^{\mu} k_{\perp}^{\nu}}{k_{\perp}^2} \right] \quad (1.37)$$

where  $k_{\perp}$  is the momentum transverse to the direction of the combined momentum  $p_{ij}$ . The momenta of the collinear partons can be written in terms of the combined momenta  $p_{ij}$ ,  $k_{\perp}$  and a light-like momentum  $n$ .

$$p_j = zp_{ij} + k_{\perp} + \xi_1 n \quad (1.38)$$

$$p_i = (1-z)p_{ij} - k_{\perp} + \xi_2 n \quad (1.39)$$

The definitions  $k_\perp \cdot p_{ij} = k_\perp \cdot n = 0$  are made; the light-like vector  $n$  must be included for  $p_i^2 = p_j^2 = 0$ , which also fixes the quantities  $\xi_1$  and  $\xi_2$ .

$$\xi_1 = -\frac{1}{z} \frac{k_\perp^2}{2p_{ij} \cdot n} \quad (1.40)$$

$$\xi_2 = -\frac{1}{1-z} \frac{k_\perp^2}{2p_{ij} \cdot n} \quad (1.41)$$

The factorised matrix elements squared can be re-written in terms of the spin averaged or Altarelli-Parisi splitting functions and terms that have the explicit angular dependence

$$\lim_{k_i || k_j} \mathcal{M}^{(n+1)}(\{k\}_{n+1}) = \frac{4\pi\alpha_s}{k_i \cdot k_j} P_{a_j a_{ij}}(z) \mathcal{M}^{(n)}(r_{[i]}^{a_{ij}}, \{\hat{k}\}_n) + \frac{4\pi\alpha_s}{k_i \cdot k_j} Q_{a_j a_{ij}}(z) \tilde{\mathcal{M}}^{(n)}(r_{[i]}^{a_{ij}}, \{\hat{k}\}_n) \quad (1.42)$$

where again  $P_{a_j a_{ij}}(z)$  are the Altarelli-Parisi splitting functions. The term  $Q_{a_j a_{ij}}(z) \tilde{\mathcal{M}}^{(n)}(r_{[i]}^{a_{ij}}, \{\hat{k}\}_n)$  is the explicit angular contribution, which can be obtained from the off-diagonal terms in the tensorial product in 1.32, and is defined in appendix B. The gluonic spin averaged splitting functions (for quarks they are given above) are

$$P_{gg}(z) = 2C_A \left( \frac{z}{1-z} + \frac{1-z}{z} + z(1-z) \right) \quad (1.43)$$

$$P_{qg}(z) = T_F (z^2 + (1-z)^2) \quad (1.44)$$

it is noted these can be obtained from spin averaging 1.36 and 1.37. Unsurprisingly the functions  $Q_{a_j a_{ij}}(z)$  can be read off to be

$$Q_{gg}(z) = -4C_A z(1-z) \quad (1.45)$$

$$Q_{qg}(z) = 4T_F z(1-z) \quad (1.46)$$

It is commonplace to neglect angular contributions to the collinear splitting, as in most cases after integrating over the phase space these terms disappear. However in subtraction terms, which will be detailed in the next section and are based on unresolved limits of matrix elements, will need to include angular contributions to avoid numerical instabilities when the phase space integral is taken.

The Altarelli-Parisi splitting functions, given above are sometimes written in a regularised form, the regularisation is often included due to singularities in the splitting functions when  $z$  tends to one or zero. The regularisation is accomplished by use of plus distributions; where a plus distribution of a function, with a singular term at zero would act as  $\int dx f(x)_+ = \int dx f(x) - f(0)$ . The regularised splitting functions are then expressed as:

$$\hat{P}_{qq}(z) = C_F \left( \frac{1+z^2}{1-z} \right)_+ \quad (1.47)$$

$$\hat{P}_{gq}(z) = C_F \frac{1+(1-z)^2}{z} \quad (1.48)$$

$$\hat{P}_{gg}(z) = 2C_A \left( \left( \frac{z}{1-z} \right)_+ + \frac{1-z}{z} + z(1-z) \right) \quad (1.49)$$

where the  $P_{qg}$  is unchanged as it is always finite.

## 1.4 Collider Physics and the QCD Parton Model

In the environment of a hadron collider it must be noted that the hadrons, typically protons or anti-protons used in the collider, are bound states of coloured objects. The need to accurately describe the physics of hadron colliders, such as the LHC, is one of the driving forces behind the research in perturbative QCD; however perturbative calculations of cross sections from quantum field theory do not seem well suited to processes with hadronic initial states.

However hadrons are bound states of coloured particles and so collisions between these objects must be related to the perturbative calculations of cross sections from quantum field theory, which are calculated for free particles. The description of such collisions in terms of partonic density functions (PDFs) and partonic cross sections of (free) partons, will be reviewed in this section.

### 1.4.1 Naïve Parton Model

The description of hadronic cross sections in terms of PDF's and partonic cross sections calculated from quantum field theory (usually QCD in the context of this work)

is best motivated from the naive parton model. In the framework of this model, some fairly basic assumptions are given which allow the naive calculation of hadronic cross sections. The fundamental assumptions of this model are that the hadrons, at the high energies typically found in colliders, can be simply modelled as a collection of unbound (i.e. free) partons, which each have a fraction,  $\eta$  of the hadronic energy. These partons are considered to be the fundamental objects found in the QFT, typically quarks and gluons (although non QCD objects such as photons also have non-negligible contributions). A key assumption of the model is that hadronic cross sections at these energy scales can then factorise into convolutions, over the fraction  $\eta$ , of partonic cross sections with a distribution function of the parton. These distribution functions are the partonic density functions (PDFs), and give the distribution of a given parton at a specified energy fraction. The factorisation of the hadronic cross section can now be written as

$$\sigma_{\text{Hadronic}} = \sum_{a,b} \int_0^1 d\eta_1 \int_0^1 d\eta_2 f_a^{H1}(\eta_1) f_b^{H2}(\eta_2) \hat{\sigma}_{ab \rightarrow X}(\eta_1 P_1, \eta_2 P_2) \quad (1.50)$$

(see [12]) where  $f_a^H(\eta)$  are the PDFs. The PDFs are essentially a set of empirically determined functions, that cannot be calculated perturbatively from first principles.

### 1.4.2 The Parton Model and QCD

The naïve parton model, described in the previous section, rested upon the assumption that partons in the hadron (at high energies) can be thought of as essentially free objects moving in the same direction as the hadron, each with a fraction,  $\eta$ , of the total hadronic momenta. These assumptions hold fairly well for tree level processes, however for higher order perturbative corrections in QCD, the model requires some modification. When considering higher  $\mathcal{O}(\alpha_s)$  perturbative corrections to the parton model it is clear that there is a contribution from the 'free' partons in the hadron radiating other partons. However this complicates the naive parton model; perturbative corrections now contain 'free' partons with non-zero transverse momentum from radiative corrections, clearly a departure from the naïve model in which partons have

no transverse momentum. To reconcile the PDF parton model with perturbation theory,  $\mu_F$ , the factorisation scale is introduced; partonic transverse momentum above the factorisation scale is said to contribute to the hard (i.e. partonic) process, and below this scale gives corrections to the PDF. Radiative contributions to PDFs require the reconsideration of the PDFs given in the naïve model; these are now regarded as bare distributions, analogous to bare couplings in renormalisation, the 'renormalised' distributions now with an explicit dependence on the factorisation scale contain these radiative corrections. These distributions can be written, like the renormalised couplings, in terms of the bare distributions plus higher order corrections, in this case radiative corrections; to  $\mathcal{O}(\alpha_s)$  this is given by [9]

$$f_{a_i}(\eta, \mu_F) = f_{a_i}(\eta) + \frac{\alpha_s}{2\pi} \sum_j \int_{\eta}^1 \frac{dy}{y} \hat{P}_{a_i a_j} \left( \frac{\eta}{y} \right) f_{a_j}(y) \log \left( \frac{\mu_F}{\kappa_{\text{cut}}} \right) + \mathcal{O}(\alpha_s^2) \quad (1.51)$$

where  $f_{a_i}(\eta)$  are the bare PDFs,  $\hat{P}_{a_i a_j}(z)$  are the (regularised) Altarelli-Parisi collinear splitting functions,  $y$  is the fractional partonic energy pre-splitting and the cutoff scale  $\kappa_{\text{cut}}$  given in the PDF radiative correction above, gives a crude regularisation. The partonic cross section will contain a similar term with a  $\log \mu_F^2$  dependence, obtained from counter terms which are discussed later in chapter two; these are added to partonic cross sections specifically to remove the low transverse momentum scale physics from the partonic process. From the form of 1.51, it is noted that the 'renormalised' distributions absorb the singularities associated with  $\kappa_{\text{cut}} \rightarrow 0$ , again in a similar fashion to renormalisation.

The scale dependence introduced in the PDFs from radiative corrections, now fixes PDFs to a factorisation scale. The evolution of PDFs with that scale can be computed, using the radiative corrections given above, yielding the expression [9]

$$\mu^2 \frac{\partial f_{a_i}(\eta, \mu^2)}{\partial \mu^2} = \frac{\alpha_s}{2\pi} \sum_j \int_{\eta}^1 \frac{dy}{y} \hat{P}_{a_i a_j} \left( \frac{\eta}{y} \right) f_{a_j}(y, \mu^2) + \mathcal{O}(\alpha_s^2) \quad (1.52)$$

which is the famous Dokshitzer-Gribov-Lipatov-Altarelli-Parisi (DGLAP) evolution equation [13] [14] [15]. The solutions of the DGLAP equation allow PDFs to be defined at one momentum to be determined at another, in analogy to beta functions

computed from renormalised quantum field theories. Splitting the physics of the process crudely into a soft component associated with the PDFs and the hard component associated with the partonic scattering cross section, yields a residual dependence of both of these quantities on the factorisation scale. These contributions will however cancel at all orders, meaning that the hadronic cross section is not dependent on this artificial scale  $\mu_F$ . However in practice hadronic cross sections are calculated to a finite order in perturbation theory and the truncation of the series causes a dependence on  $\mu_F$  to appear, analogous to the appearance of a renormalisation scale dependence for fixed order calculations. In practical calculations the factorisation scale is usually set equal to the renormalisation scale as this prevents corrections of the form  $\log \frac{\mu_f^2}{\mu_R^2}$  appearing, and generally both scales are chosen to be of the same order as the hard process. An estimate of the error associated with scale dependence can be obtained by varying the factorisation scale over a range of scales, in practical terms this may amount to a factor of two over the original scale choice. A judicious choice of factorisation (and renormalisation) scale can reduce the error associated with scale dependence on a fixed order calculation; several calculation methods, such as the Principle of Minimum Sensitivity (PMS) [16] [17], exist for this purpose (for most processes the choice of the hard scale is justified by these methods). However as this error is always at an  $\mathcal{O}(\alpha_s)$  greater than the order of the calculation, the scale dependence is reduced by including higher order corrections.

The introduction of the factorisation scale introduces some subtleties into partonic calculations; at higher orders contributions to the partonic cross section must not include radiative corrections below the factorisation scale and it must therefore be modified to meet this requirement. Discussion of PDFs and partonic cross sections at higher order is left to chapter two, after some of the machinery of such calculations has been described.

## 1.5 Jet Algorithms

The phenomena of colour confinement, where coloured objects such as quarks are only observed in bound colourless states such as hadrons, presents a problem when comparisons are made between experiment and theoretical predictions based on perturbative QCD. The treatment of this problem for initial states is described by PDFs and factorisation which are summarised in the previous section, however for final states this issue is dealt with by the introduction of jets. Jets can be simply described as a collection of hadrons in a detector, that are somehow assigned to one common bulk of hadronic matter. Sometimes what constitutes a jet can be fairly intuitive, for example two narrowly collimated bulges of hadronic matter in a detector can be clearly interpreted as a two jet event; however this is not always the case and precise definitions are necessary to enable valid comparisons between theory and experiment. For this reason jet algorithms are introduced, which, for a given input of protojets, hadronic clusters in experiments and partons in theory, return jets. The use of jet algorithms, first introduced in [18], is not unique and quite a number exist; for various applications the optimal choice of jet algorithms will be different.

Jet algorithms are usually formulated in terms of variables that are conveniently related under Lorentz boosts. The reference frame used for theoretical calculations (usually the partonic centre of mass frame) and the lab frame will, in general, be different; this motivates the use of variables in jet algorithms that have no or a simple frame dependence. In a collider, where the beam axis is said to lie in the  $z$  direction, it is clear that the lab and the centre of mass frames are simply related by boosts in the  $z$  direction; as a result the momentum of final state particles transverse to the beam axis,  $p_T$  will be invariant under these boosts, as will the azimuthal angle  $\phi$ . Both of these are variables often used in jet algorithms, in addition to the rapidity  $\eta$  which is defined to be

$$\eta = \frac{1}{2} \log \left( \frac{E + k_z}{E - k_z} \right) \quad (1.53)$$

Under a Lorentz boost in the  $z$  direction the variables  $E$  and  $k_z$  transform as  $E = \gamma(E + \beta k_z)$   $p_z = \gamma(\beta E + k_z)$ ; hence under a boost in  $z$

$$\eta' = \eta + \frac{1}{2} \log \frac{1 + \beta}{1 - \beta} \quad (1.54)$$

hence the difference in rapidity between any two particles is invariant under these boosts.

### 1.5.1 Infrared Safety

A key issue associated with jets is the ability to link theoretical calculations in perturbative QCD with the experimental situation of colour confinement and hadronic matter. The use of jet algorithms then allows a precise definition of jets that can be used for both theoretical and experimental purposes. The major part of this work is dedicated to providing tools for NLO QCD predictions; for NLO (and higher order) accuracy the definitions of jets must be constrained by the notion of infra-red (IR) safety. The constraint around IR safety is associated with the real emission component of a NLO cross section. The calculational details of NLO cross sections are left to later chapters, however the relevant point here is that in NLO calculations the tree level matrix element with an additional parton forms part of the  $\mathcal{O}(\alpha_s)$  correction, if a parton goes unresolved. These unresolved partons produce divergences in soft and collinear limits, which cancel IR divergences from loops; IR safety amounts to jet algorithms which are insensitive to the addition of partons with these limits. Essentially the condition of infrared jet safety is that the addition of soft or collinear partons to the final state does not alter the structure of the jets, and hence allows the cancellation described above to occur.

If the jet algorithms are sensitive to the addition of soft or collinear partons, the divergent structures in the real and loop contributions can be split into terms with different jet structures, meaning that a proper cancellation of singularities cannot take place - a result which is not consistent with perturbation theory [19].

### 1.5.2 Generalised $k_T$ Clustering Algorithms

A common set of jet algorithms which exhibit infra-red safety is the set of general  $k_T$  clustering algorithms; to provide an example of jet algorithms these algorithms are discussed in this section. This set of algorithms consists of three algorithms with a slight parameter difference, and are all by construction IR safe, they are: the  $k_T$  or Durham algorithm outlined in [20] and [21], the Cambridge-Aachen algorithm outlined in [22] and [23] and finally the anti- $k_T$  algorithm described in [24]. The generalised  $k_T$  algorithm is split into two steps; the first is a clustering procedure which decides whether a given set of protojets are merged into a jet and a merging procedure which defines the momentum of the jet in terms of the merged protojets momenta. The quantities used in the algorithms can now be defined as

$$d_i = k_{iT}^{2p} \quad (1.55)$$

$$R_{ij} = (\eta_i - \eta_j)^2 + (\phi_i - \phi_j)^2 \quad (1.56)$$

$$d_{ij} = \min(k_{iT}^{2p}, k_{jT}^{2p}) \frac{R_{ij}}{D^2} \quad (1.57)$$

where  $D$  is the jet resolution parameter, where the value is usually given in the range  $0.4 < D < 1.0$ ,  $\eta$  is the rapidity of the protojet and  $\phi$  the azimuthal angle. The value of the parameter discriminates the different algorithms.

$$p = -1 \quad \text{Anti-}K_T \quad (1.58)$$

$$p = 0 \quad \text{Cambridge - Aachen}$$

$$p = 1 \quad K_T \text{ Algorithm}$$

The clustering algorithm is defined by an iterative procedure; a list of protojets is input into the algorithm, the quantities  $d_i$  and  $d_{ij}$  are then calculated for all protojets. The minimum of  $d_i$  and all  $d_{ij}$ 's for each protojet is calculated; if the minimum is  $d_i$  then the protojet becomes a jet, if a  $d_{ij}$  is the minimum then protojets  $i$  and  $j$  are merged. The algorithm is carried out iteratively until there are simply jets in the process. The merging of momenta can then take the following form

$$E_{ij} = E_i + E_j \quad (1.59)$$

$$\vec{k}_{ij} = \vec{k}_i + \vec{k}_j \quad (1.60)$$

The result of the algorithm is simply a list of jets with well defined momenta.

The differences between the algorithms result from different analysis priorities, as jet definitions are arbitrary the user is free to use the most convenient definition for their purpose. The Cambridge-Aachen algorithm, which has no dependence the transverse momenta and is therefore clustered according to how collinear the particles are, is most favoured to measure the collinear splitting of partons, however it will clearly not cluster soft partons with a large angular separation. The  $k_T$  or Durham algorithm will cluster soft events well but has the disadvantage of producing jets which have complicated structure in the detector; for experimental purposes simple cone like structures are favoured. Anti- $k_T$  is often used because it produces these simple well defined cone like structures in experimental data, due to its inverse dependence upon  $k_T$ ; it does however have a downside similar to that of Cambridge-Aachen in that soft partons with large angles are often not clustered.

# Chapter 2

## Next-to Leading Order Calculations

The main purpose of this thesis is to describe and test tools developed for the calculation of cross sections in perturbative QCD at Next-to Leading Order (NLO). The computational details for the calculation of processes at NLO will be outlined in this chapter, and considered more thoroughly in chapter three for the method of FKS subtraction. This chapter will mostly be concerned with the appearance of infra-red divergences in NLO calculations, and will discuss how such divergences occur and how these cancel in the full calculation. Additionally, the computational difficulties associated with these calculations are discussed, particularly with numerical methods, and the concept of a subtraction scheme is introduced. Given that NLO calculations can be, if not technically difficult to perform, at least computationally expensive, the justification for performing such calculations is important and will also be reviewed. It is noted that, unless otherwise stated, the notation used in this section will be that described in section 1.3.1 of chapter one.

### 2.1 Motivation

The motivation for performing Next to Leading Order calculations for processes in QCD is fairly simple, to improve the accuracy of such calculations and obtain more

reliable error estimates. The inclusion of higher order terms in a perturbative calculation will by definition improve the accuracy of such calculations. However for QCD calculations in particular there is additional motivation for seeking higher order corrections, which has been touched upon in chapter one. This is of course the introduction of artificial scales into perturbative calculations, principally the renormalisation scale,  $\mu_R$  and (for hadronic processes) the factorisation scale. The dependence of fixed order calculations in perturbative QCD on these scales represents one of the principle sources of error in such calculations, which is significant as these scales are introduced for technical reasons and are not physical. An all orders calculation would of course remove this dependence; however, as was described in chapter one, for a truncated series the variation over such scales is at least an  $\mathcal{O}(\alpha_s)$  greater than the highest order term. This gives us two results, namely that no fixed order calculation can entirely be free of scale dependence, but also that such scale dependence reduces the higher the order of the calculation. Thus one of the principle sources of error can be reduced by performing higher order calculations. This is of course motivation for calculating QCD processes to the highest order technically possible. However higher order calculations, for reasons which will become apparent later in this chapter, are often technically difficult and computationally intensive to calculate - in many cases NLO is simply the best estimate that can currently be calculated. However NLO calculations are particularly well motivated from this argument as the biggest reduction in this scale dependence must come from going to NLO from LO, as the scale uncertainty is of  $\mathcal{O}(\alpha_s)$  larger the order of the calculation.

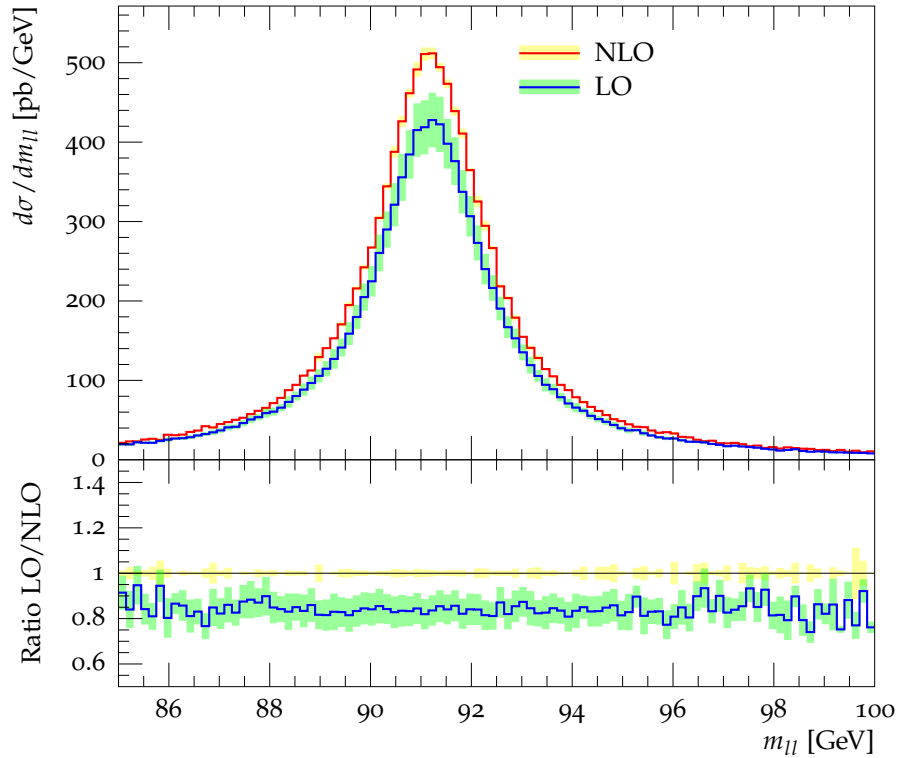


Figure 2.1: Lepton pair mass distribution of the Drell Yan Z mass peak, between  $85 < m_{ll} < 100$  GeV shown for LO and NLO. The error bands indicate the correlated variation of the factorisation and renormalisation scales between  $m_{ll}/2 < \mu < 2m_{ll}$

The reduction in such a scale dependence from LO to NLO is shown in figure 2.1 for the Drell Yan process, and as can be seen, this reduction is not insubstantial. Calculations that are only of leading order in a perturbative series are therefore particularly plagued by high uncertainties associated with scale variation. This is a particular problem for high multiplicity processes, for example if a leading order term is of order  $\mathcal{O}(\alpha_s^n)$  then a correction of the order  $n\alpha_s^{n+1} \log(\mu/\mu_R)$  is the leading contribution to the scale variation; if  $n$  is large then the scale variation can be of the order of the LO term. For such processes NLO calculations are then essential to obtain a reasonable estimate of the cross section.

## 2.2 Schematics of NLO calculations

Next to Leading Order (NLO) calculations in perturbative QCD are simply the  $\mathcal{O}(\alpha_s)$  corrections to the leading term in the perturbative series. The general composition of the NLO correction must therefore include all possible corrections to the process at  $\mathcal{O}(\alpha_s)$ . The components of an NLO calculation are given, schematically, in 2.1, and is composed of the leading order (Born) term,  $d\sigma^{(B)}$  and the  $\mathcal{O}(\alpha_s)$  corrections to this term. These contributions can be divided into two distinct parts; virtual corrections ( $d\sigma^{(V)}$ ) in the form of (one) loop Feynman diagrams and the real corrections ( $d\sigma^{(R)}$ ), which give contributions from an additional (unresolved) radiative emission. In addition to these terms, for hadronic initial states the partonic cross section must include counter terms ( $d\sigma^{(C)}$ ) originating from PDFs; the reason for these counter terms is discussed in chapter one. As can be seen from 2.1, the virtual and counter terms exist on the Born level phase space, whilst the real term must include the phase space of the extra emission.

$$\sigma_{\text{NLO}} = \int_m d\sigma^{(B)} + \int_m d\sigma^{(V)} + \int_m d\sigma^{(C)} + \int_{m+1} d\sigma^{(R)} \quad (2.1)$$

Both the real and the virtual terms of this NLO cross section contain divergent terms, both of which are associated with an unrestrained phase space integral; for the virtual term this is associated with loop integrals and for the real term this is associated with the unresolved partonic emission. The singularity structure of both the real and virtual corrections, which are explicitly given in later sections of this chapter, potentially poses a problem for perturbation theory. However perturbation theory is saved by the cancellation between the singularities present in both terms. The guarantee of this cancellation is the theorem of Kinoshita, [25] and Lee and Nauenberg, [26], which states that QCD is free of infra-red divergences, at all orders in perturbation theory, if all contributions at the relevant order are summed.

## 2.3 Virtual Contributions

The virtual corrections, of a process in perturbative QCD, are contributions in the perturbative series, which contain amplitudes with integral(s) over a virtual momenta. These amplitudes are represented, in Feynman diagrams, as containing a loop of particles, which gives the contribution of integral over unconstrained momenta which appears in propagators, a simple example is given in figure 2.2. It is from these loop integrals that the divergent terms in the virtual contribution arise. At NLO

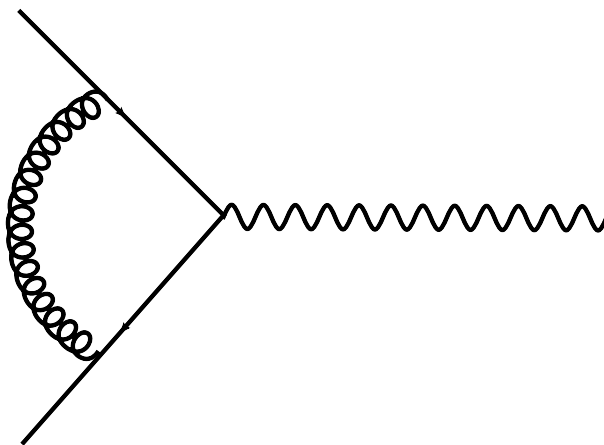


Figure 2.2: One loop diagram representing the virtual contribution at NLO of the process  $q\bar{q} \rightarrow \gamma^*$

the virtual contributions purely consist of amplitudes which contain only one loop term and a Born like final state, other terms are part of higher order corrections. The virtual terms can therefore be easily integrated over the same phase space as the Born term. Schematically the NLO virtual contribution can be written as

$$\mathcal{M}^{(n,1)}(r_n) = \frac{1}{2s} \frac{1}{\omega_1 \omega_2} \sum_{\text{Colour, spin}} \mathcal{A}^{(1\text{loop})}(r_n) \mathcal{A}^{(\text{tree})}(r_n)^* + \mathcal{A}^{(\text{tree})}(r_n) \mathcal{A}^{(1\text{loop})}(r_n)^* \quad (2.2)$$

The details associated with calculations of loop integrals will not be considered in this thesis, however the form of the resulting singularities is of interest. The divergent structure of loop terms has already been partially discussed in chapter one in the context of renormalisation; the loop integral over unconstrained momenta generally leads to two types of divergent structures, ultra-violet (UV) and infra-red

(IR), which are essentially divergences from arbitrarily high or low momenta and are associated with the upper and lower bounds of the loop integral. The appearance of these singularities becomes apparent when considering the form of these integrals; a generic loop diagram has the structure, from propagators of internal fields

$$\int d^4k \frac{k^{\mu_1} \dots k^{\mu_m}}{\prod_{i=1}^n (k_i - p_i)^2} \quad (2.3)$$

which for a crude discussion of singularities can be written as

$$\int d^4k \frac{k^{\mu_1} \dots k^{\mu_m}}{k^{2n}} \quad (2.4)$$

The integral, which runs over the entire phase space of the loop momenta, can become divergent either as the loop momentum becomes arbitrarily large (ultra violet) or when it tends to zero (infra-red); given the crude parametrisation of a loop integral above, it is clear that for  $m \geq n - 4$  a UV divergence will occur in 2.4 and that for  $n \geq m + 4$  an IR divergence will occur. The appearance of IR singularities in the virtual term is dealt with by their explicit cancellation with similar divergent structures in the real emission contributions - a cancellation which is guaranteed, order by order, in the KLN theorem. The IR divergent structure of the virtual term at NLO can be calculated generally and it is shown in [27] and [28] (the latter gives loop contributions for higher order terms as well) to be

$$\mathcal{M}^{(n,1)}(r_n) = \frac{\alpha_s}{2\pi} \frac{1}{\Gamma(1-\epsilon)} \left( \frac{4\pi\mu^2}{Q^2} \right)^\epsilon V(\epsilon) \quad (2.5)$$

where

$$V = - \left( \frac{1}{\epsilon^2} \sum_n C(a_n) + \frac{1}{\epsilon} \sum_n \gamma(a_n) \right) \mathcal{M}^{(n)}(r_n) + \frac{1}{2\epsilon} \sum_{nm} \log \frac{2k_k \cdot k_l}{Q^2} \mathcal{M}_{kl}^{(n)}(r_n) + \mathcal{M}_{\text{Finite}} \quad (2.6)$$

Where the  $\gamma$  constants are described by

$$\gamma(q) = \frac{3}{2}C_F \quad \gamma(g) = \frac{N_c^2 - 1}{2N_c} \quad (2.7)$$

for quarks and gluons respectively. This simply gives the infra-red pole structure of virtual terms at NLO, the finite contribution is left for actual calculation of loop

diagrams which will not be considered in this thesis. The scale  $Q^2$  is introduced, which is an arbitrary mass scale introduced by Ellis and Sexton to help the writing of the result - for convenience it is usually set to the Mandelstam variable  $s$ . The result above is calculated in conventional dimensional regularisation.

## 2.4 Real Emission Contributions

The contribution of radiative terms, to the NLO cross section, is generally known as the real emission term. In QCD, radiative corrections to the Born term of  $\mathcal{O}(\alpha_s)$  simply consist of Born like terms with one additional partonic leg; if the extra parton is unresolved such a term constitutes an NLO correction to the leading order term, and hence must be included in NLO calculation. Such terms can be computed, in QCD, with identical methods to that of the Born term, as they can simply be calculated from tree-level Feynman diagrams. The appearance of an unresolved parton in the real term poses the question as to the behaviour of QCD amplitudes in the unresolved limits. It will be seen that these limits, which amount to the unresolved particle becoming either soft, or collinear with another particle, are important for the singularity structure of the real term. It has already been demonstrated that infra-red divergences occur in the virtual terms, which are not absorbed by renormalisation, and it is the divergences from these unresolved limits that will cancel those from the loop terms. Schematically the form of the real emission term is given by

$$d\sigma^{(R)} = \mathcal{M}^{n+1}(r_{n+1}, \{k_{n+1}\}) J^{(n)} d\phi_{n+1} \quad (2.8)$$

Where  $\mathcal{M}^{n+1}$  is the  $n+1$  particle matrix element squared,  $d\phi_{n+1}$  represents the phase space integral and  $J^{(n)}$  the jet function. It is seen in this form that the jet function (sometimes described as the measurement function) describes a final state with  $n$  resolved jets, from a  $n+1$  parton final state. One of the partons is therefore somehow unresolved, there is therefore no restriction of its kinematics and it is free to take limits that make the matrix element singular. The previous chapter reviewed such unresolved amplitudes, and they will be considered here in the context of the real

emission term.

The unresolved limits of the limits of the matrix element squared, which are described in chapter one, are in the notation of this chapter given by:

$$\lim_{k_i \rightarrow 0} \mathcal{M}^{(n+1)}(\{k\}_{n+1}) = \delta_{ga_i} 4\pi\alpha_s \sum_{n \neq m} \frac{\hat{k}_n \cdot \hat{k}_m}{\hat{k}_n \cdot \hat{k}_i \hat{k}_m \cdot k_i} \mathcal{M}_{nm}^{(n)}(\{\hat{k}\}_n) \quad (2.9)$$

for the soft limit, and

$$\lim_{k_i \parallel k_j} \mathcal{M}^{(n+1)}(\{k\}_{n+1}) = \frac{4\pi\alpha_s}{k_i \cdot k_j} P_{a_j a_{ij}}(z) \mathcal{M}^{(n)}(r_{[i]}^{a_{ij}}, \{\hat{k}\}_n) + \frac{4\pi\alpha_s}{k_i \cdot k_j} Q_{a_j a_{ij}}(z) \tilde{\mathcal{M}}^{(n)}(r_{[i]}^{a_{ij}}, \{\hat{k}\}_n) \quad (2.10)$$

for the collinear limit, where the Altarelli-Parisi splitting functions are given in the previous chapter. It is commonplace to neglect angular contributions to the collinear splitting, as after integrating over phase space these terms disappear; however such terms must be included in subtraction terms (see next section), when using numerical methods, to ensure stability. Both of these expressions are clearly divergent in their respective unresolved limits; and it is noted that the form of these singularities is broadly the same (if factors from the phase space are included), and take the form of 2.11.

$$\lim_{x \rightarrow 0} \frac{1}{x} \quad (2.11)$$

To give a comparison with the virtual singularity structure, the phase space integral of the unresolved momenta, over such singular terms, can be calculated in dimensional regularisation to produce a crude pole structure. If this integral is performed on singularity structures of the form given in 2.11, the pole structure will be of the form of  $\frac{1}{\epsilon}$  (see [10]). Given that there is no kinematic reason to exclude it, the double limit of an unresolved parton, such that it becomes both soft and collinear with another parton, can exist. Naively this would give a divergent structure of the form  $\frac{1}{E_i(1-\cos\theta_{ij})}$  and a naive pole structure by previous arguments would be  $\frac{1}{\epsilon^2}$ . Continuing with this naive expression of singularities, the total singularity structure of an unresolved real matrix integrated over momenta of the unresolved parton would therefore be of the

form 2.12.

$$\left(\frac{A}{\epsilon^2} + \frac{B}{\epsilon} + C\right) \mathcal{M}^n(\{\hat{k}\}_n) \quad (2.12)$$

This singular structure, which as can be seen from equations 2.5 and 2.6, is of the same form identified as the singular structure of the virtual term. The argument given above is of a crude nature but does serve to illustrate that the form of the singularities in the real emission term does indeed match the form of singularities in the virtual term given in 2.5 and 2.6.

## 2.5 PDFs and Partonic Cross Sections at NLO

The discussion of PDFs, in section 1.3 of this thesis, describes the introduction of the factorisation scale into PDFs; this provides a distinction between low scale and high scale physics resulting from radiative corrections to the leading order partonic process. Such radiative corrections will occur in higher order corrections, and as such must be discussed here in the context of NLO calculations. As discussed in chapter one, radiative corrections which are below the factorisation scale give contributions to the PDFs and above to the partonic process. However, for the calculation of NLO cross sections, all radiative corrections are treated as part of the real correction. As result, for hadronic calculations, the use of PDFs requires corrections to prevent double counting of radiative contributions below the factorisation scale, which are implicitly included in PDFs. To prevent this double counting, of radiative corrections below the factorisation scale, the introduction of counter terms to the partonic cross section are necessary. When such corrections are included, the hadronic cross section will retain the form 2.13.

$$d\sigma_{\text{Hadronic}} = \sum_{a,b} \int_0^1 d\eta_1 \int_0^1 d\eta_2 f_a^{H1}(\eta_1, \mu_f^2) f_b^{H2}(\eta_2, \mu_f^2) d\hat{\sigma}_{ab \rightarrow X}(\eta_1 P_1, \eta_2 P_2) \quad (2.13)$$

However the partonic cross section is replaced by 2.14, [29] which is the partonic cross section supplemented with counter terms.

$$d\hat{\sigma}(k_1, k_2) = d\sigma(k_1, k_2) + d\sigma_1^{\text{cnt}}(k_1, k_2) + d\sigma_2^{\text{cnt}}(k_1, k_2) \quad (2.14)$$

These counter terms, which prevent the inclusion of the soft radiative contributions already present in the PDFs, are to NLO given by 2.15; where the terms  $K_{ad}(x)$  are factorisation scheme dependent functions, which in conventional dimensional regularisation are zero ( $K_{ad}(x) = 0$ ).

$$d\sigma_1^{\text{cnt}}(k_1, k_2) = \frac{\alpha_s}{2\pi} \frac{1}{\Gamma(1-\epsilon)} \left( \frac{4\pi\mu^2}{\mu_F^2} \right)^\epsilon \sum_d \int dx \left( P_{da}(x) \frac{1}{\epsilon} + K_{da}(x) \right) d\sigma_{db}^{(B)}(x_1 k_1, k_2) \quad (2.15)$$

Where the scale  $\mu$ , introduced in 2.15, is an arbitrary scale that allows the writing down of the result in dimensional regularisation; in most cases the choice  $\mu = \mu_F = \mu_R$ , the renormalisation scale, is made. The form of these counter terms can be obtained from considering the soft radiative contributions to the PDF given in equation 1.51, after a reparamaterization of integrals and the rewriting of the singularity in terms of dimensional regularisation these contributions can be written in the form of equation 2.15.

It is important to note that this contribution enables the cancellation, of initial state collinear singularities, from the real term; this does not occur with just the virtual piece (although all other singularities from the real term are indeed cancelled by the virtual contribution). The introduction of these counter terms into the partonic cross section, a result required by factorisation, is therefore very important for perturbative QCD. The singularities from these counter terms are required for the complete cancellation of singularities present in perturbative corrections beyond leading order.

## 2.6 Subtraction

Previous sections of this chapter has discussed the various components of NLO calculations, these are principally; the virtual terms, composed of quantum corrections, and the real terms, which are composed of radiative corrections. Both the real and virtual terms contain, as discussed in prior sections, singularities associated with infra-red limits, in either phase space or loop integrals. Such terms are guaranteed to cancel when the real and virtual terms are combined. However for practical calculations, this explicit cancellation can be problematic to achieve.

The singularity structure for virtual terms is usually computed by use of dimensional regularisation in loop calculations; thus the singular structure for the virtual term is commonly expressed in terms of poles. To enable an explicit cancellation of this pole structure by the real terms, it is necessary to use dimensional regularisation for the phase space integration of real terms. However, beyond simple low multiplicity processes, the use of numerical methods is required to perform the phase space integration of the calculation; as dimensional regularisation is an analytic method, it is not practical to compute real corrections in this fashion.

There clearly exists a practical problem for NLO calculations of non-trivial processes; an uncancelled explicit pole structure is combined with a divergent numerical integral, and although it is known the divergent structure does indeed cancel the pole structure, performing the calculation such that this cancellation is explicit requires some additional technicalities.

The method of choice to allow this explicit cancellation is subtraction; essentially this involves constructing a term on the real phase with an identical singular structure to the real term, this term is subtracted from the real term to cancel any singularities. To ensure the NLO calculation remains unchanged, the subtraction term is also added back to the calculation; however this subtraction term is usually integrated analytically (using dimensional regularisation) to explicitly cancel the pole structure of the virtual terms. There do exist other methods, notably phase space slicing [30] which essentially performs a kind of cutoff regularisation upon the real phase space integral and phase space sector decomposition [31], however neither will be discussed in this work in any depth as the focus will be on the use of subtraction.

The unresolved limits of the QCD matrix elements are described in the previous chapter, and it is clear from these results that the singular regions of the real term are the result of the two possible unresolved limits of the partons. These limits are explicitly the soft limits of any (gluonic) parton, and the collinear limit of any two (massless) partons; the subtraction term is required to have the same singularity structure, hence its behaviour in these kinematic limits must be the same as the real

term as shown in 2.16.

$$\lim_{k_i \rightarrow 0 \text{ or } k_i \parallel k_j} d\sigma^{(R)} = \lim_{k_i \rightarrow 0 \text{ or } k_i \parallel k_j} d\sigma^{(S)} \quad (2.16)$$

The subtraction terms are constructed such that, in addition to having the same singularity structure as the real term, they can simply be integrated over the momenta of the unresolved parton analytically. This allows this integral, over the unresolved partons phase space, to be performed in dimensional regularisation, yielding an explicit pole structure; the 'added back' subtraction term is written in this way. After performing this analytic integral, over the unresolved partonic phase, on the subtraction term, it becomes an object on the same Born level phase space as the virtual term. Additionally this integrated subtraction term contains an explicit pole structure, which is able to cancel the pole structure of the virtual term; this cancellation is guaranteed by the KLN theorem and the definition of the subtraction term. The integrated subtraction term and the virtual term can then be combined into one term with no pole structure, which is integrated over the same  $n$  particle phase space. The form of an NLO calculation using subtraction is given by 2.17, where  $d\sigma^{(S)}$  represents the subtraction term.

$$\sigma_{\text{NLO}} = \int_m d\sigma^{(B)} + \int_m \left[ d\sigma^{(V)} + \int_1 d\sigma^{(S)} \right] + \int_{m+1} [d\sigma^{(R)} - d\sigma^{(S)}] \quad (2.17)$$

Implicitly the one particle phase space integral in  $\int_1 d\sigma^{(S)}$ , in 2.17, is performed using dimensional regularisation. Subtraction terms are not unique, and there exist a number of completely general methods for calculating them, the most popular of which are that of Dipole subtraction by Catani and Seymour [32] and the FKS subtraction of Frixione, Kunszt and Signer [10]. Both of these methods are reviewed later in this thesis.

### 2.6.1 Overview of Catani Seymour Dipoles

The Catani Seymour dipole subtraction method, which is one of the most popular methods for the calculation of QCD processes at NLO, was introduced in [32], this was later extended in [33] to include massive partons. In this method, subtraction terms

for NLO calculations are formed from a set of universal functions, known as dipoles. Schematically the subtraction term constructed from Catani Seymour dipoles takes the form of some convolution of the dipole functions, and a Born like term, as shown in 2.18.

$$d\sigma^{(s)} = \sum_{\text{Dipoles}} d\sigma^B \otimes dV_{\text{Dipole}} \quad (2.18)$$

These dipole functions are constructed by utilizing the general factorisation of QCD amplitudes in the soft and collinear limits. As it is such kinematic limits that are responsible for the IR singularities of the real term, these results can be used to construct terms with the same singular structures as the real term. For the real term, these factorisation results force it to take the forms 1.32 and 2.9 in the collinear and soft limits respectively. Additionally, in both of these kinematic limits, this factorisation extends to the phase space, which is split into a Born like phase space integral and the integral over the phase space of the unresolved parton; this is schematically written in 2.19.

$$\begin{aligned} \lim_{k_i \rightarrow 0 \text{ or } k_i \parallel k_j} d\phi_{n+1} &= \lim_{k_i \rightarrow 0 \text{ or } k_i \parallel k_j} \prod_{l=1}^{n+1} \frac{d^3 k_l}{2E_l (2\pi)^3} \delta^{(4)}(p_1 + p_2 - \sum_i^{n+1} k_i) \\ &= \frac{d^3 k_i}{2E_i (2\pi)^3} \prod_{l=1}^n \frac{d^3 k_l}{2E_l (2\pi)^3} \delta^{(4)}(p_1 + p_2 - \sum_l^n k_l) \quad (2.19) \end{aligned}$$

The tactic of dipole subtraction is to exploit these factorisations to construct the universal dipole functions. The phase space factorisation firstly allows the subtraction terms to be split into a Born like term, and a dipole function on the unresolved partons' phase space; this partially justifies the structure in 2.18. The form of the dipole functions must follow from the splitting functions from factorisation. Examining the unresolved limits given in equations 2.9 and 1.32, it is seen that for the soft limit the splitting function is parametrised by the soft momenta and the momenta of two other spectator partons; for the collinear limit the splitting is parametrised defined by the two momenta in the collinear limit. So it is apparent that the dipole functions must be constructed from the momenta of three particles, one of which is 'soft' and two of

which can become collinear. The subtraction terms can now be rewritten such that

$$d\sigma^S = \sum_{i \neq j \neq k} \mathcal{D}_{ijk} \quad (2.20)$$

where  $\mathcal{D}_{ijk}$  is composed of the dipole functions. Generally it can be written in the form

$$\mathcal{D}_{ijk} = \sum_{\text{spin, colour}} V_{ijk}(z, y_{ijk}) \mathcal{A}^n(\dots, a_{ij}\dots) \frac{\vec{Q}(a_k) \cdot \vec{Q}(a_{ij})}{\vec{Q}^2(a_{ij})} \mathcal{A}^{n*}(\dots, a_{ij}\dots) \quad (2.21)$$

where  $V_{ijk}$  represents the dipole functions, the remaining terms give the Born like matrix element with colour factors. The full structure of the subtraction term is now clear, the partons  $i$ ,  $j$  and  $k$  are defined to be the emitted, the emitter and the spectator;  $i$  is the parton that becomes unresolved, it can either become soft or collinear to parton  $j$  (other collinear limits are considered with other dipole terms), the spectator  $k$  is then needed to give to parametrise the soft limit. The reduced Born level term, which also includes colour factors from the splittings, replaces the flavours of partons  $i$  and  $j$  with a combined parton  $a_{ij}$ , while the flavour of the spectator is unaffected. However to produce the kinematics for the Born term the momenta of the emitted, emitter and spectator are subject to a kinematic map, 2.22.

$$\{\mathbf{k}_1, \dots, \mathbf{k}_i, \mathbf{k}_j, \mathbf{k}_k, \dots, \mathbf{k}_{n+1}\} \rightarrow \{\hat{\mathbf{k}}_1, \dots, \hat{\mathbf{k}}_{ij}, \hat{\mathbf{k}}_k, \dots, \hat{\mathbf{k}}_n\} \quad (2.22)$$

The momenta of  $i$  and  $j$  are mapped into a combined momenta for the Born term, however unlike for the flavour map the spectator's momenta is in general also mapped. The nature of the map is dependent upon the structure of the partons  $i$ ,  $j$  and  $k$  within the real process, different maps are required for dipoles with all final state partons, and those with different mixes of initial and final state partons; (note, as parton  $i$  is defined to become unresolved it must always be in the final state). The universal dipole functions,  $V_{ijk}$  are in general dependent upon the flavours of the partons  $i$ ,  $j$  and  $k$ , which reflects this dependence on the factorisation results 2.9 and 1.32. It is also useful to separate the dipole functions into sections, dependent upon whether the emitter and spectator partons are in the initial or final state, these sections are given the labels; final-final, initial-final, final-initial and initial-initial (emitter-spectator).

It should be noted that the emitted parton must always be a final state parton if it is to become unresolved. This separation into sections reflects different kinematic mapping and variables that are used in the dipole functions. To obtain the full subtraction term, the dipole subtraction terms must be summed to include all possible partons, in all possible configurations, such that all singularity structures possible in the real term are countered.

The subtraction of the dipole terms described above must also be accompanied by the addition of the integrated term as described in the previous sections. To obtain the integrated term the full sum of all the dipole subtraction terms must be integrated over the phase space of the unresolved parton. This integral can be calculated analytically, and completely generally as the dipole functions are universal; for convenience, this integral is usually performed using dimensional regularisation, as is schematically shown in 2.23.

$$\int_{m+1} d\sigma^{(s)} = \int_m \sum_{\text{Dipoles}} d\sigma^B \otimes \int_1 d^{4-2\epsilon} V_{\text{dipole}} \quad (2.23)$$

The full list of integrated dipole terms is given explicitly in the original papers by Catani and Seymour. The explicit cancellation of poles can then be accomplished by the addition of this term with the virtual piece, and the PDF counter terms.

# Chapter 3

## Review of FKS Subtraction

The concept of a subtraction scheme for the calculation of the real contributions to a next to leading order cross section has been reviewed in the previous chapter, and the example of the popular Catani Seymour dipole subtraction given. As was described in chapter two, a subtraction scheme handles divergences in the real emission contribution of a NLO cross section by subtracting a term with an identical singular structure, giving a finite term. This subtraction term is added back into the cross section after having been integrated over the phase space of the unresolved parton. Subtraction terms are chosen such that the integral can be performed analytically, in dimensional regularisation; this yields a pole structure that must explicitly cancel that of the virtual terms. The subtraction procedure of Frixione, Kunszt and Signer (henceforth FKS), is just such a method and is generally applicable to any process in QCD. It was first formulated in [10], for three jet QCD processes and was expanded upon in [34]. Existing implementations of FKS include the POWHEG box, [35] and MADFKS [36], which is a completely automated implementation of FKS subtraction within MADGRAPH. The FKS subtraction method will be reviewed in this chapter, with a view to its implementation described in later chapters.

### 3.1 Structure of FKS subtraction

The FKS subtraction procedure constructs subtraction terms rather differently to the Catani Seymour dipole method described in chapter two. In the FKS formalism the subtraction terms are constructed by first parameterising the singular structures of the real term, using angular and energy variables; these structures represent regions of phase space where distinct singular limits of the real matrix element exist. The subtraction terms are then formed by applying the relevant singular limits, for each of these structures, to the real term. The subtraction terms are then guaranteed to have the same divergent structures as the real matrix element squared, as they are explicitly constructed from it. This is a somewhat different philosophy to dipole subtraction, whereby universal structures defining the singular limits of any matrix element are calculated. However, like dipole subtraction, FKS relies on the factorisation of the matrix elements in the soft and collinear singular limits, which has been described in chapter one, in order to construct the subtraction terms.

To construct the subtraction terms in FKS, the real  $(n+1)$  particle phase space must be partitioned into the different singular regions of the real term; in FKS the partitioned regions are defined in terms of pairs of partons (in the real matrix element), as is schematically shown in 3.1.

$$d\sigma^{(R)} = \sum_{ij} S_{ij} d\sigma^{(R)} \quad (i, j) \in \mathcal{P}_{\text{FKS}} \quad (3.1)$$

The partition of the phase space is described by a partitioning function  $S_{ij}$ , which is a function of the momenta of partons  $i$  and  $j$ ; the full phase space is recovered after summing over all possible pairs.

$$\sum_{i,j} S_{ij} = 1 \quad (3.2)$$

The set of these pairs, defined as  $\mathcal{P}_{\text{FKS}}$  the set of all FKS pairs, which can represent the FKS singular regions is constrained according to 3.3;

$$\mathcal{P}_{\text{FKS}} = \{3 \leq i \leq n+1 \forall a_i \in \text{SU}(3)_c, 0 \leq j \leq n+1 \forall a_j \in \text{SU}(3)_c, i \neq j\} \quad (3.3)$$

essentially the variable  $i$  can be any final state parton and  $j$  can be any parton in the process (including the initial state) that is not  $i$ , the full set of pairs that obeys

these conditions is the set of FKS pairs. These partition regions described by  $S_{ij}$  are defined such that only unresolved limits associated with the partons  $i$  and  $j$  are allowed; specifically the only limits allowed are parton  $i$  becoming soft, and partons  $i$  and  $j$  becoming collinear. Other unresolved kinematic limits acting on  $S_{ij}$  lead to it vanishing, namely:

$$\lim_{k_n \rightarrow 0} S_{ij} = 0 \quad \text{if } n \neq i \quad (3.4)$$

$$\lim_{k_n || k_m} S_{ij} = 0 \quad \text{if } n, m \neq i, j \quad (3.5)$$

These constraints force certain conditions on the form of the partitioning function in the various unresolved limits. Considering first the soft limit of the parton  $i$ , the definition

$$\lim_{k_i \rightarrow 0} S_{ij} = c_{ij} \quad (3.6)$$

is made for this limit on the partitioning function. By the definitions given in 3.2 and 3.4 it is then required that

$$\sum_j c_{ij} = 1 \quad (3.7)$$

Considering the collinear limit, it is fairly clear from 3.2 and 3.5 that the constraint

$$\lim_{k_i || k_j} S_{ij} + S_{ji} = 1 \quad (3.8)$$

must be obeyed. In the original FKS formulation, the terms  $S_{ij}$  are defined in terms of  $\Theta$  functions; however later work [35] defines them in terms of kinematic variables. There is no unique definition, as any functions that obey the constraints given above are valid for use in FKS; a choice of  $S_{ij}$  is however given in the implementation of FKS described later in this thesis.

After this partition the real term is split into a series of terms,  $S_{ij} d\sigma^{(R)}$ , with the phase space constrained such that only one collinear and one soft singularity are allowed in each term. By splitting up the phase space in this way all the singular regions can be considered and subtracted separately.

## 3.2 Constructing the Subtraction Terms

The FKS subtraction formalism, as has been discussed, relies on a partition of the real term in regions with only specific singular limits of the matrix element; the subtraction terms are then constructed by applying these singular limits to the real term in each of these regions. For the case of the phase space slice,  $S_{ij}d\sigma^{(R)}$ , now written for convenience as  $d\sigma_{ij}^{(R)}$ , only the unresolved limits allowed by  $S_{ij}$  can be applied to  $d\sigma_{ij}^{(R)}$ ; explicitly these are the soft limit of parton  $i$ ,  $E_i \rightarrow 0$ , and collinear limit of partons  $i$  and  $j$ ,  $\cos \theta_{ij} \rightarrow 1$ .

The subtraction terms for  $d\sigma_{ij}^{(R)}$  are then formed by acting these limits on  $d\sigma_{ij}^{(R)}$  itself. This subtraction procedure can be written schematically (for the soft limit) as

$$\int_{n+1} d\sigma_{ij}^{(R)} = \int_n \int_i d\sigma_{ij}^{(R)}|_{E_i \rightarrow 0} + \int_{n+1} d\sigma_{ij}^{(R)} - d\sigma_{ij}^{(R)}|_{E_i \rightarrow 0} \quad (3.9)$$

where the term  $\int_i d\sigma_{ij}^{(R)}|_{E_i \rightarrow 0}$  is understood to be integrated over the one particle phase space such that a pole structure can be extracted and explicitly cancelled with loop contributions.

To write down the subtraction terms, the phase space integral over the matrix element squared must be considered; for the phase space slice  $S_{ij}d\sigma^{(R)}$  this can be written in terms of a product of the phase spaces of all final state particles.

$$d\sigma_{ij}^{(R)} = S_{ij}d\sigma^{(R)} = \int \prod_k^{n+1} d\phi_k \delta^4(p_1 + p_1 - \sum_{i=1}^{n+1} k_i) S_{ij} \mathcal{M}(r_{n+1}, \{k_{n+1}\}) \frac{J_n(\{k_{n+1}\})}{\mathcal{N}(a_{n+1})} \quad (3.10)$$

Where  $\mathcal{N}(a_{n+1})$  is the symmetry factor which is included to account for the presence of identical particles in the final state. The phase space integral in 3.10 is simply product of the phase spaces for all final state particles, and it is convenient for this discussion to separate the phase space of particle  $i$ ; which according to the  $S_{ij}$  functions is the only particle in this term with unresolved limits.

$$\prod_k^{n+1} d\phi_k = d\phi_i \prod_{k,k \neq i}^{n+1} d\phi_k = d\phi_i d\Phi_n \quad (3.11)$$

To enable the construction of the subtraction term, the form one particle phase  $d\phi_i$ , must be considered. This is explicitly given in 3.12 using dimensional regularisation formalism of chapter one; the use of which will allow the construction of the subtraction terms.

$$d\phi_i = \frac{d^{3-2\epsilon}k_i}{(2\pi)^{3-2\epsilon}2k_i^0} = \frac{1}{2(2\pi)^{3-2\epsilon}} \left(\frac{\sqrt{s}}{2}\right)^{2-2\epsilon} \xi_i^{1-2\epsilon} (1-y_{ij}^2)^{-\epsilon} d\xi_i dy_{ij} d\Omega_i^{2-2\epsilon} \quad (3.12)$$

Where  $\xi_i = \frac{2E_i}{\sqrt{s}}$  and  $y_{ij} = 1 - \frac{k_i \cdot k_j}{E_i E_j} = \cos \theta_{ij}$ ; these variables are understood to be given in the partonic centre of mass frame. The construction of the subtraction terms will now be considered for a generic function of the one particle phase space; for the purpose of simplification, at first only the energy variable  $\xi_i$  will be considered. The integral given in 3.13 represents the integral of this function over the (energy) part of the phase space.

$$\int d\xi_i \xi_i^{-1-2\epsilon} g(\xi_i) \quad (3.13)$$

If it is supposed that this integral is singular in the soft limit of  $\xi_i$ , the subtraction procedure can be applied to 3.13 to give a finite integral and an explicitly singular term. In FKS it is the singular limit of the function itself which is used as the subtraction term, in the case of 3.13 the soft limit of  $g(\xi_i)$ . To demonstrate this subtraction the soft limit of this function,  $\Theta(\xi_i - \xi_{\text{cut}}) \xi_i^{-1-2\epsilon} g(0)$  (where the theta function represents a phase space cut whose function will be explained later) is simply added and subtracted as is shown in 3.14.

$$\int d\xi_i \left\{ \Theta(\xi_i - \xi_{\text{cut}}) \xi_i^{-1-2\epsilon} g(0) + \xi_i^{-1-2\epsilon} (g(\xi_i) - \Theta(\xi_i - \xi_{\text{cut}}) g(0)) \right\} \quad (3.14)$$

To give the equivalent of the integrated term, the integral over  $\xi_i$  is performed on one of the soft limit terms. As this is formally divergent, dimensional regularisation has implicitly been used to write down the result.

$$\int d\xi_i \xi_i^{-1-2\epsilon} g(\xi_i) = -\frac{\xi_{\text{cut}}^{-2\epsilon}}{2\epsilon} g(0) + \int d\xi_i \frac{g(\xi_i) - \Theta(\xi_i - \xi_{\text{cut}}) g(0)}{\xi_i} (1 - 2\epsilon \log \xi_i + \mathcal{O}(\epsilon^3)) \quad (3.15)$$

This expression now mimics the form for a schematic subtraction for the soft term given in equation 3.9, with a subtracted piece plus a term with an explicit pole structure easily integrated over  $d\xi_i$ . The variable  $\xi_{\text{cut}}$ , introduced in 3.14, parameterises

the phase space cut and it should be noted that the above expression as a whole has no dependence upon this parameter. This result can then be used to give the identity

$$\xi_i^{-1-2\epsilon} = -\frac{\xi_{\text{cut}}^{-2\epsilon}}{2\epsilon}\delta(\xi_i) + \left(\frac{1}{\xi_i}\right)_c - 2\epsilon\left(\frac{\log \xi_i}{\xi_i}\right)_c \quad (3.16)$$

Where

$$\left(\frac{1}{\xi_i}\right)_c f(\xi_i) = \frac{1}{\xi_i} (f(\xi_i) - \Theta(\xi_{\text{cut}} - \xi_i)f(0)) \quad (3.17)$$

Analogously a similar term for the collinear variable  $y_{ij}$  can be shown to be

$$(1 - y_{ij})^{-1-\epsilon} = -\frac{(y_{\text{cut}})^{-\epsilon}}{\epsilon}\delta(1 - y_{ij}) + \left(\frac{1}{1 - y_{ij}}\right)_c + O(\epsilon) \quad (3.18)$$

Where

$$\left(\frac{1}{1 - y_{ij}}\right)_c f(y_{ij}) = \frac{1}{1 - y_{ij}} [f(y_{ij}) - \Theta(y_{ij} - 1 + y_{\text{cut}})f(1)] \quad (3.19)$$

The subtraction procedure for a generic function,  $g(\xi_i)$ , allows the writing of the above results for the soft and collinear variables  $\xi_i$  and  $y_{ij}$ ; which perform the subtraction of the singular limits of these variables. Given that the one particle phase space integral for a parton  $i$ , which was parameterised in 3.12, also implicitly appears in the the expression for  $d\sigma_{ij}^{(R)}$  in 3.10, the results for  $\xi_i^{-1-2\epsilon}$  and  $(1 - y_{ij})^{-1-\epsilon}$  can also be applied to  $d\sigma_{ij}^{(R)}$ . Since the only singular limits which can apply, to  $d\sigma_{ij}^{(R)}$ , are precisely those limits considered in 3.17 and 3.18; these results can be used to construct the subtraction terms. Forming the subtraction terms from 3.17 and 3.18 instantly splits the calculation into terms proportional to a delta function, which will be the basis for the integrated terms, and a real cross section with subtracted singular limits expressed in the form of plus distributions.

The terms proportional to delta functions can be analytically integrated over the one particle phase space, which, as dimensional regularisation is used will give an explicit pole structure; these constitute the integrated terms, which after this procedure become functions on the Born phase space. The remaining terms contain plus-like distributions, which implicitly subtract the singular limits of the real term; these correspond to the real subtracted term. The finite, real subtracted term can be written as

$$d\sigma_{ij}^{(RS)} = \left(\frac{1}{\xi_i}\right)_c \left(\frac{1}{1 - y_{ij}}\right)_c \xi_i^2 (1 - y_{ij}) \mathcal{M}^{(n+1)}(r_{n+1}) S_{ij} \frac{J_n}{\mathcal{N}(a_{n+1})} d\Phi_{n+1} \quad (3.20)$$

Where for the real subtracted term the limit  $\epsilon \rightarrow 0$  has been taken, hence these terms are now calculated in the standard four dimensions. Schematically this finite, real subtracted piece is of the following form

$$\begin{aligned} d\sigma_{ij}^{(RS)} = d\sigma_{ij}^{(R)} - \frac{1}{\xi_i(1-y_{ij})} & [\Theta(\xi_{\text{cut}} - \xi_i)H(0, y_{ij}) + \Theta(y_{ij} - 1 + y_{\text{cut}})H(\xi_i, 1) \\ & - \Theta(\xi_{\text{cut}} - \xi_i)\Theta(y_{ij} - 1 + y_{\text{cut}})H(0, 1)] d\xi_i dy_{ij} \quad (3.21) \end{aligned}$$

Where the function  $H(\xi_i, y_{ij})$  is defined to be.

$$\begin{aligned} H(\xi_i, y_{ij}) = \xi_i^2(1-y_{ij})\mathcal{M}^{(n+1)}(r_{n+1})S_{ij} \\ \frac{J_n}{\mathcal{N}(a_{n+1})} \frac{1}{2(2\pi)^3} \left(\frac{\sqrt{S}}{2}\right)^2 d\xi_i dy_{ij} d\Omega_i^2 d\Phi_n \quad (3.22) \end{aligned}$$

The subtraction terms, as schematically given in 3.21, are split into three terms; the soft, collinear and soft-collinear limit of  $d\sigma_{ij}^{(RS)}$ . To write down explicit expressions for these subtraction terms, the factorisation of the QCD amplitudes in soft and collinear limits can be used; use of these results to show expressions for real subtraction terms is delayed until the next section.

### 3.3 Real Subtraction Terms

The previous section discusses the construction of the subtraction terms for a generic phase space slice of the real term,  $d\sigma_{ij}^{(RS)}$ , the real subtraction part of this term is then given explicitly in 3.20. The complete subtraction structure for FKS is simply the sum of the subtraction terms of all the individual phase space slices, as expressed by 3.23.

$$d\sigma^{(RS)} = \sum_{ij} d\sigma_{ij}^{(RS)} \quad (3.23)$$

There is nothing unique about the results in 3.20, for a generic slice,  $d\sigma_{ij}^{(RS)}$  of the real term; and as a result they can be applied to any partition of the phase space;

The complete real subtraction term, in FKS, is therefore simply the sum of these terms for all the phase space slices, as given in 3.24.

$$d\sigma^{(RS)} = \sum_{i,j \in \mathcal{P}_{FKS}} \left(\frac{1}{\xi_i}\right)_c \left(\frac{1}{1-y_{ij}}\right)_c \xi_i^2 (1-y_{ij}) \mathcal{M}^{(n+1)}(r_{n+1}) S_{ij} \frac{J_n}{\mathcal{N}(a_{n+1})} d\Phi_{n+1} \quad (3.24)$$

For each partition of the phase space the plus distributions enforce the subtraction of these unresolved singular limits, which are divided into the soft subtraction term and the collinear subtraction term which are subtracted separately. In addition a soft-collinear subtraction term, subject to both unresolved limits, and with a change of sign, is included from the plus distributions to ensure this combined limit is not subject to double counting from other subtraction terms. These subtraction terms from plus distributions are given schematically in the previous section as the singular limit of the real term which they subtract, for example the soft term

$$\Theta(\xi_{\text{cut}} - \xi_i) H(0, y_{ij})$$

where  $H(\xi_i, y_{ij})$  is properly defined in equation 3.22. The approach that is taken, and which will allow FKS subtraction to be applied algorithmically to a generic process, to calculate these unresolved limits will be to utilise factorisation of QCD amplitudes. The factorisation of QCD matrix elements is discussed in chapter one, and in the case of FKS allows the soft or collinear unresolved limits of the real term to be written in terms of a Born like term and a generic function of the unresolved momenta. The subtraction terms for FKS, which are entirely comprised of such limits of the real term, can then be written in this fashion and hence given a concrete functional form that is analogous to that of Catani Seymour dipoles.

The factorisation, in the soft and collinear kinematic limits, also applies to the phase space; the phase space for the real term in such limits factorises into a Born like phase space, which is acted on by the Born level term, and a one particle phase space of the soft/collinear parton. This phase space factorisation is discussed, in the context of Catani Seymour subtraction, in chapter two and also applies to the present discussion. For the calculation of subtraction terms this Born like phase space must be computed from the from the real phase space, such that this factorisation

occurs and that both phase spaces are equivalent in either the soft or collinear limit. Computationally this is accomplished by a set of momentum maps, from the real to the Born set, and vary according the subtraction term; unlike in Catani Seymour these maps are not specified for FKS. Discussion of these maps is withheld until the implementation is described in chapter four.

For the remainder of this section the explicit form of the subtraction terms, using the QCD factorisation results will be reviewed.

### 3.3.1 Soft Term

The soft subtraction term, given implicitly as the unresolved limit of  $H(0, y_{ij})$  in 3.21, can, for a generic phase space slice, be considered by taking the soft limit of 3.22

$$\begin{aligned} d\sigma^{S,\text{soft}} &= \frac{1}{\xi_i(1-y_{ij})} \left[ \xi_i^2(1-y_{ij}) \mathcal{M}^{(n+1)} S_{ij} \frac{J_n}{\mathcal{N}(a_{n+1})} d\Phi_{n+1} \right]_{\xi_i \rightarrow 0} \\ &= \frac{1}{\xi_i(1-y_{ij})} [\xi_i^2(1-y_{ij}) \mathcal{M}^{(n+1)}]_{\xi_i \rightarrow 0} S_{ij}(\xi_i = 0) \frac{J_n}{\mathcal{N}(a_{n+1})}(\{\hat{k}\}) d\phi_i d\hat{\phi}_n \quad (3.25) \end{aligned}$$

To calculate this limit, as has been discussed, the factorisation of QCD amplitudes is made use of; the soft limit of a generic QCD matrix element squared is quoted from chapter one to be

$$\lim_{\xi_i \rightarrow 0} \xi_i^2(1-y_{ij}) \mathcal{M}^{(n+1)}(\{k\}_{n+1}) = \delta_{ga_i} 4\pi\alpha_s \xi_i^2(1-y_{ij}) \sum_{n \neq m} \frac{\hat{k}_n \cdot \hat{k}_m}{\hat{k}_n \cdot \hat{k}_i \hat{k}_m \cdot \hat{k}_i} \mathcal{M}_{nm}^{(n)}(\{\hat{k}\}_n) \quad (3.26)$$

The effect of the soft limit on the momenta is formally taken to be equivalent to performing a map on the momenta, the notation of  $\hat{k}$  is taken to indicate the mapping. It is noted that this term, due to the  $\xi_i^2$  term is in fact finite in this limit; this is a general observation of the singular limits of  $H(\xi_i, y_{ij})$ , which despite containing divergent matrix elements is constructed such that it is in fact finite. This forces the result that the singular part of the subtraction term is solely the result of  $\frac{1}{\xi_i(1-y_{ij})}$  in the plus distributions.

### 3.3.2 Collinear Term

The collinear subtraction term, like the soft term, is given implicitly in the subtracted real term in 3.21 via the plus distribution for  $y_{ij}$ . This term can be read off to be

$$\begin{aligned} d\sigma^{S,\text{coll}} &= \frac{1}{\xi_i(1-y_{ij})} \left[ \xi_i^2(1-y_{ij}) \mathcal{M}^{(n+1)} S_{ij} \frac{J_n}{\mathcal{N}(a_{n+1})} d\Phi_{n+1} \right]_{y_{ij} \rightarrow 1} \\ &= \frac{1}{\xi_i(1-y_{ij})} [\xi_i^2(1-y_{ij}) \mathcal{M}^{(n+1)}]_{y_{ij} \rightarrow 1} S_{ij}(y_{ij}=1) \frac{J_n}{\mathcal{N}(a_{n+1})} (\{\hat{k}\}) d\phi_i d\hat{\Phi}_n \end{aligned} \quad (3.27)$$

Where again the effect of the collinear limit on the phase space integral is taken to give the phase space integral over the mapped momenta. Again to calculate this term, the collinear limit of the matrix element squared is considered; the well known result is quoted from chapter one and is given by

$$\begin{aligned} \lim_{y_{ij} \rightarrow 1} \xi_i^2(1-y_{ij}) \mathcal{M}^{(n+1)}(\{k\}_{n+1}) &= \frac{16\pi\alpha_s}{z_S} \bar{P}_{a_j a_{ij}}^{(0)}(z) \mathcal{M}^{(n)}(r_{[i]}^{a_{ij}}, \{\hat{k}\}_n) + \\ &\quad \frac{16\pi\alpha_s}{z_S} \bar{Q}_{a_j a_{ij}}(z) \tilde{\mathcal{M}}^{(n)}(r_{[i]}^{a_{ij}}, \{\hat{k}\}_n) \end{aligned} \quad (3.28)$$

where again the effect of the limit on the momenta is taken to be equivalent to mapping the momenta. It is noted that this term, much like the soft term, is in fact finite in this limit due to the appearance of the factor  $1-y_{ij}$ ; as has been noted the singular part is the result of the term  $\frac{1}{1-y_{ij}}$  in the plus distributions.  $P_{a_j a_{ij}}^{(0)}(z)$  are the Altarelli-Parsi splitting functions, where  $\bar{P}(z) = (1-z)P(z)$ . The splitting functions present in this term, the Altarelli-Parsi splitting functions  $P_{a_j a_{ij}}^{(0)}(z)$  (where  $\bar{P}(z) = (1-z)P(z)$ ) and the functions  $\bar{Q}(z)$  associated with the angular term in the expression are given as functions of the fractional energy,  $z$ , of the parton  $j$  after splitting (where this splitting would give the  $n+1$  parton process for the real). For the final state collinear term the fractional energy is defined to be  $z = \frac{E_j}{E_j + E_i}$ , which after the phase space mapping is given by  $z = 1 - \frac{E_i}{E_{ij}}$ . For initial state terms this fractional energy is instead given by  $z = 1 - \xi_i$ . The second term in the expression is given by a splitting kernel,  $\bar{Q}(z)$  and a term  $\tilde{\mathcal{M}}^{(n)}(\{\hat{k}\}_n)$ , which is known as the reduced matrix element; as has been shown in chapter one this term is the result of spin dependence of the splitting functions, which only occurs for gluons. Generally an integral over the phase space would see this term vanish, however it must in principle be included to

avoid large numerical instabilities in the integration. Its form is discussed in chapter one and is given explicitly in appendix B.

### 3.3.3 Soft Collinear Term

The soft collinear limit, which is included as one of the subtraction terms has not been included as a limit above. To obtain this term, the soft limit of the collinear term can be applied (the reverse application of limits will also yield the same result but it is somewhat easier to obtain this way) this yields

$$\lim_{\xi_i \rightarrow 0, y_{ij} \rightarrow 1} \xi_i^2 (1 - y_{ij}) \mathcal{M}^{(n+1)}(\{k\}_{n+1}) = \delta_{ga_i} \frac{16\pi\alpha_s}{s} \bar{P}_{a_j a_{ij}}^{(0)}(1) \mathcal{M}^{(n)}(\{\hat{k}\}_n) \quad (3.29)$$

It is noted that this term, which has a different sign to the other terms, exists to prevent double counting of singular limits. Essentially it ensures that the region of the soft-collinear limit is subtracted only once (it is implicitly included in both the soft and collinear terms).

## 3.4 Integrated terms

The integrated terms of a generic subtraction scheme are simply given by the integral of the subtraction terms over the phase space of the unresolved parton in the real process.

$$d\sigma^{(I)} = \int_1 d\sigma^{(\text{sub})} \quad (3.30)$$

The subtraction terms are by construction divergent over this integral, and to be written down a regularisation scheme is required; the choice made here will be that of dimensional regularisation. For FKS subtraction, in which dimensional regularisation has been used in the derivation of the structure, this seems an appropriate choice. The pole structure from the complete integrated term will then cancel the pole structure from the virtual terms (assuming loop integrals are calculated using dimensional regularisation as seems sensible). For FKS the integrated terms can be obtained from the first term of the  $\xi_i^{1-2\epsilon}$  and  $y_{ij}^{-1-\epsilon}$  expressions given in section 3.2. These terms

are proportional to delta functions, and so are in principle not difficult to integrate. The section below will simply quote the results of these integrals, a more complete derivation of the integrated terms is given in [10]. As with the real subtraction terms, the setting of matrix elements squared to  $\xi_i = 0$  or  $y_{ij} = 1$  is conducted by using the factorisation of these terms in the soft and collinear limits. The appearance of Born matrix elements in the integrated terms are the result of using this factorisation.

### 3.4.1 Soft Term

The integrated soft term can simply be read off from the section 3.2, it is given by

$$d\sigma_{ij}^{(s)} = -\frac{\xi_{\text{cut}}^{-2\epsilon}}{2\epsilon} \delta(\xi_i) \xi_i^2 \mathcal{M}^{(n+1)}(r_{n+1}) S_{ij} \frac{J_n}{\mathcal{N}(a_{n+1})} \frac{1}{2(2\pi)^{3-2\epsilon}} \left(\frac{\sqrt{S}}{2}\right)^{2-2\epsilon} (1-y_{ij}^2)^{-\epsilon} d\xi_i dy_{ij} d\Omega_i^{2-2\epsilon} d\phi_n \quad (3.31)$$

Performing the one particle phase space integral (ie the integrals of  $\xi_i, y_{ij}$  and  $\Omega_i$ ) this becomes

$$d\sigma_{ij}^{(I,S)} = \delta_{ga_i} \frac{\alpha_s}{2\pi} \frac{1}{2} \sum_{n \neq m} (\mathcal{I}_{nm}^{\text{div}} + \mathcal{I}_{nm}^{\text{reg}}) \mathcal{M}_{nm}(r_{n,[i]}) c_{ij} \frac{J_n}{\mathcal{N}(a_{n+1})} d\phi_n \quad (3.32)$$

Where  $c_{ij}$  is the soft limit of  $S_{ij}$ . This has the property  $\sum_j c_{ij} = 1$ , so

$$d\sigma_i^{(I,S)} = \sum_j d\sigma_{ij}^{(I,S)} = \delta_{ga_i} \frac{\alpha_s}{2\pi} \frac{1}{2} \sum_{n \neq m} (\mathcal{I}_{nm}^{\text{div}} + \mathcal{I}_{nm}^{\text{reg}}) \mathcal{M}_{nm}(r_{n,[i]}) \frac{J_n}{\mathcal{N}(a_{n+1})} d\phi_n \quad (3.33)$$

The index  $i$ , representing the soft particle from the  $n + 1$  matrix element has no real effect on this term. It can therefore be summed over trivially, the effect is to change from the normalisation factor from the real process,  $\mathcal{N}(a_{n+1})$  to the normalisation factor for the Born process. This sum now gives the total soft subtraction term.

$$\begin{aligned} d\sigma^{(I,S)} &= \sum_i d\sigma_i^{(I,S)} = \frac{1}{2} \frac{\alpha_s}{2\pi} \sum_{n \neq m} (\mathcal{I}_{nm}^{\text{div}} + \mathcal{I}_{nm}^{\text{reg}}) \mathcal{M}_{nm}(r_{n,[i]}) \frac{J_n}{\mathcal{N}(a_n)} d\phi_n \\ &= \frac{1}{2} \frac{\alpha_s}{2\pi} \sum_{n \neq m} (\mathcal{I}_{nm}^{\text{div}} + \mathcal{I}_{nm}^{\text{reg}}) d\sigma_{nm}^{(B)}(r_n) \end{aligned} \quad (3.34)$$

This is the total integrated soft term. The quantities  $\mathcal{I}_{nm}^{\text{div}}$  and  $\mathcal{I}_{nm}^{\text{reg}}$  are given by

$$\mathcal{I}_{nm}^{\text{reg}} = \left[ \log^2 \frac{\xi_{\text{cut}} S}{Q^2} + \log \frac{\xi_{\text{cut}}^2 S}{Q^2} \log \frac{k_n \cdot k_m}{2E_n E_m} - \text{Li}_2 \left( \frac{k_n \cdot k_m}{2E_n E_m} \right) + \frac{1}{2} \log^2 \frac{2k_n \cdot k_m}{E_n E_m} - \log \left( 4 - \frac{2k_n \cdot k_m}{E_n E_m} \right) \log \frac{k_n \cdot k_m}{2E_n E_m} - 2 \log^2 2 \right] \quad (3.35)$$

$$\mathcal{I}_{nm}^{\text{div}} = \frac{(4\pi)^\epsilon}{\Gamma(1-\epsilon)} \left( \frac{\mu_R^2}{Q^2} \right)^\epsilon \left[ \frac{1}{\epsilon^2} - \frac{1}{\epsilon} \left( \log \frac{2k_n \cdot k_m}{Q^2} - \log \frac{4E_n E_m}{\xi_{\text{cut}}^2 S} \right) \right] \quad (3.36)$$

This is the result assuming all coloured objects in the process are massless. However when there are massive coloured particles the above is modified, the results of which are shown in appendix B. It is interesting to note that massive partons enter this term (if they exist in the process) not through FKS pairs (from which massive particles are excluded) but from considering the eikonal limit, which includes a sum over all coloured objects. The scale  $Q^2$  is again the Ellis-Sexton scale which also appears in the virtual terms.

### 3.4.2 Final state collinear terms

The integrated collinear term for final state partons, that is both  $i$  and  $j$  are final state partons, can be read off to be

$$d\sigma^{(C)} = -\frac{(y_{\text{cut}})^{-\epsilon}}{\epsilon} \delta(1 - y_{ij}) \left[ \left( \frac{1}{\xi_i} \right)_c - 2\epsilon \left( \frac{\log \xi_i}{\xi_i} \right)_c \right] \xi_i^2 \mathcal{M}^{(n+1)}(r_{n+1}) S_{ij} \frac{J_n}{\mathcal{N}(a_{n+1})} \frac{1}{2(2\pi)^{3-2\epsilon}} \left( \frac{\sqrt{S}}{2} \right)^{2-2\epsilon} (1 - y_{ij}^2) d\xi_i dy_{ij} d\Omega_i^{2-2\epsilon} d\phi_n \quad (3.37)$$

The one particle phase space integrals can be performed and the result for the final state collinear term is given below.

$$d\sigma^{(I,C)} = \frac{\alpha_s}{2\pi} \frac{(4\pi)^{-\epsilon}}{\Gamma(1-\epsilon)} \left( \frac{\mu^2}{Q^2} \right)^\epsilon \frac{1}{\epsilon} \left[ \gamma(a_j) - 2C(a_j) \log \frac{2E_j}{\xi_{\text{cut}} \sqrt{s}} \right] d\sigma^{(B)}(r_n) + \frac{\alpha_s}{2\pi} d\sigma^{(B)}(r_n) \sum_j \left[ \gamma'(a_j) - \log \frac{sy_{\text{cut}}}{2Q^2} \left( \gamma(a_j) - 2C(a_j) \log \frac{2E_j}{\xi_{\text{cut}} \sqrt{s}} \right) + 2C(a_j) \left( \log^2 \frac{2E_j}{\sqrt{s}} - \log^2 \xi_{\text{cut}} \right) - 2\gamma(a_j) \log \frac{2E_j}{\sqrt{s}} \right] \quad (3.38)$$

An implicit sum over the  $i$  index has been performed, as for the soft term, this has the same effect of changing the normalisation factors. Again the scale  $Q^2$  is that

of Ellis-Sexton scale which also appears in the virtual terms. The terms  $\gamma(a_j)$  and  $\gamma'(a_j)$  is defined for quarks and gluons as

$$\gamma(g) = \frac{N_c^2 - 1}{2N_c} \quad \gamma'(g) = \frac{67}{9}C_A - \frac{2\pi^2}{3}C_A - \frac{23}{9}T_F N_F \quad (3.39)$$

$$\gamma(q) = \frac{3}{2}C_F \quad \gamma'(q) = \frac{13}{2}C_F - \frac{2\pi^2}{3}C_F \quad (3.40)$$

where  $N_F$  is defined as the number of quark flavours.

### 3.4.3 Initial state collinear term

The collinear limit with any initial state parton (in the FKS pair  $i$  is restricted to be in the final state, hence only  $j$  can be in the initial state), like other collinear limits for the real term is in principle singular, as such it has an associated subtraction term in FKS. The associated integrated subtraction term for this piece is completely analogous to the term given for final state collinear term in the previous subsection. However the reason for the separate consideration here is their combination with terms from the PDFs. Divergences from the initial state collinear limits are not completely cancelled by loop contributions, however these are cancelled by the inclusion of the PDF counter terms discussed in chapters one and two. It is recalled that these are necessary to maintain the distinction between the hard process considered in the partonic cross section and the softer terms which contribute via PDFs. To  $\mathcal{O}(\alpha_s)$  the PDF counter terms to the partonic cross section are given by

$$d\sigma_1^{\text{cnt}}(k_1, k_2) = \frac{\alpha_s}{2\pi} \frac{1}{\Gamma(1 - \epsilon)} \left( \frac{4\pi\mu^2}{\mu_f^2} \right)^\epsilon \sum_d \int dx \left( P_{da}(x) \frac{1}{\epsilon} + K_{da}(x) \right) d\sigma_{db}^{(B)}((1 - \xi_i)k_1, k_2) \quad (3.41)$$

where  $K_{da}$  are regularisation scheme dependent functions, for  $\overline{\text{MS}}$ , which is the scheme employed for all results in this work  $K_{ad} = 0$ . When combined with the counter term

from the PDF the initial state integrated term becomes

$$\begin{aligned}
d\sigma_j^{(C_{in}+cnt)} &= \frac{\alpha_s}{2\pi} \left( \frac{(4\pi)^{-\epsilon}}{\Gamma(1-\epsilon)} \left( \frac{\mu^2}{Q^2} \right)^\epsilon \frac{1}{\epsilon} - \log \frac{\mu_f^2}{Q^2} \right) \\
&\quad \times [\gamma(a_1) + 2C(a_j) \log \xi_{cut}] d\sigma^{(B)}(r_{n[i]}) \\
&\quad + \frac{\alpha_s}{2\pi} \sum_{a_{ij}} \left\{ \xi_i P_{a_{ij}a_j}^{(0)} (1-\xi_i) \left[ \left( \frac{1}{\xi_i} \right)_c \log \frac{sy_{cut}}{2\mu^2} + 2 \left( \frac{\log \xi_i}{\xi_i} \right) \right] \right. \\
&\quad \left. - \xi_i P_{a_{ij}a_j}^{(1)} (1-\xi_i) \left( \frac{1}{\xi_i} \right)_c \right\} d\sigma^{(B)}(r_{n[i]}^{a_{ij}}, (1-\xi_i)k_j) d\xi_i \quad (3.42)
\end{aligned}$$

An implicit sum over the  $i$  index has been performed for the collinear part, as was done for the soft term, this has the same effect of changing the normalisation factors. Again the scale  $Q^2$  is that of Ellis-Sexton scale which also appears in the virtual terms.

# Chapter 4

## Implementation

The following chapter will describe the implementation of the FKS subtraction, which is reviewed in the previous chapter, into the event generator AMEGIC++ [6], part of the SHERPA Monte Carlo event generator package [37]. This allows the automatic calculation, of the real and subtraction terms, of a NLO cross section within the FKS method; at present this implementation is restricted to the case of massless partons. The actual calculation of FKS subtracted cross sections requires more details than the review of the method given in chapter three. Most of these relate to the subtracted real term, which is often the bottleneck for any NLO calculation (for many processes the virtual term is bottleneck). These include choices for the FKS partitioning functions, and the kinematic mapping of the phase space for subtraction terms; these are issues which are not specified by the FKS subtraction scheme and are thus details of the implementation.

The biggest issue associated with the implementation are the aforementioned kinematic maps, associated with  $n$  parton matrix elements in the subtraction terms for the  $n + 1$  matrix elements. These maps, from  $n + 1$  to  $n$  parton kinematics, must have the same limiting behaviour as the subtraction terms themselves (ie soft or collinear); such maps are discussed in depth for all relevant limits and include a distinction between initial and final state partons. The explicit forms of the subtraction terms are given and the organisation of the real and subtraction terms in the code are discussed. Additionally the validity of the implementation is tested, and the results

are discussed.

## 4.1 Partitioning Functions

The construction of subtraction terms in the FKS formalism relies upon a partition of phase space of the real term, as was reviewed in chapter three; each partition of the phase space must allow only a restricted set of unresolved limits of the real term. In FKS this is accomplished by the introduction of partitioning functions, which in chapter three are labelled as  $S_{ij}$ ; the subscript  $ij$  refers to the FKS pair  $i,j$ . For the general description of FKS the precise form of these variables is not necessary, however the form is restricted by the constraints, described in more detail in chapter three, but are also summarised below.

$$\begin{aligned} \lim_{k_i \rightarrow 0} S_{ij} &= c_{ij} \quad \text{where} \quad \sum_j c_{ij} = 1 \\ \lim_{k_i || k_j} S_{ij} + S_{ji} &= 1 \quad \lim_{k_n \rightarrow 0} S_{ij} = 0 \quad \text{if} \quad n \neq i \\ \lim_{k_n || k_m} S_{ij} &= 0 \quad \text{if} \quad n, m \neq i, j \end{aligned}$$

The choice of partitioning functions,  $S_{ij}$  is, as has been discussed, not unique as any set of functions obeying the constraints outlined in chapter three are appropriate. However this section will describe the functional form of  $S_{ij}$  used in this implementation.

The original FKS paper [10] gave the partitions in terms of  $\Theta$  functions, while other implementations such as [38] use functions of products,  $k_n \cdot k_m$ . This work will utilise the partition functions defined in [36]; these are based on angular and energy variables, as FKS is itself and are shown in 4.1 to 4.6.

$$S_{ij} = \frac{1}{\mathcal{D}d_{ij}} h_{ij}(z_{ij}) \quad z_{ij} = \frac{E_i}{E_i + E_j} \quad (4.1)$$

$$d_{nm} = \left( \frac{2E_n}{\sqrt{s}} \right)^{a_s} \left( \frac{2E_m}{\sqrt{s}} \right)^{a_s} (1 - \beta_n \beta_m \cos \theta_{nm}) \quad \beta_n = \sqrt{1 - \frac{m_n^2}{E_n^2}} \quad (4.2)$$

Where  $a_s, b_s$  are arbitrary real, positive parameters; for this implementation the choice  $a_s = 1$  and  $b_s = 1$  has been used.

$$\mathcal{D} = \sum_{kl \in \mathcal{P}_{FKS}} \frac{1}{d_{kl}} h_{kl} \quad (4.3)$$

$$h_{ij} = \begin{cases} 1 & \forall j \leq 2 \\ h(z) & \forall j \geq 3 \end{cases} \quad (4.4)$$

$$h(z) = \frac{(1-z)^{2a_h}}{z^{2a_h} + (1-z)^{2a_h}} \quad a_h = 1 \quad (4.5)$$

Again  $h(z)$  does not have a unique choice, but it must obey

$$\lim_{z \rightarrow 0} h(z) = 1 \quad \lim_{z \rightarrow 1} h(z) = 0 \quad h(z) + h(1-z) = 1 \quad (4.6)$$

These properties are required from the definition of the partitioning function, the first terms ensure the correct soft limits for  $i$  and  $j$  and the final term that  $\lim_{k_i || k_j} S_{ij} + S_{ji} = 1$  (for final state  $j$ ).

### 4.1.1 Some efficiencies

The general form of the partitioning function  $S_{ij}$  is given in the section above. However in the implementation it is possible to minimise the number of subtraction terms and therefore speed up calculations, by alternating the form of  $S_{ij}$  under certain conditions. To make such alterations, it is useful to compare unresolved limits allowed by partitioning functions which differ only in the order of partons; for example  $S_{ij}$  and  $S_{ji}$ . Such partitions will allow the same collinear limit of partons  $i$  and  $j$ , but will however admit different soft limits. For example  $S_{ij}$  will admit the soft limit of parton  $i$  and  $S_{ji}$  that of  $j$ . This is relevant to the discussion because, under certain conditions, the soft limit of a parton may not lead to a singular form of the real matrix element. This occurs for partons which are not gluons, and as a result it is not necessary to construct subtraction terms for such unresolved limits.

As a result some of the partitions  $S_{ji}$  can be neglected if parton  $j$  is not gluonic, as the collinear limit can be accommodated in  $S_{ij}$ ; given an appropriate modification of  $S_{ij}$ . For FKS pairs  $(i,j)$ , both of which are in the final state and which contain only

one gluon, such a modification would require the results  $\lim_{y_{ij} \rightarrow 1} S_{ij} = 1$  and  $S_{ji} = 0$ . To accomodate this, the partitioning functions defined in 4.4 can be modified to take the form given in 4.7 to 4.8; with other elements of the partitioning functions remaining unchanged from those definitions given in 4.1 to 4.6.

$$h_{ij} = 1 \quad \text{if } a_i \in g, \quad a_j \notin g \quad (4.7)$$

$$h_{ji} = 0 \quad \text{if } a_i \in g, \quad a_j \notin g \quad (4.8)$$

Additionally for FKS pairs where neither parton is gluonic limits, and hence where neither soft subtraction term is necessary, a similar modification of the partitioning functions can be made to 4.7. Analogously to the one gluon case, the choice can be made to set one contribution to zero. In this case the choice

$$h_{ij} = 1 \quad h_{ji} = 0 \quad \forall i < j \quad (4.9)$$

is made.

## 4.2 Integrated Terms

The integrated subtraction terms of any subtraction scheme, are formed by an analytic integral of a subtraction term over a one particle phase space, which is somehow factorised from a Born level phase space; in FKS this is the phase space of an unresolved parton in either a soft or collinear limit.

The integrated term therefore always lies in the Born level phase space. The organisation of the calculation in AMEGIC++ utilises this fact by performing the calculation of the Born and integrated terms at the same stage. In this respect the organisation of the integrated term in the FKS implementation differs little from the treatment of integrated subtraction terms in the Catani Seymour implementation in AMEGIC++ described in [39]. The full integrated subtraction terms, for FKS, are given in chapter three, and for FKS pairs associated with entirely final state partons there is little to add to the discussion given there. In this implementation the treatment of the initial state collinear terms is slightly different to the expressions given in

the chapter three. The reorganisation of these terms is for reasons of computational efficiency, by allowing for fewer recalculations of the matrix elements; this is discussed in full in the following subsection. The calculation of the integrated terms takes place, in the AMEGIC++ implementation, within the file `Single_Virtual_CorrectionFKS`, including both the simple final state terms and the initial state terms described below. This file also calls the results of the virtual piece of the calculation and also contains the option to check the pole cancellation between integrated and virtual terms.

### 4.2.1 Initial state terms

The expression for the integrated subtraction terms, given in 4.10 and discussed in chapter three, is considered separately from final state collinear subtraction terms because it has been combined with the PDF counter term.

$$\begin{aligned}
d\sigma_j^{(C_{in}+cnt)} &= \frac{\alpha_s}{2\pi} \left( \frac{(4\pi)^{-\epsilon}}{\Gamma(1-\epsilon)} \left( \frac{\mu^2}{Q^2} \right)^\epsilon \frac{1}{\epsilon} - \log \frac{\mu_f^2}{Q^2} \right) \\
&\quad \times [\gamma(a_1) + 2C(a_j) \log \xi_{cut}] d\sigma^{(B)}(r_{n[i]}) \\
&\quad + \frac{\alpha_s}{2\pi} \sum_{a_{ij}} \left\{ \xi_i P_{a_{ij}a_j}^{(0)}(1-\xi_i) \left[ \left( \frac{1}{\xi_i} \right)_c \log \frac{sY_{cut}}{2\mu^2} + 2 \left( \frac{\log \xi_i}{\xi_i} \right) \right] \right. \\
&\quad \left. - \xi_i P_{a_{ij}a_j}^{(1)}(1-\xi_i) \left( \frac{1}{\xi_i} \right)_c \right\} d\sigma^{(B)}(r_{n[i]}^{a_{ij}}, (1-\xi_i)k_j) d\xi_i \quad (4.10)
\end{aligned}$$

The form of the initial state term, as shown in 4.10, is of a splitting function convoluted with a matrix element squared; where the partonic flavour of the initial state FKS parton is summed over. It is noted that for the calculation of the full hadronic cross section, all possible partonic cross sections which contribute to the hadronic process must be included; the full hadronic cross section calculation is therefore written in terms of a sum over all initial state partons. Combining this sum with the initial state integrated terms yields a term of the form given in 4.11, for the form of



implemenatation of FKS.

$$\begin{aligned}
& \sum_{a_1, a_2} \int d\eta_1 d\eta_2 f_a(\eta_1) f_b(\eta_2) \int_m d\sigma^B(\{a_l\}, \eta_1 p_1, \eta_2 p_2) \left\{ C\left(\frac{1}{\epsilon}\right) + h \right. \\
& + \sum_{a'_1} \int_0^{1-\eta_1} d\xi_i \left[ \frac{f_{a'_1}(\eta_1/(1-\xi_i))}{(1-\xi_i)f_{a_1}(\eta_1)} g_{a_1 a'_1}(x) - \frac{f_{a'_1}(\eta_1)}{f_{a_1}(\eta_1)} \Theta(\xi_i - \xi_{\text{cut}}) g_{a_1 a'_1}(x) \right] \\
& + \sum_{a'_1} \frac{f_{a'_1}(\eta_1)}{f_{a_1}(\eta_1)} \left[ K_{a_2 a'_2}(1) + \int_{1-\eta_1}^1 d\xi_i \Theta(\xi_i - \xi_{\text{cut}}) g_{a_1 a'_1}(x) \right] \\
& + \sum_{a'_2} \int_0^{1-\eta_2} d\xi_i \left[ \frac{f_{a'_2}(\eta_2/(1-\xi_i))}{(1-\xi_i)f_{a_2}(\eta_2)} g_{a_2 a'_2}(x) - \frac{f_{a'_2}(\eta_2)}{f_{a_2}(\eta_2)} \Theta(\xi_i - \xi_{\text{cut}}) g_{a_2 a'_2}(x) \right] \\
& \left. + \sum_{a'_2} \frac{f_{a'_2}(\eta_2)}{f_{a_2}(\eta_2)} \left[ K_{a_2 a'_2}(1) + \int_{1-\eta_2}^1 d\xi_i \Theta(\xi_i - \xi_{\text{cut}}) g_{a_2 a'_2}(x) \right] \right\} \quad (4.12)
\end{aligned}$$

In the implementation the integral over  $\xi_i$ , as expressed in 4.12, is computed numerically in `Single_Virtual_CorrectionFKS`; for each call of the integrated terms for the phase space integration the file calls a new value of  $\xi_i$ , thus the  $\xi_i$  integral is performed with the phase space integration.

## 4.3 Real Subtraction Terms

### 4.3.1 Organisation of the Calculation

The real subtraction term is, by definition, the finite contribution that is yielded by addition of subtraction terms to the real cross section, schematically it has the form of 4.13

$$d\sigma^{(RS)} = d\sigma^{(R)} - \sum d\sigma^{(\text{sub})} \quad (4.13)$$

It is, as can be seen, constructed from two objects. The first is a tree level matrix element squared, with an additional partonic added to the Born level process; in terms of implementation this can be obtained fairly easily when working in an automatic matrix element generator such as `AMEGIC++`. The second are the full set of subtraction terms, which in FKS are constructed by splitting the real phase

space into regions defined by FKS pairs; in each region the subtraction terms are represented implicitly by plus distributions of energy and angular variables of the FKS pairs. The explicit form of the subtraction terms can be calculated by taking the singular limits of these variables on the real term; this, as has been discussed in chapter three, is the result of the factorisation of the real matrix element in such limits. In the implementation the real subtraction term is constructed from a file, `Single_Real_CorrectionFKS`, which calls the real matrix element squared from the matrix element generator. The subtraction is then organised thus; the real process file iterates over all valid pairs of partons from the real process and assigns these to become FKS pairs. For each FKS pair, the collinear subtraction subtraction term is then calculated in the file `Single_CollTermFKS`; this subtraction file also contains the required functions to perform the required kinematic map from the real to Born phase space or  $\{k\}_{n+1} \rightarrow \{\hat{k}\}_n$ . The soft terms are subtracted separately, but the structure of the computation is similar to the collinear part. The iteration over possible FKS pairs in the collinear terms is then replaced with a similar iteration over final state gluons, the functional form of the soft subtraction term is then calculated in `Single_SoftTermFKS`. This again calculates the appropriate kinematic maps although the soft maps are in general different to the collinear ones. The soft-collinear subtraction terms then are calculated within the soft term, though in principle they can be included with the collinear terms. It should be noted that the subtraction terms, as calculated in both subtraction files, utilize Born level terms calculated within the `AMEGIC++` matrix element generator; these are then accessed within these files to form the subtraction terms.

### 4.3.2 Kinematics

The full NLO cross section requires the integration of all terms that make up the NLO calculation over their respective phase spaces. The real subtraction term, in which both the real and subtraction terms are defined on an  $n+1$  particle phase space, must then be integrated over this  $n+1$  particle phase space. In the implementation this integral is carried out with the Monte Carlo integration routine native to SHERPA,

details of which are beyond the scope of this thesis, but which can be found in [37]. However, the construction of the subtraction terms via plus distributions creates complications for the momenta of the subtraction terms. Consider the example of subtracting a soft term.

$$\int d\phi_{n+1} \frac{1}{\xi_i} f(k_1, \dots, k_{n+1}) - \int d\xi_i dy_{ij} d\Omega \frac{1}{\xi_i} \left[ d\phi_{[i]} f(\xi_i = 0, \{\hat{k}\}_{[i]}) \right]_{\xi_i=0} \quad (4.14)$$

Where  $\{\hat{k}\}$  is defined as the set of  $n$  momenta which result from the soft limit of  $k_i$ . It is clear, from momentum conservation, that this new set of momenta are not equal to the momenta from the real term, but must somehow correspond to a soft and/or collinear limit of that set of momenta. It is noted that in such limits the phase space factorises into a Born like phase space and a one particle phase for the an unresolved parton; it is necessary, for the calculation of the real subtraction terms, to be able to construct such a phase space from the real phase space. To accomplish this, kinematic maps are constructed which map a set of  $n+1$  momenta to a set of  $n$  momenta i.e.  $\{k\}_{n+1} \rightarrow \{\hat{k}\}_n$ , which are equivalent to these limits. The construction of such maps can be non trivial, as the result of constraints on the phase space; such as the requirement that the momenta must remain on their mass shells. The notation used from now on in this section will clearly show unmapped momenta as  $k$  and mapped momenta as  $\hat{k}$ .

The mapping of momenta, for use in subtraction terms, in this fashion does not ensure that the correct phase space integral is applied to the subtraction terms. The Monte Carlo integration of these terms is carried out over the unmapped phase space, however given the nature of the plus distributions it is the mapped phase space which must be integrated over. To correct this, without substantial modification of the Monte Carlo intergration native to SHERPA , Jacobians are constructed from the relevant relations between the mapped and unmapped monenta. Including these Jacobians in the subtraction terms then ensures that integration over the unmapped phase space, becomes equivalent to conducting the integral over the mapped phase space, as is required by the plus distributions. In the notation of 4.14, this is is represented by 4.15.

$$d\hat{\phi}_n d\xi_i dy_{ij} d\Omega_i = J d\phi_{n+1} \quad (4.15)$$

For other subtraction schemes, such as Catani-Seymour, these kinematic maps are specified for particular subtraction terms; however this is not the case for FKS. In the original FKS papers [10] and [34] no kinematic maps are given, as no unique map exists; rather any map which gives the correct infrared limits (the soft or collinear limits) can in principle be used. The maps presented in the following section are those chosen for this implementation and it is stressed that other choices are possible. The momentum maps for subtraction terms used in this implementation will in general be different for both the two kinematic limits and to whether the remapping is applied to initial or final state partons; that the mapping for the soft and collinear limits, should in general be different, is fairly intuitive given the difference in the kinematics, however the dependence on initial and final states is not. This dependence is the result of constraints placed on the mapping of initial state partonic momenta, where the use of PDFs restricts any mapping of partonic momenta to a rescaling. All maps used have been tested for the correct soft or collinear limits to ensure their validity.

### 4.3.3 Final State Collinear Map

This section will detail the momentum map used for collinear subtraction terms, where the FKS partons for this term are both in the final state. The map is constructed by considering the collinear limit of  $k_i, k_j$  but it is also valid in the  $k_i$  soft limit, it is outlined in detail in [40]. To begin, the following definitions are made:

$$q = p_1 + p_2 \quad k = k_i + k_j \quad (4.16)$$

$$k_{\text{rec}} = \sum_{n \neq i, j} k_n \quad M_{\text{rec}}^2 = k_{\text{rec}}^2 \quad (4.17)$$

$$k_{\text{rec}} = q - k \quad \vec{k}_{\text{rec}} = -\vec{k} \quad (4.18)$$

where  $p_{1,2}$  are the initial state partonic momenta (for hadronic initials) or simply the initial state momenta (for e.g. electrons). To map the momenta, all final state partons, except  $k_i$  and  $k_j$  are boosted, and a new combined momentum  $k_{ij}$  is defined as

$$\hat{k}_{ij} = q - \mathcal{B}k_{\text{rec}} \quad (4.19)$$

where  $\mathcal{B}$  is this boost; this is defined to act in the direction  $\vec{k}_{\text{rec}}$ . This definition for  $k_{ij}$  now ensures conservation of momentum. The combined momenta  $k_{ij}$  is required to remain massless; combining this requirement with 4.19 allows the boost velocity to be computed as shown in 4.20.

$$\beta = \frac{q^2 - (k_{\text{rec}}^0 + |\vec{k}_{\text{rec}}|)^2}{q^2 + (k_{\text{rec}}^0 + |\vec{k}_{\text{rec}}|)^2} \quad (4.20)$$

The set of mapped momenta, excluding  $\hat{k}_{ij}$ , are now defined as by acting this boost upon the unmapped momenta, as expressed by 4.21.

$$\hat{k}_l = \mathcal{B}k_l, \quad l \neq i, j \quad (4.21)$$

The mapping of  $\hat{k}_{ij}$  is then defined by 4.19. This map can then be applied to  $n + 1$  momenta from the real term to construct appropriate momenta for the subtraction terms.

When the Monte Carlo integration of the subtraction term occurs in SHERPA, this will be conducted over the unmapped phase space; this is problematic as the plus distributions, upon which the subtraction scheme is built, require the phase space integral of the subtraction terms to be performed over the mapped space. To ensure the correct integration, the Jacobian defined by the transformation of the real to mapped phase space can be utilized; such a Jacobian must, by definition obey 4.15. For this phase space mapping the Jacobian is computed in [40], and is expressed in 4.22.

$$J = \frac{\hat{E}_{ij}}{E_j^2} \left( k_j^0 - \frac{2k_i \cdot k_j}{\sqrt{s}} \right) \quad (4.22)$$

The procedure of initiating a phase space integral over  $d\phi_{n+1}$  and then mapping this to an  $n$  momenta phase space for subtraction terms is a choice that has been made in the implementation. It is instead perfectly possible to generate an  $n$  momenta phase space  $d\hat{\phi}_n$ , with independent variables  $\xi_i, y_{ij}$  and  $\omega$  which give the one particle phase space over  $k_i$ , and perform an inverse map to real phase space,  $\{k\}_{n+1}$ . This is in fact done in some implementations of FKS subtraction, notably MADFKS, but the structure of how phase space integrals are handled in SHERPA means that in

practice it is simpler to make the choice outlined above.

The use of plus distributions to construct the subtraction terms, leads to the requirement that, for the collinear subtraction terms, the mapped momenta should be equivalent to the unmapped momenta in the collinear limit. Such a constraint presents a useful test, both of the map and its implementation.

In the language of this momentum map, this requirement corresponds to the boost specified by 4.20 tending to the identity. For a Lorentz boost specified by a boost factor,  $\beta$ , this requirement must correspond to the boost factor tending to zero in the collinear limit as expressed in 4.23; taking such a limit trivially reduces such a Lorentz boost to the identity. For a Lorentz boost specified by a factor  $\beta$ , this requirement is simply that the boost factor expressed in 4.23.

$$\lim_{k_i || k_j} \beta = 0 \quad (4.23)$$

The condition 4.23 is however not apparent from the form of 4.20, and will now be considered to show the validity of this phase space mapping. The condition 4.23 can be shown by considering the form of  $k_{\text{rec}}$  in the collinear limit, which in the partonic centre of mass frame can be expressed by 4.24-4.25.

$$k_{\text{rec}}^0 = q^0 - E_i - E_j \quad (4.24)$$

$$|\vec{k}_{\text{rec}}| = E_i + E_j \quad (4.25)$$

Utilizing the results of 4.24 and 4.25, for the collinear limits of  $k_{\text{rec}}$  the result 4.26 is apparent.

$$\lim_{k_i || k_j} (k_{\text{rec}}^0 + |\vec{k}_{\text{rec}}|)^2 = q^2 \quad (4.26)$$

The limit expressed in 4.26, combined with the expression for the boost factor in 4.20, leads simply to 4.23. Hence the collinear limit of this map reduces to the identity in the collinear limit, as required.

#### 4.3.4 Initial State Soft map

The soft subtraction term, when calculated independently from the collinear term should have no dependence on other partons in the process; however despite the fact

that soft contributions are indeed calculated in this way, there is a distinction to be made between initial and final state kinematic terms from soft maps. This distinction is a result of considering states that (at Born level) are entirely leptonic, in either the initial or final states; in this case what is phrased as an initial state soft map is used only for processes with solely partonic initial states and leptonic final states. In the case of partonic initial and leptonic final state particles, any unresolved partonic emission must occur off the initial state partons; as a result it is the kinematics of the initial state partons that must be subject to the kinematic map (and vice-versa with leptonic initial and partonic final states).

The momentum map for the soft initial state terms will now be outlined, again it is described in detail in [40]. As with the final state collinear map, it is convenient to begin with some definitions; for this map the quantity  $K_{\text{tot}}$  is defined in 4.27.

$$K_{\text{tot}} = \sum_{n,[i]} k_n = x_1 P_1 + x_2 P_2 - k_i \quad (4.27)$$

To map the final states, excluding  $k_i$ , the boosts,  $\mathcal{B}_L$  constructed such that  $K_{\text{tot}}$  has a zero longitudinal component and  $\mathcal{B}_T$  constructed such that  $K_{\text{tot}}$  has a zero transverse component, are used to boost the final state excluding  $k_i$

$$\hat{k}_l = \mathcal{B}_L^{-1} \mathcal{B}_T \mathcal{B}_L k_l \quad (4.28)$$

The boost now leaves 4.27 to be of the form

$$\hat{K}_{\text{tot}} = \sum_{[i]} \hat{k}_n = \hat{x}_1 P_1 + \hat{x}_2 P_2 \quad (4.29)$$

Where the factors  $\hat{x}_{1,2}$  are rescaled partonic fractions. The rescaling factors can be determined, by noting that the boosts in 4.28 preserve the invariant mass and rapidity between  $K$  and  $\hat{K}$ . Considering the centre of mass frame for  $K$ , this amounts to the conditions 4.30 for rapidity and 4.31 for the invariant mass.

$$\frac{1}{2} \log \frac{2 - \xi_i(1 - y_{i1})}{2 - \xi_i(1 + y_{i1})} = \frac{1}{2} \log \frac{\hat{x}_1}{\hat{x}_2} \quad (4.30)$$

$$s - \xi_i s = \frac{\hat{x}_1 \hat{x}_2}{x_1 x_2} s \quad (4.31)$$

The rescaling factors can then be computed, by a simple manipulation from 4.30 and 4.31, to be:

$$\hat{x}_1 = x_1 \sqrt{1 - \xi_i} \sqrt{\frac{2 - \xi_i(1 - y_{i1})}{2 - \xi_i(1 + y_{i1})}}, \quad \hat{x}_2 = x_2 \sqrt{1 - \xi_i} \sqrt{\frac{2 - \xi_i(1 + y_{i2})}{2 - \xi_i(1 - y_{i2})}} \quad (4.32)$$

where as FKS variables are constructed in the centre of mass frame, such that  $y_{i1} = -y_{i2}$ . A key point to note is that the partonic momenta that are being mapped are fractions of hadronic momenta; as this is a measurable quantity it cannot be mapped. However, the partonic fraction,  $x$  which gives the partonic momenta, can be mapped. So the partonic momenta are mapped what is really happening is a rescaling of  $x$  (so initial state momenta cannot be boosted in a generic direction, as this would change the direction of the hadronic momenta). So the mapping of partonic momenta, in this case, takes the form of a rescaling of the partonic fractions, So for soft and soft-collinear terms the fraction  $x$  in the PDFs must be mapped.

The use of the SHERPA Monte Carlo integration routine for the subtraction term, which will perform the integral over the unmapped phase space as discussed previously, requires the definition of a Jacobian to perform the integral over the mapped phase space. For the case of this map, the Jacobian is simply results from the partonic rescalings, and is given by 4.33; the affect of the Lorentz boosts does not change the integration measure.

$$J = \frac{x_1 x_2}{\hat{x}_1 \hat{x}_2} = \frac{1}{1 - \xi_i} \quad (4.33)$$

While this factor has been labelled a Jacobian, and in effect performs the same role, this factor is actually the result of a rescaling of the variable  $s = 2x_1 x_2 P_1 \cdot P_2$  to  $\hat{s} = 2\hat{x}_1 \hat{x}_2 P_1 \cdot P_2$  and not from any mapping of integrated variables.

The construction of subtraction terms, from plus distributions, leads to requirements on the momentum maps used for the subtraction terms; for the soft maps the application of the momentum map must be equivalent to the soft limit of the unmapped momenta. It is apparent, from their functional form, that in the soft limit the mapped partonic energy fractions become equal to the unmapped ones, i.e.

$$\lim_{\xi_{1,2} \rightarrow 0} \hat{x}_{1,2} = x_{1,2} \quad (4.34)$$

which clearly fulfils the requirement on the map. The boosts acting on the final state momenta must therefore tend to the identity in the soft limit, to complete the requirements on the map.

It is clear that in the soft limit  $K_{\text{tot}} = \sum_{n,[i]} k_n = x_1 P_1 + x_2 P_2$ ; and consequently the boosts constructed with respect to this parameter can be constrained. It is noted that in the partonic centre of mass frame (in which calculations are conducted)  $K_{\text{tot}}$  will already possess zero longitudinal and transverse momentum; the construction of the boosts to ensure these results will then lead to the identity.

### 4.3.5 Final State soft map

For reasons outlined in the previous subsection, the soft term requires separate maps for initial and final partonic states, the final state map is outlined here. The overview of this map is as follows; simply remove the soft parton  $k_i$ , and construct a Lorentz transform on remaining momenta such that they will be boosted into their combined rest frame. The boosted momenta are then rescaled to ensure energy conservation. This map is outlined in [41], and contains the implicit assumption that the input partonic momenta are in the centre of mass frame.

As for the previous maps it will be convenient to begin with some definitions; first of all the Lorentz boost 4.35 is defined, in addition to the parameters  $Q$  and  $\lambda$  in 4.36 and 4.37.

$$\Lambda^\mu{}_\nu(K, \tilde{K}) = g^\mu{}_\nu - 2 \frac{(K + \tilde{K})^\mu (K + \tilde{K})_\nu}{(K + \tilde{K})^2} + 2 \frac{\tilde{K}^\mu K_\nu}{K^2} \quad (4.35)$$

$$Q = p_1 + p_2 \quad (4.36)$$

$$\lambda = \sqrt{1 - \frac{2p_i \cdot Q}{Q \cdot Q}} \quad (4.37)$$

The Lorentz transform, as expressed by 4.35, is simply a generic transform to map one momenta,  $\tilde{K}$  onto another  $K$ , and can be used to in this map to boost the final state partonic momenta, without  $k_i$  the soft parton, to their combined rest frame. The mapped momenta, for all final state partonic momenta  $[k_i]$ , are defined to accomplish

this according to 4.38.

$$\hat{k}^\mu = \frac{1}{\lambda} \Lambda(Q, (Q - k_i)/\lambda)^\mu_\nu k^\nu \quad (4.38)$$

The boost 4.38 is, broadly speaking, transforming the set of final state momenta excluding  $k_i$  into their combined centre of mass frame; while the  $\frac{1}{\lambda}$  term performs a rescaling that ensures conservation of momentum with the initial states.

The use of the SHERPA monte carlo integration routine for the subtraction term, which will perform the integral over the unmapped phase space as discussed previously, requires the definition of a Jacobian to perform the integral over the mapped phase space. For this map, the Jacobian is largely a result of the scale factors present in the transformation 4.38, and is given in 4.39.

$$J = \frac{1}{\lambda^{2(n-1)-2}} \quad (4.39)$$

This factor can simply be derived by considering a rescaling of the momenta by  $1/\lambda$  (i.e.  $k \rightarrow \frac{1}{\lambda}k$ ). The change of the integral measure under such a rescaling is given in 4.40.

$$\prod_m^n \frac{dk_m^3}{2k_m^0 (2\pi)^3} \delta^4(p_1 + p_1 - \sum_{n=1}^n k_n) = \prod_{\hat{k}}^n \frac{1}{\lambda^2} \frac{d\hat{k}_m^3}{2\hat{k}_m^0 (2\pi)^3} \lambda^4 \delta^4(p_1 + p_1 - \sum_{n=1}^n \hat{k}_n) \quad (4.40)$$

Accumulating the factors of  $\lambda$  clearly yields 4.39.

While the above is sufficient to define the map, it is important to consider its validity; one key requirement on such a map is the mapped phase space's equivalence to the real phase space in the (soft) kinematic limit. The condition on the Lorentz boost, expressed in 4.38, caused by this requirement amounts to the transform becoming the identity, in the kinematic limit. The functional form of the variables and boost can be used to show this algebraically. The application of the soft limit to 4.37 is relatively straightforward and leads to the result

$$\lim_{k_i \rightarrow 0} \lambda = 1 \quad (4.41)$$

this limit also gives the functional form of the boost to be  $\Lambda(Q, Q)$ . After some unremarkable algebra the boost becomes

$$\Lambda(Q, Q)^\mu_\nu = g^\mu_\nu \quad (4.42)$$

which is simply the identity. This map therefore must produce mapped momenta that are equivalent to unmapped momenta in the soft limit.

### 4.3.6 Initial state Collinear map

This subsection will now detail the momentum map used for collinear subtraction terms with FKS pairs which include an initial state parton. As has been discussed the presence of initial state partons restricts the mapping of these partons to a rescaling. The overview of this map is that  $k_j$  is mapped to some fraction,  $z$  of itself (which corresponds to the fraction  $z$  in the splitting functions), the final state momenta are then Lorentz boosted to ensure conservation of momentum. As for the previous maps, it is convenient to begin with some definitions; the fraction,  $z$ , used for the partonic rescaling, is defined to be

$$z = \left(1 - \frac{k_i \cdot Q}{k_1 \cdot k_2}\right) \quad (4.43)$$

where this value is also the partonic fraction of the collinear splitting. Additionally the Lorentz boost 4.44 is defined.

$$\Lambda^\mu{}_\nu(K, \tilde{K}) = g^\mu{}_\nu - 2 \frac{(K + \tilde{K})^\mu (K + \tilde{K})_\nu}{(K + \tilde{K})^2} + 2 \frac{\tilde{K}^\mu K_\nu}{K^2} \quad (4.44)$$

The boost 4.44 is also found in the final state soft map, and is used for the same purpose here, to boost all final state momenta, excluding  $k_i$ , to their collective rest frame. In this mapping, the  $z$  fraction is then used to rescale the initial state FKS parton,  $j$  in the manner of 4.45.

$$\hat{k}_j = \left(1 - \frac{k_i \cdot Q}{k_1 \cdot k_2}\right) k_j \quad (4.45)$$

The mapped final state momenta are then constructed by applying a Lorentz boost on all the existing momenta, excluded  $k_i$ , according to 4.46

$$\hat{k}_n = \Lambda^\mu{}_\nu(\hat{k}_1 + \hat{k}_2, Q - k_i) k_n^\nu \quad (4.46)$$

Where  $\hat{k}$  represents the mapped momenta,  $k_n$  represents all final state momenta,  $Q = k_1 + k_2$ , and the Lorentz transform is given in 4.44. This boost, as for the

equivalent boost in the final state map, simply transforms the final state momenta, excluding  $k_i$ , to their collective rest frame. This map is detailed in [32], and is in fact the same map used for Initial-Initial dipole functions in Catani Seymour subtraction. For Collinear mapping the rescaling of PDFs, as required for soft terms, does not occur. The reason is that in the soft limit, the momenta  $k_i$  must be treated as if it's zero, hence the total partonic energy of the process will change, requiring remapped PDF's. For collinear terms, the momenta  $k_i$  does not tend to zero, it simply becomes collinear to  $k_j$ ; hence the total momenta in the initial state is unchanged, meaning that the partonic energy fractions,  $x$  are unchanged by this map.

For other phase mappings presented in this work, the Jacobian associated with modifying the integration measure of unmapped phase space, to that of the mapped one is discussed. In the case of this map, the only actions on the momenta are a rescaling of one initial state parton, and a Lorentz boost on all final state partons. For reasons that are discussed above, namely that the rescaling doesn't change the partonic fractions, there is no factor analogous to 4.33 for this map; additionally the affect of Lorentz boosting, as has been discussed for other maps, does not change the integration measure. Hence for the case of this mapping, there is not a Jacobian factor.

The plus distribution for the collinear variable requires that the map is essentially the equivalent of taking the collinear limit of the original momenta; hence this leads to the requirement that the mapped momenta are equivalent to the unmapped momenta in the collinear limit. This requirement is manifested in the momentum map, by the constraint that the Lorentz boost expressed in 4.46 must tend to the identity in the collinear limit. To show this, it is appropriate to start with the collinear limit of  $\hat{k}_j$ , which is apparent from 4.46 as  $\hat{k}_j = k_j - k_i$ . The functional form of the boost  $\Lambda^\mu_\nu(\hat{k}_1 + \hat{k}_2, Q - k_i)$  must then, after some unremarkable algebra become

$$\Lambda(Q - k_i, Q - k_i)^\mu_\nu = g^\mu_\nu \quad (4.47)$$

which is simply the identity. This map therefore must produce mapped momenta that are equivalent to unmapped momenta in the collinear limit.

## 4.4 Technical Cutoff

The implementation of a subtraction scheme such as FKS must deal with the singularities present in the integration of the real term. In theory this is completely dealt with by the subtraction term. However for numerical calculations, the presence of infinite, or very large, numbers in the calculation can be problematic; this mostly occurs in the form of large fluctuations in the numerical calculation, and can therefore be the cause of large errors. There are two issues that cause these problems for numerical calculations; the first is the limited precision of numerical values available computationally. The second is the result of the unresolved limits of QCD matrix elements, these have been discussed in previous chapters and form the basis for the construction of the FKS subtraction term. However in these discussions, only the leading term in this limit is considered; this is appropriate when considering singularities however, it is noted that for both the soft and collinear limits, of the matrix element squared, subleading terms exist; these terms are of order  $\mathcal{O}(\frac{1}{\xi_i})$  for the soft and  $\mathcal{O}(\frac{1}{(1-y_{ij})^{1/2}})$  for the collinear limit. The presence of such terms causes no contribution to the singularity structure, hence their absence from prior discussion. However it is clear that such terms will appear divergent in the soft or collinear limit, despite being finite over the full phase space integral; and it these terms in the soft and collinear regions that can cause large fluctuations and errors. To deal with these issues, a numerical cutoff is placed upon the calculation, for the FKS variables  $\xi_i$  and  $1 - y_{ij}$ . As is clear from discussion of the FKS method, singularities from the real term correspond to the  $\frac{1}{\xi_i}$  and  $\frac{1}{1-y_{ij}}$  becoming large in the soft or collinear limits; to implement a cutoff of this form a lower limit,  $\alpha_{\min}$  can simply be placed on  $\xi_i$  and  $1 - y_{ij}$ . This approach rests upon the assumption that as the phase space cut is made finer, the approximation to the analytic answer becomes better; consequently, as cut is adjusted to become finer, the result of the calculation should converge to the same value. This is considered in the next section, for this implementation, and the results are commented upon.

## 4.5 Tests of the Implementation

In the following section a series of tests, that have been applied to the implementation, are described and the results of these tests are presented and discussed. These tests are either straightforward checks, such as comparisons with other NLO codes or technical checks such as correct behaviour in the cutoff region.

### 4.5.1 Parameter Variation

One check on an implementation of FKS subtraction is to consider the cutoff parameters  $\xi_{\text{cut}}$  and  $Y_{\text{cut}}$ . These appear as phase space cuts in the subtraction terms from the plus distributions and are explicitly part of the integrated terms. For self consistency the variation of these parameters should not vary the cross section, as they are introduced artificially by the subtraction scheme. Hence a good check on the implementation is to calculate the cross section with varying values of  $\xi_{\text{cut}}$  and  $Y_{\text{cut}}$ . To this effect the variation for both  $\xi_{\text{cut}}$  and  $Y_{\text{cut}}$  (with the other held constant) is plotted in figures 4.1 to 4.6 for  $e^+e^- \rightarrow jj$ ,  $e^+e^- \rightarrow jjj$  and  $jj \rightarrow e^+e^-$ . These results plot the combined Born and integrated terms, the real term and the total cross section against the cutoff parameters. These figures also display the fractional errors of Born and Integrated terms, and the real terms. Additionally the combined values are plotted with the equivalent result from Catani Seymour subtraction. The combined Born and integrated piece and the real term are both calculated to 1% accuracy in SHERPA, the NLO cross section here is simply the sum of these two pieces.

As can be seen from figures 4.1 to 4.6, there is no variation over either of these parameters in any of the specified processes, this is therefore a good indication that FKS subtraction has been successfully implemented.

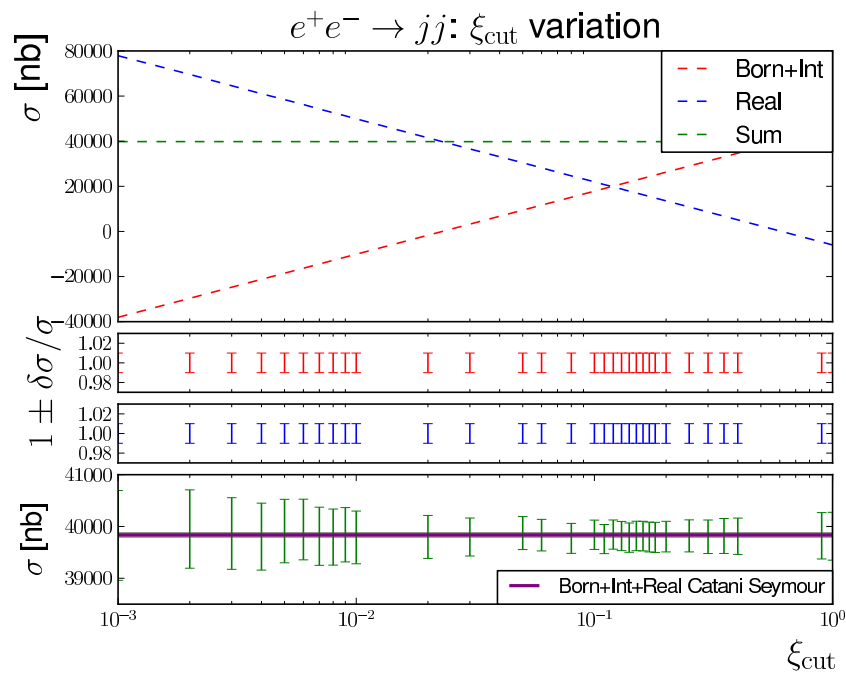


Figure 4.1: The variation of the NLO cross section for  $e^+e^- \rightarrow jj$  as calculated by the FKS implementation with the soft cutoff parameters  $\xi_{\text{cut}}$ . The Integrated and Real terms are plotted separately to display their variation

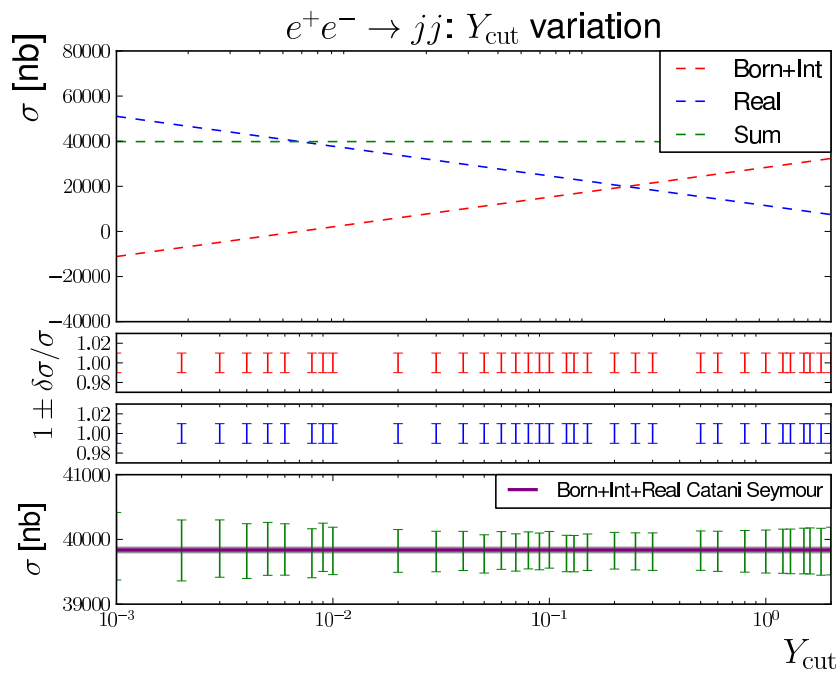


Figure 4.2: The variation of the NLO cross section for  $e^+e^- \rightarrow jj$  as calculated by the FKS implementation with the collinear cutoff parameter  $Y_{\text{cut}}$ . The Integrated and Real terms are plotted separately to display their variation

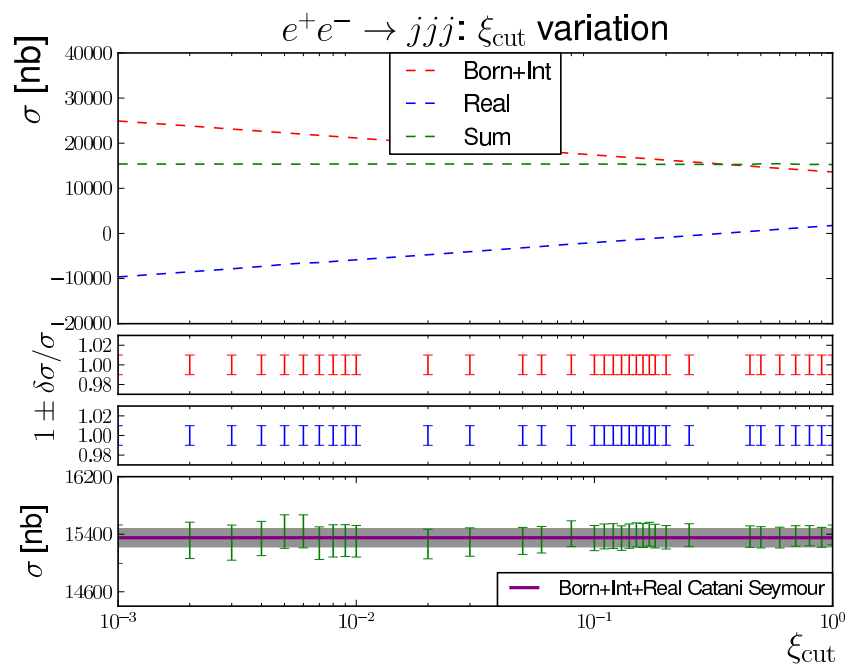


Figure 4.3: The variation of the NLO cross section for  $e^+e^- \rightarrow jjj$  as calculated by the FKS implementation with the soft parameter  $\xi_{\text{cut}}$ . The Integrated and Real terms are plotted separately to display their variation

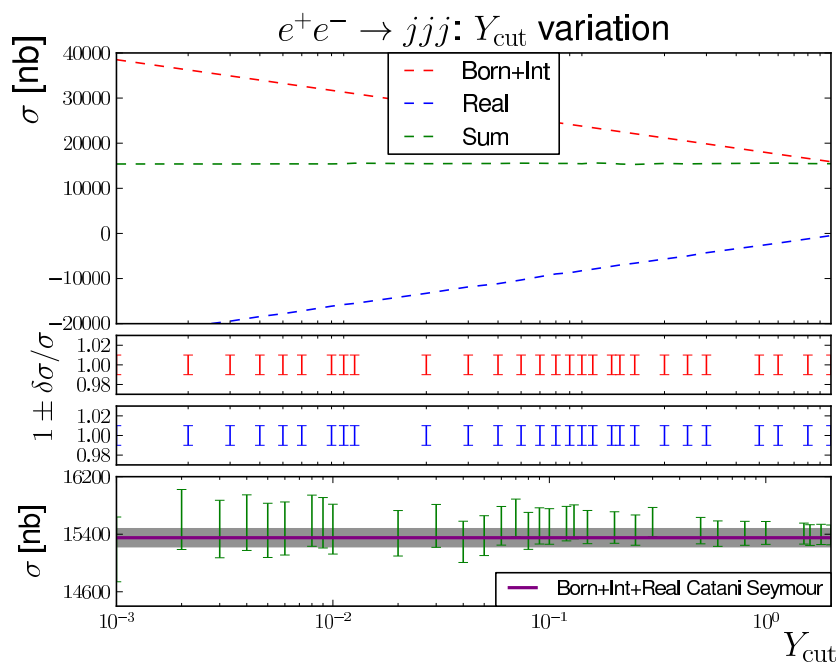


Figure 4.4: The variation of the NLO cross section for  $e^+e^- \rightarrow jjj$  as calculated by the FKS implementation with the collinear cutoff parameter  $Y_{\text{cut}}$ . The Integrated and Real terms are plotted separately to display their variation

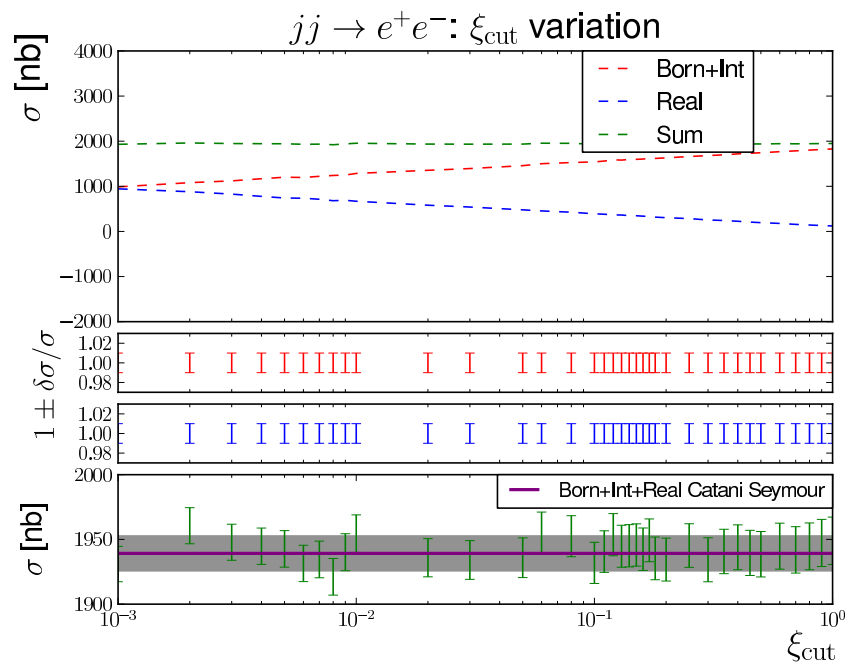


Figure 4.5: The variation of the NLO cross section for  $jj \rightarrow e^+e^-$  as calculated by the FKS implementation with the soft parameter  $\xi_{\text{cut}}$ . The Integrated and Real terms are plotted separately to display their variation

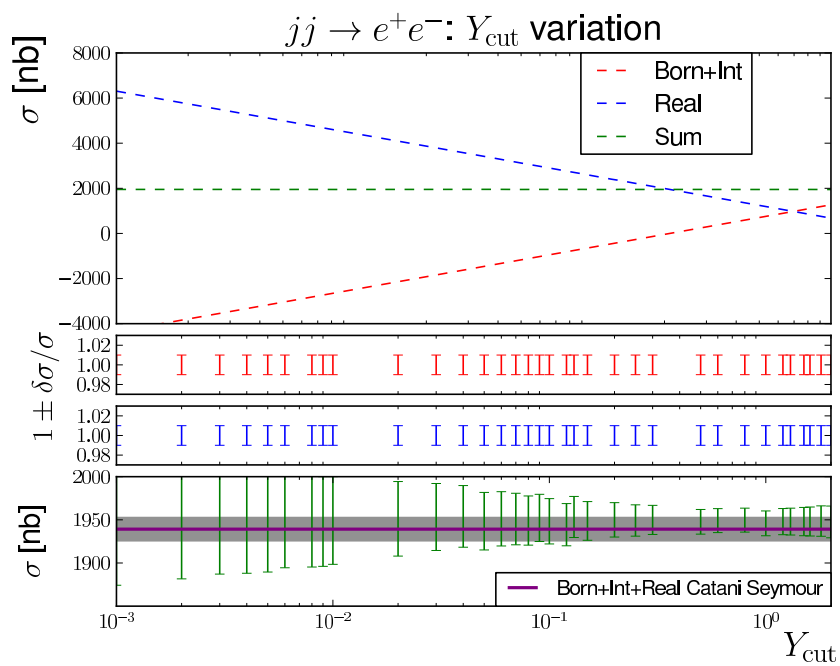


Figure 4.6: The variation of the NLO cross section for  $jj \rightarrow e^+e^-$  as calculated by the FKS implementation with the collinear cutoff parameter  $Y_{\text{cut}}$ . The Integrated and Real terms are plotted separately to display their variation

### 4.5.2 Convergence test for Subtraction Terms

The need for technical cutoffs in the implementation is discussed in the previous section, and is for the twofold reasons of limited numerical precision in computations and the behaviour of subleading terms of the matrix element in the unresolved limits. Consequently a cutoff,  $\alpha_{\min}$ , is required on the values of the FKS variables  $\xi_i$  and  $y_{ij}$ , that prevent the discussed problems; which occur in the regions where  $\frac{1}{\xi_i}$  and  $\frac{1}{y_{ij}}$  become large.

So a useful test of this implementation is to vary  $\alpha_{\min}$  with the real subtracted piece; if the implementation is correct, then as  $\alpha_{\min}$  becomes small  $\sigma^{(RS)}$  should tend to a common value. This test is conducted for the process  $e^+e^- \rightarrow jj$ ,  $jj \rightarrow e^+e^-$ , and the plots shown in figures 4.7 and 4.8 give the variation of  $\sigma^{(RS)}$  with  $\alpha_{\min}$  for these processes. The values of  $\sigma^{(RS)}$  are calculated with FKS cut off parameters  $\xi_{\text{cut}}$ ,  $Y_{\text{cut}}$  set to 1,2 respectively, which allow the subtraction terms to be calculated over the entire phase space. As such the only phase space cuts associated with values of  $\sigma^{(RS)}$  are the result of  $\alpha_{\min}$ .

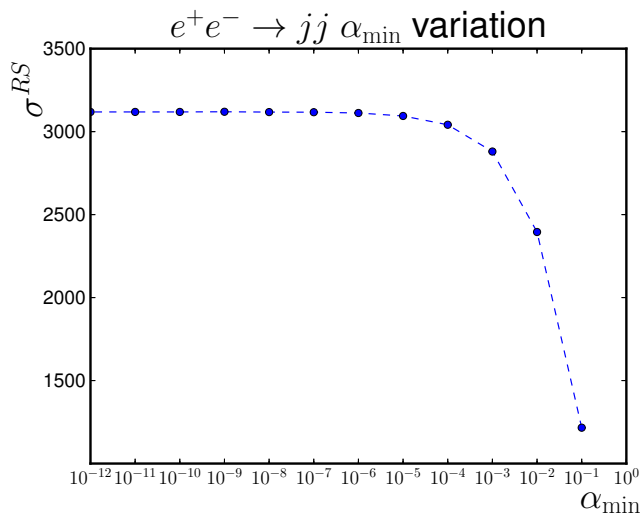


Figure 4.7: The subtracted real term,  $\sigma^{(RS)}$  calculated for the process  $e^+e^- \rightarrow jj$  in FKS for different numerical cutoff values,  $\alpha_{\min}$ , in the integration. FKS cutoff parameters,  $\xi_{\text{cut}}$  and  $Y_{\text{cut}}$  set to 1,2 respectively such that only phase space cuts are the result of  $\alpha_{\min}$ .

As can be seen from the plots given in figures 4.7 and 4.8 there is a convergence of  $\sigma^{(RS)}$  for  $\alpha_{\min} < 10^{-5}$ , which indicates that this cutoff procedure is valid for  $\alpha_{\min}$  below this value.

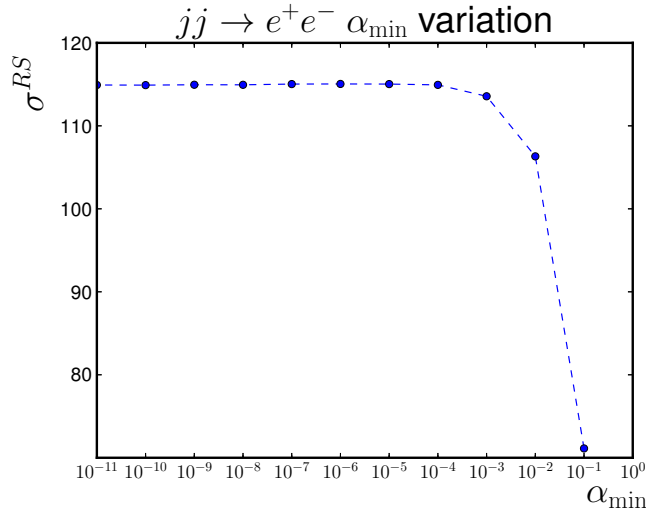


Figure 4.8: The subtracted real term,  $\sigma^{(RS)}$  calculated for the process  $jj \rightarrow e^+e^-$  in FKS for different numerical cutoff values,  $\alpha_{\min}$ , in the integration. FKS cutoff parameters,  $\xi_{\text{cut}}$  and  $Y_{\text{cut}}$  set to 1,2 respectively such that only phase space cuts are the result of  $\alpha_{\min}$ .

### 4.5.3 Comparison with Catani Seymour Cross Sections

One of the most obvious comparisons for an implementation of NLO calculations is to cross check the results against the same calculation implemented with a different method. For the implementation of FKS subtraction within AMEGIC++ the obvious check on the calculation is the comparison against the existing Catani Seymour implementation in the same generator, which is described in [39]. The following table gives a list of processes for which both FKS and Catani-Seymour subtraction is used to calculate the real component of the NLO cross sections.

All energies, cuts, PDFs and jet selectors used are identical for both methods (the set up for running simply differs by a switch which distinguishes FKS from CS), and the details are not discussed as the aim here is to demonstrate consistency with another

method rather than provide comprehensive predictions. Given the cross sections that

Process	$\sigma_{NLO}^{BR}$ CS [pb]	$\sigma_{NLO}^{BR}$ FKS [pb]
$e^+e^- \rightarrow jj$	$42530 \pm 10$	$42520 \pm 9$
$e^+e^- \rightarrow jjj$	$16190 \pm 80$	$16260 \pm 80$
$e^+e^- \rightarrow jjjj$	$2530 \pm 60$	$2550 \pm 40$
$jj \rightarrow h_o \rightarrow \tau^+\tau^-$	$1.68 \pm 0.002$	$1.7 \pm 0.02$
$jj \rightarrow e^+e^-$	$2047 \pm 2$	$2020 \pm 20$

Table 4.1: The Born and real components of the NLO cross sections calculated with the Catani-Seymour and FKS implementations within AMEGIC++ [6], which in each case has been run with one million events.

are listed above which give an agreement, within error, between the two implementations, it is not unreasonable to conclude that FKS has been correctly implemented within AMEGIC++. It is noted that there is an absence of cross sections for processes which would require kinematic maps applied to both the initial and final states, for example deep inelastic scattering; this is because currently such a kinematic map has not been incorporated within this implementation and does not reflect any difficulties with the subtraction scheme.

# Chapter 5

## Comparison with Catani Seymour

The implementation of FKS subtraction in AMEGIC++, described and tested in the previous chapters, is in part motivated by the desire for the fully automatic calculation of NLO corrections. However, an automatic implementation of a subtraction scheme has already been accomplished in [39] for Catani Seymour dipoles. Indeed so far the dipole subtraction procedure has been the method of choice for calculation of the NLO processes. The implementation of an automatic FKS subtraction in AMEGIC++ therefore requires additional motives. The principle motive for this is fairly simple, to speed up calculations. The usual (though not always) bottleneck for QCD processes at NLO is the real subtracted piece and this is essentially because it requires the calculation of a more complex matrix element integrated over a larger phase space. There is, however, some computational speed to be gained by optimising the subtraction scheme that is used and it is in this vein that FKS has been implemented.

### 5.1 Comparison of the Subtraction Terms

The comparison of the subtraction terms for the FKS and Catani Seymour methods in this chapter is, as has been stated, motivated by attempts to improve the efficiency of NLO calculations with particular reference to the real subtraction term. The purpose of this section is to consider the subtraction terms in each method and attempt to

discuss general statements about the efficiency of each method relative to the other. The subtraction method of Catani and Seymour, reviewed in chapter two, yields a structure of subtraction terms that is described by a sum over universal dipole functions convoluted with a Born level matrix elements squared. The universal dipole functions are constructed from kinematic variables of three partons in the real matrix elements; the complete set of subtraction terms is computed by the sum over all possible configurations of dipole functions, this is schematically represented in the equation below.

$$d\sigma^{\text{sub}} = \sum_{i,j,k} V_{ijk} \otimes d\sigma^B(\{\hat{k}_n\}) \quad (5.1)$$

Where  $V_{ijk}$  are a set of universal functions. The key point to note here is that this is a sum over all three parton configurations possible from the set of  $n + 1$  partons of the real term. FKS subtraction, reviewed thoroughly in chapter three, is based upon constructing subtraction terms from pairs of objects. In the implementation of FKS, described in previous sections, soft subtraction terms are considered separately from these pairs. Schematically the FKS subtraction (in this implementation) can be written as

$$d\sigma^{\text{sub}} = \sum_{i,j \in \mathcal{P}_{\text{FKS}}} f(k_i, k_j) d\sigma(\{\hat{k}\}_n) + \sum_{i \in g} f(k_i) d\sigma(\{\hat{k}\}_n) \quad (5.2)$$

Comparing the subtraction structure of both methods, it can be seen that in both methods subtraction terms are composed of some kinematic function convoluted with a Born level matrix element squared. In the case of Catani Seymour subtraction these kinematic functions are the dipoles and for FKS they are represented by either Altarelli-Parisi splitting functions, in the collinear limit, or eikonal factors for the soft limit. In subtraction terms of this form, the most computationally intensive component is the calculation of the Born level matrix element squared; comparatively the kinematic functions are 'cheap'. Upon this, the assumption is built that individual subtraction terms in either method are not significantly more or less computationally intensive to calculate. It is therefore not unreasonable to reduce the comparison of the computational efficiency to simply considering the number of subtraction terms necessary for each method.

From the structure of the Catani Seymour and FKS subtraction terms given above some crude statements on the number of subtraction terms used from each method can be made. For Catani Seymour the full subtraction term is obtained by a sum over all possible three parton configurations possible from the real process; for FKS, which is constructed from pairs of partons, the full subtraction term is obtained by a sum over all possible pairs. A naive comparison of subtraction terms, for a real process with  $n + 1$  partons, would therefore give the number of subtraction terms for Catani Seymour subtraction to be

$$\frac{(n + 1)!}{3!(n - 2)!} \quad (5.3)$$

And for FKS

$$\frac{(n + 1)!}{2!(n - 1)!} \quad (5.4)$$

These are simply the results from combinatorics from picking all possible sets of three partons (for Catani Seymour) and pairs (FKS). This is a naive comparison, as many of these terms in both of these subtraction procedures are zero (mostly because the corresponding Born term for them doesn't exist), and these values are in reality the upper bound for the number of subtraction terms for a given process. It does however provide a useful guide to the scaling of subtraction terms for large values of  $n$ . This gives a scaling of  $\approx n^3$  for Catani Seymour and  $\approx n^2$  for FKS; given this scaling it is fairly clear that for high multiplicity process there are fewer subtraction terms present in FKS.

An additional component of the implementation of subtraction schemes, which is discussed in previous chapters, is the introduction of kinematic cuts on the subtraction terms. These are present, both in the FKS implementation detailed in chapter four and the Catani Seymour implementation against which it is compared, outlined in [39]. These kinematic cuts are introduced to increase the efficiency of the calculation, by only calling the subtraction terms in regions of phase space where singular terms begin to emerge. This introduces additional parameters into the calculation, the invariance of the result on these parameters is tested in chapter four. The form of

these cuts for Catani Seymour and FKS is shown in the expressions below and is neatly summarised thus: in FKS two parameters exist, one for the soft and one for the collinear subtraction terms, which apply cuts on the relevant variables ( $\xi_i$  or  $y_{ij}$ ). In Catani Seymour a single dipole cutoff parameter applies to all dipole functions which cuts on a dipole dependent kinematic variable (see [39] for details).

$$d\sigma^{\text{sub}} = \sum_{i,j,k} \Theta(\alpha_{\text{dip}} - y_{ijk}) V_{ijk} d\sigma_{nm}(\{\hat{k}_n\}) \quad (5.5)$$

Where  $y_{ijk} = \frac{p_i \cdot p_j}{p_i \cdot p_j + p_i \cdot p_k + p_j \cdot p_k}$

$$d\sigma^{\text{sub}} = \sum_{i,j \in \mathcal{P}_{\text{FKS}}} \Theta(y_{ij} - (1 - Y_{\text{cut}})) f(k_i, k_j) d\sigma(\{\hat{k}\}_n) + \sum_{i \in g} \Theta(\xi_{\text{cut}} - \xi_i) f(k_i) d\sigma(\{\hat{k}\}_n) \quad (5.6)$$

Where  $\xi_i = \frac{2E_i}{\sqrt{s}}$  and  $y_{ij} = 1 - k_i \cdot k_j / E_i E_j$ .

This provides a somewhat more complex picture of the relative number of terms required for Catani Seymour and FKS subtraction; the number of subtraction terms used now has a kinematic dependence and so clear comparisons from combinatorics provided above are not necessarily reliable.

## 5.2 Results

The discussion of the relative efficiency of FKS and Catani Seymour subtraction methods given in the previous section introduced the assumption that, for computational reasons, this analysis could be reduced to a comparison of the numbers of subtraction terms used by each method. A simple crude comparison of terms, given in the previous section showed that for high multiplicity events FKS will produce fewer subtractions (and conversely that for small  $n$  there are fewer Catani Seymour terms), however there are complicating factors to this argument. One of these is that not all combinations of either FKS pairs or Catani Seymour triplets produce valid Born level matrix elements. The other complicating factor is the presence of kinematic cuts on the subtraction terms, which in essence give a phase space dependence to the number of subtraction terms.

A more direct comparison is therefore needed to provide information as to the efficiency of the two subtraction schemes relative to each other. In this vein this section will detail runs of the real subtraction terms calculated from both the Catani Seymour and FKS in AMEGIC++, where the total number of subtraction terms called are measured.

The results of these runs are plotted in figures 5.1 to 5.4, for the processes  $e^+e^- \rightarrow jj$ ,  $jj \rightarrow e^+e^-$ ,  $e^+e^- \rightarrow jjj$  and  $e^+e^- \rightarrow jjjj$ . The number of subtraction terms measured is defined to be the number of calls to these terms necessary to integrate the real-subtracted piece to 0.1% accuracy for  $e^+e^- \rightarrow jj$  and 1% accuracy for the other processes; these results are given for a large range of FKS and Catani Seymour cutoff parameters.

The phase space cuts associated with subtraction terms, discussed in the previous section with more detail in chapter three for FKS and in [39] for Catani Seymour, do not cut the phase space in the same way for both methods; this is simply the result of applying these cuts on different kinematical variables. The phase space cuts on the subtraction terms have an obvious impact on measuring the numbers of subtraction terms used to calculate the real subtracted cross section; as a result when comparing the numbers of subtraction terms used, for the Catani Seymour and FKS methods in a particular process, care must be taken to ensure the cuts on the phase space used in both methods give a similar restriction on the phase space in which subtraction terms are calculated to enable a valid comparison to be made.

To ensure this region is comparable in both, a definition is made to compare the phase space cuts in both methods, in terms of the percentage of subtraction terms called. This can be computed from the number of subtraction terms called, and the number without applying phase space cuts (for any given process the number of subtraction terms for both methods is straightforward to obtain). The range of FKS and Catani Seymour cutoffs in figures 5.1 to 5.4 are broadly equivalent by this measure.

It is worth commenting on some general features of these figures before specific

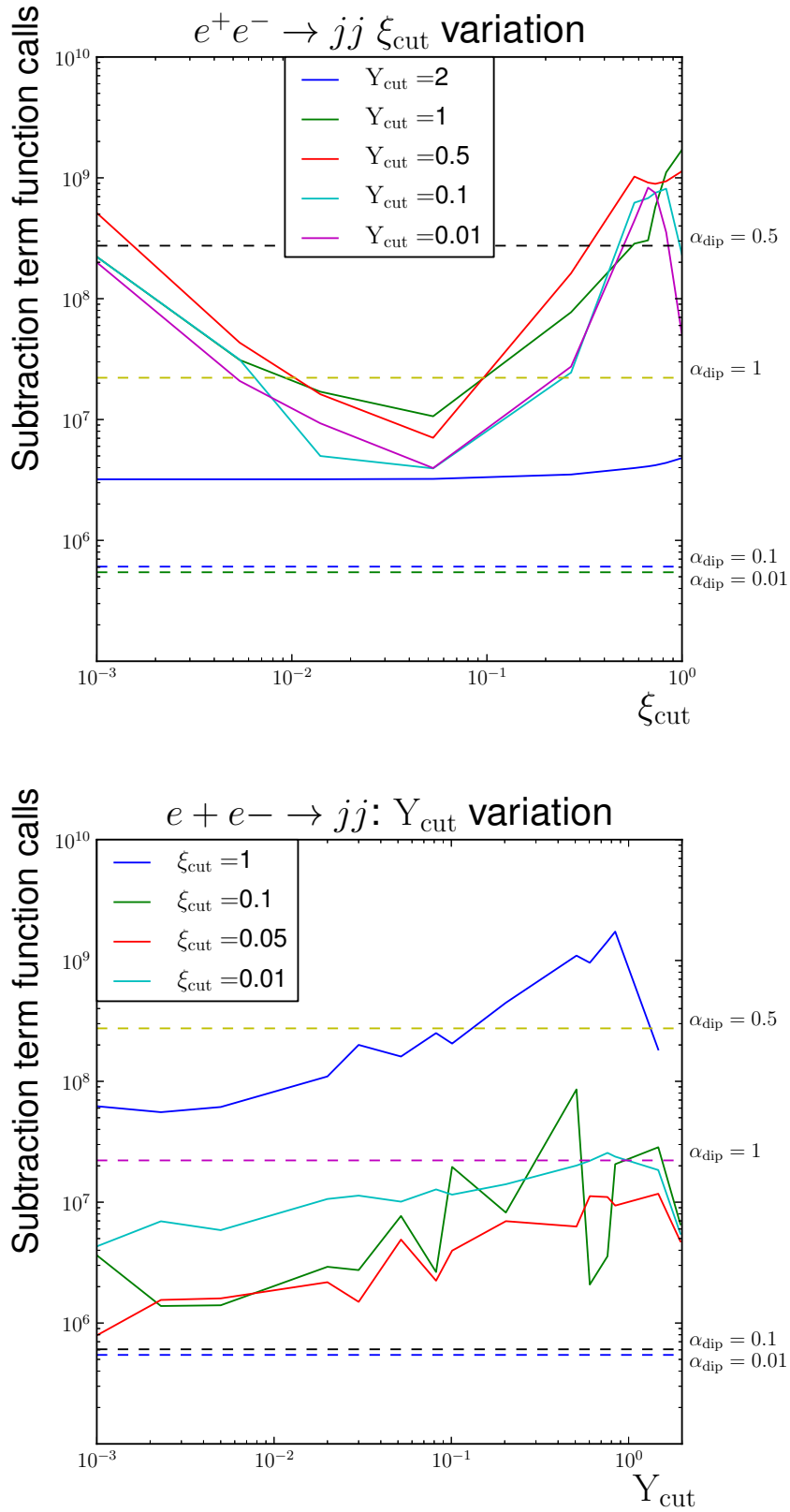


Figure 5.1: The number of function calls for the integration of  $\sigma^{(RS)}$  to 0.1% accuracy for the process  $e^+e^- \rightarrow jj$  for both FKS and Catani Seymour. These are shown against the FKS soft and collinear cutoff parameters  $\xi_{\text{cut}}$  and  $Y_{\text{cut}}$ . Function calls for Catani Seymour runs shown for different values of dipole cutoff parameter,  $\alpha_{\text{dip}}$

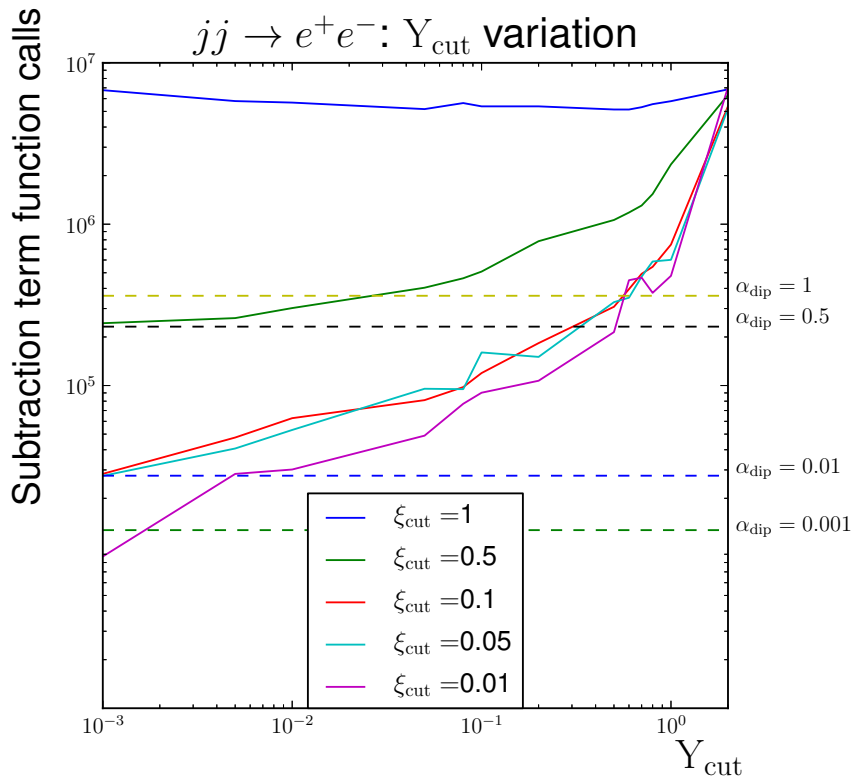
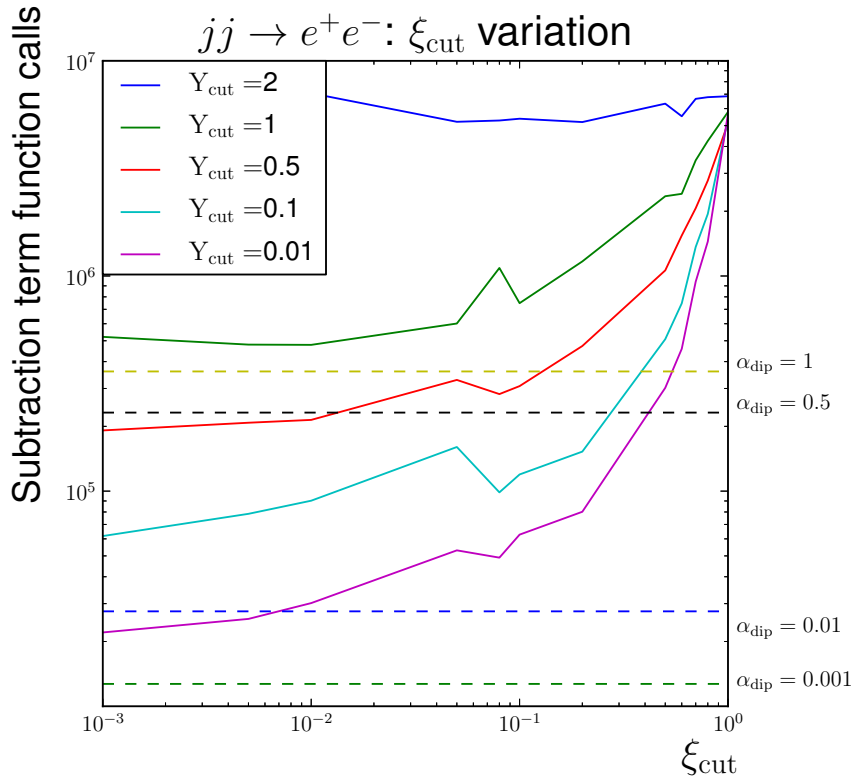


Figure 5.2: The number of function calls for the integration of  $\sigma^{(RS)}$  to 1% accuracy for the process  $jj \rightarrow e^+e^-$  for both FKS and Catani Seymour. These are shown against the FKS soft and collinear cutoff parameters  $\xi_{\text{cut}}$  and  $Y_{\text{cut}}$ . Function calls for Catani Seymour runs shown for different values of dipole cutoff parameter,  $\alpha_{\text{dip}}$

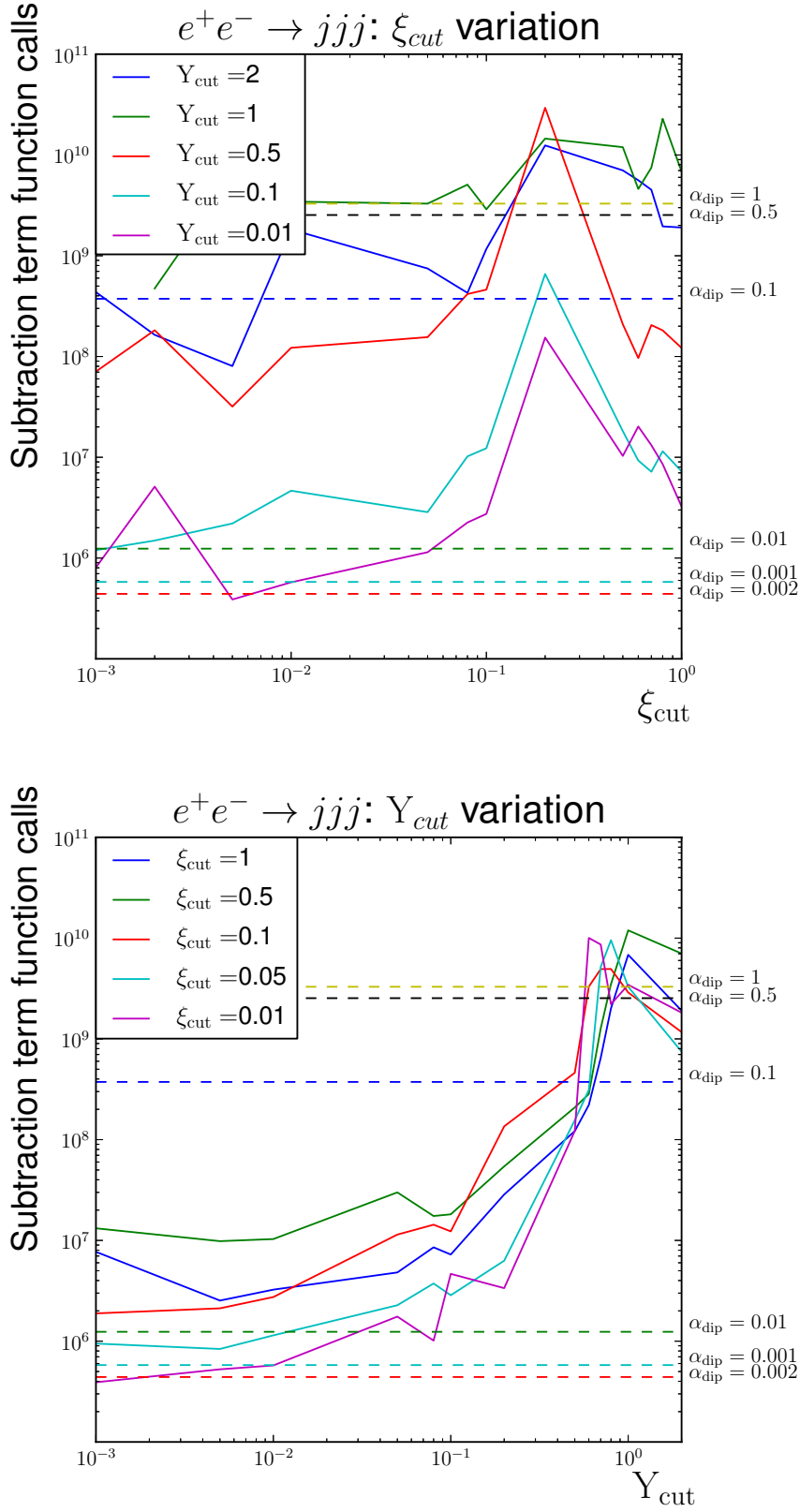


Figure 5.3: The number of function calls for the integration of  $\sigma^{(RS)}$  to 1% accuracy for the process  $e^+e^- \rightarrow jjj$  for both FKS and Catani Seymour. These are shown against the FKS soft and collinear cutoff parameters  $\xi_{cut}$  and  $Y_{cut}$ . Function calls for Catani Seymour runs shown for different values of dipole cutoff parameter,  $\alpha_{dip}$

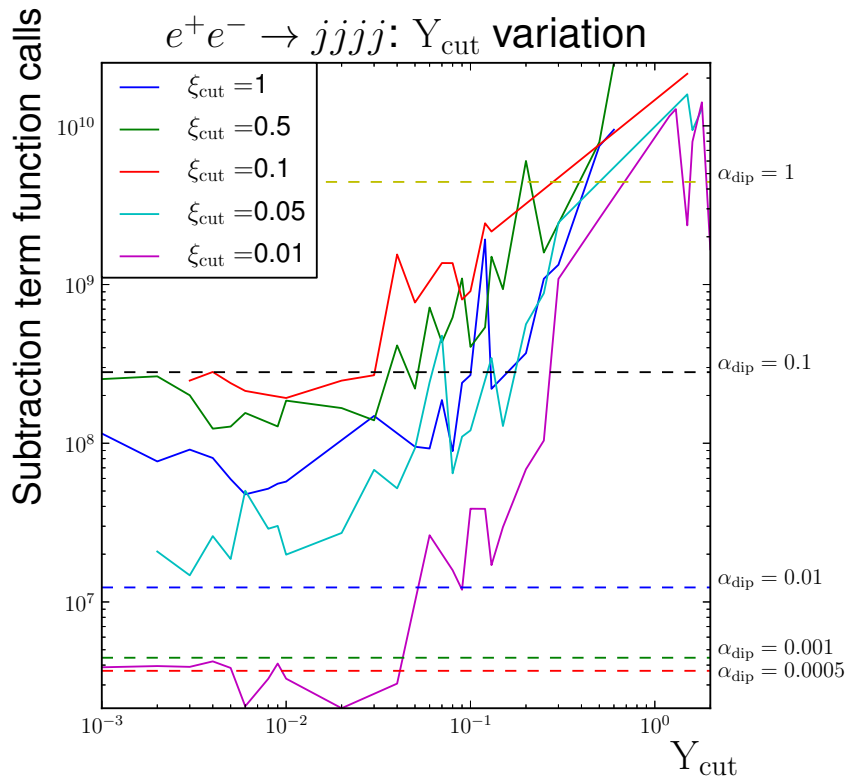
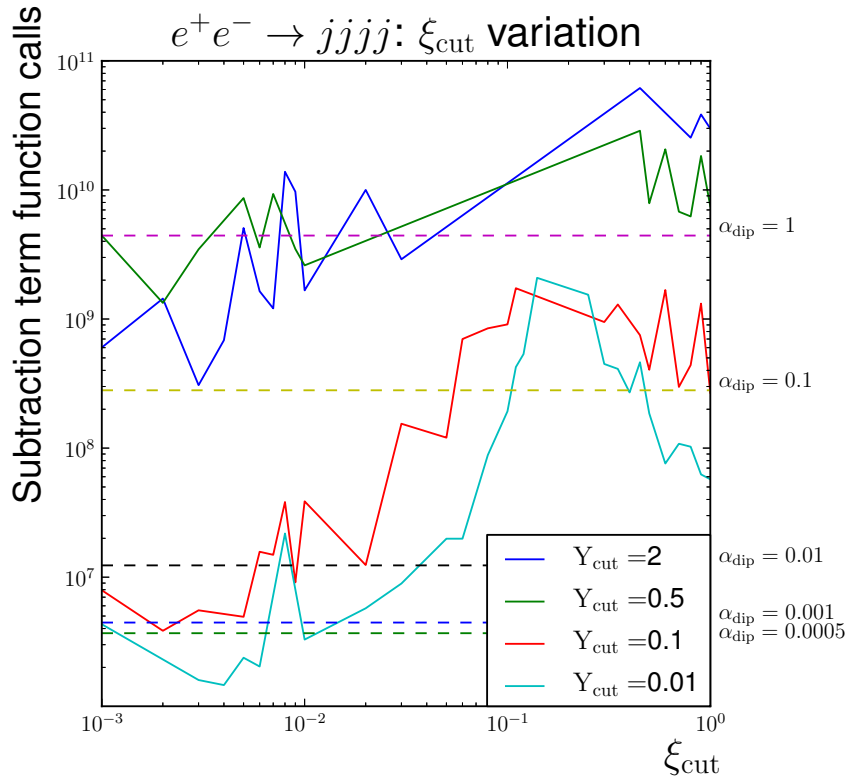


Figure 5.4: The number of function calls for the integration of  $\sigma^{(RS)}$  to 1% accuracy for the process  $e^+e^- \rightarrow jjjj$  for both FKS and Catani Seymour. These are shown against the FKS soft and collinear cutoff parameters  $\xi_{\text{cut}}$  and  $Y_{\text{cut}}$ . Function calls for Catani Seymour runs shown for different values of dipole cutoff parameter,  $\alpha_{\text{dip}}$

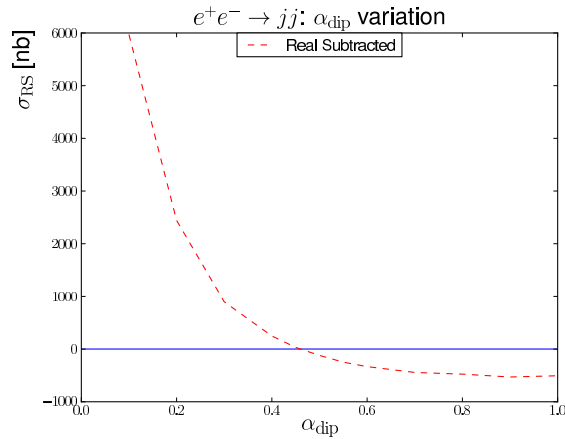


Figure 5.5: The real subtraction calculated in the Catani Seymour subtraction scheme, calculated with  $\alpha_{\text{dip}} \in [1, 0.1]$

comments that are the purpose of this chapter. One obvious feature of these figures is the fluctuations in the function calls that occur in the figures 5.1 to 5.4 over the variation of the cutoff parameters; whilst for most there are clear trends in the number of function calls over cutoff parameter values, it is as clear that fluctuations over these trends occur. While it is not the purpose of this work to precisely determine this effect; it is worth noting that such fluctuations are probably partly caused by inconsistent precision with respect to the Monte Carlo integration of the real subtracted term. The requirement, stated above, that the for these results the real subtracted piece should be integrated to 1% (or 0.1%) accuracy seems at odd with this; however, a more accurate statement of this requirement would be that the real subtracted piece is integrated to atleast 1% (or 0.1%) accuracy. It is also apparent from the results presented in chapter 4 that the numerical values of the real subtraction term in FKS vary quite significantly over the range of cutoff parameters; as an example figure 5.5 is presented which displays the numerical value of the Catani Seymour real subtraction term for various values of  $\alpha_{\text{dip}}$ , calculated for the process  $e^+e^- \rightarrow jj$ . It is seen in figure 5.5 that, without phase space cuts on the subtraction term, the real subtraction term is negative; as the cuts are applied the cross section becomes larger, becoming positive for  $\alpha_{\text{dip}} < 0.45$ . It is also noted that in this region, around  $\alpha_{\text{dip}} = 0.5$ , the Catani Seymour real subtraction term becomes numerically small;

correspondingly it is seen from figure 5.1 that the number of function calls for this process at  $\alpha_{\text{dip}} = 0.5$  show an increase over the  $\alpha_{\text{dip}} = 1$  value. To consider the reason for this, the calculation of the errors in Monte Carlo integrals should be examined. Given that Monte Carlo integrals are simply sums of a function evaluated at random points in the phase space, then the error on this is simply the standard error. For the Monte Carlo integral of a subtracted real term, the error is therefore

$$\delta = \frac{1}{\sqrt{N}} \sqrt{\frac{\sum_{i=1}^N (A_i - B_i)^2}{N} - \frac{\left(\sum_{i=1}^N A_i - B_i\right)^2}{N^2}} \quad (5.7)$$

where  $A_i$  represents the real matrix element and  $B_i$  the subtraction term. The procedure followed in this chapter, for counting subtraction terms, requires that the accuracy of the  $\sigma_{\text{RS}}$  integral is at least 1%; hence it is the fractional error that is of interest to this discussion. For the  $\sigma_{\text{RS}}$  integral this can be written as

$$\frac{\delta}{\sigma_{\text{RS}}} = \frac{1}{\sqrt{N}} \sqrt{\frac{N \sum_{i=1}^N (A_i - B_i)^2}{\left(\sum_{i=1}^N A_i - B_i\right)^2} - 1} \quad (5.8)$$

As can be seen from 5.8 the fractional error is largest, for a given number of phase space points, when the ratio of the sum of the squared (Monte Carlo points) to the square of the sum (of Monte Carlo points), is largest. This is worthy of note, because this ratio should be largest for precisely those values of  $\sigma_{\text{RS}}$  where the real and subtraction terms are similar in size, so the region in figure 5.5 where  $\sigma_{\text{RS}}$  changes sign; a simple example of this is to consider the ratio of the  $x^2+1$  and  $(x+1)^2$  which is largest around region where  $x = -1$ . It is noted that the region of the largest fractional error occurs for cutoff values of around  $\alpha_{\text{dip}} = 0.5$ , which correlates with the peak seen in the number of subtraction term function calls. Given that the fractional error is fixed for the Monte Carlo integration results in this chapter, the effect of relatively large fractional errors would be relatively large numbers of Monte Carlo points necessary to resolve integrals to this fixed fractional error; it is surmised that this effect is the cause of this peak in function calls. Examining the corresponding figures for FKS in chapter four, figures 4.1 to 4.6, it is clear that FKS real subtraction term can, for

some processes take relatively smaller numerical values; it is therefore possible that this can account for some of the fluctuations in the cutoff-function call results for FKS. It is again emphasised that the main design of this chapter is to compare the computational efficiency of the FKS and Catani Seymour subtraction schemes; and that discussion above concerning variations over parameters within such schemes is far from complete, or systematic.

The results plotted in figures 5.1 and 5.2 give the number of subtraction term function calls against the FKS cutoff parameters,  $\xi_{\text{cut}}$  and  $Y_{\text{cut}}$  for  $e^+e^- \rightarrow jj$  and  $jj \rightarrow e^+e^-$ ; with an equivalent range of cutoffs for the Catani Seymour dipoles. From the combinatorics argument for these  $2 \rightarrow 2$  processes it is clear the upper bounds on subtraction terms is lower for Catani Seymour than for FKS, and therefore it might be expected that there are in fact fewer dipole terms than FKS terms. The plots for  $e^+e^- \rightarrow jj$ , both for  $\xi_{\text{cut}}$  and  $Y_{\text{cut}}$  variation show a significantly lower number of subtraction term function calls for Catani Seymour than FKS, seemingly in agreement with the combinatorial argument. Examining the Drell Yan plots a similar agreement can be reached; however, it should be noted that for this process FKS appears to be slightly more competitive.

The results given in figures 5.3 and 5.4 give the number of subtraction term function calls against FKS cutoff parameters, as for 5.1 and 5.2; for the processes  $e^+e^- \rightarrow jjj$  and  $e^+e^- \rightarrow jjjj$ . From combinatorics arguments for the process  $e^+e^- \rightarrow jjj$  the upper bounds on the number of subtraction terms is lower for Catani Seymour; for  $e^+e^- \rightarrow jjjj$ , the upper bounds are the same for both methods. However the results plotted in 5.3 for  $e^+e^- \rightarrow jjj$  show that the number of subtraction terms called for both processes varies between broadly similar numbers of subtraction term calls for an equivalent range of cutoff values. In addition the number of subtractions without cutoffs can be trivially obtained from the code; for  $e^+e^- \rightarrow jjj$  this yields 30 for FKS and 36 for Catani Seymour. This would seem to indicate that for this process FKS and Catani Seymour are broadly equivalent in terms of the speed of the calculation. The results plotted for  $e^+e^- \rightarrow jjjj$ , show the number of calls, considering the vari-

---

ation over equivalent cutoff parameters, is slightly but significantly lower for FKS than Catani Seymour. In addition, the number of subtractions without cutoffs can be trivially obtained from the code, for  $e^+e^- \rightarrow jjjj$  this yields 69 for FKS and 138 for Catani Seymour. This then leads to the obvious conclusion, that for  $e^+e^- \rightarrow jjjj$  FKS calls fewer subtraction terms than Catani Seymour, for equivalent cuts. The results from both  $e^+e^- \rightarrow jjj$  and  $e^+e^- \rightarrow jjjj$  show that the comparisons using the upper bounds on subtraction terms from combinatorics overestimates FKS subtraction terms far more than Catani Seymour terms. However the broad conclusion from combinatorics, that for larger multiplicity processes FKS becomes proportionately more competitive, does indeed hold.

# Chapter 6

## Conclusions to Part I

Part I of this thesis addresses the calculation of next to leading order QCD cross sections, with particular relevance to the real correction term of such calculations. The automation of such calculations in the Monte Carlo event generator SHERPA is the stated aim of this work.

The underlying physics of perturbative QCD has been described in chapter one, providing the necessary theoretical backdrop for NLO calculations. A discussion of aspects of NLO calculations is then presented in chapter two, which addresses the structure such calculations in addition to their motivation; which is usually to reduce errors associated with perturbative scales. The presence of singularities, which are expressed in terms of poles, in the real and virtual parts of NLO calculations is described; while the cancellation of such singularities between these terms is motivated. The difficulty in numerically computing singularity free NLO cross sections is then discussed, with reference to different phase spaces for the real and virtual terms, and the concept of a subtraction scheme introduced. Such schemes subtract a term with an identical singularity structure to the real term; these terms are then added back to the virtual term, after being integrated analytically over the additional one particle phase space present for the real term. These integrated terms contain explicit pole structures which guarantee cancellation of all poles present in the virtual term. The example of the Catani Seymour dipole subtraction is then presented as a demonstration of such a subtraction scheme. In chapter three a review of the FKS subtraction

scheme is presented. This scheme, which constructs subtraction terms by partitioning the real term phase space and taking all allowed singular limits, is described explicitly with all details provided to compute real corrections. In chapter 4 an implementation has been presented which allows the automatic calculation of the real correction using the matrix element generator AMEGIC++; this implementation is based on the FKS subtraction scheme. The full details of this implementation, including the explicit forms of both the real and integrated subtraction used, the kinematic maps for the subtraction and the partitioning functions are presented. Tests of this code have then been performed, to ensure the correct parameter evolution and singular limits of both the subtraction terms and the kinematic maps; all of these tests indicate a properly working implementation.

In chapter 5 a study is presented into the relative efficiency of the FKS and Catani Seymour dipole subtraction schemes. For this work the implementation of FKS subtraction is then used, in conjunction with an implementation of Catani Seymour dipole subtraction within AMEGIC++, to make this comparative study. The comparison of the two schemes, for computational speed, is based on measuring the total number of times the code will call a subtraction term, in order to numerically integrate a real process (using one of the subtraction schemes), to a given accuracy. For this measure results are presented for a wide, but comparable range of cutoff parameters in both schemes. Given these results it is seen that Catani Seymour dipole subtraction is significantly faster for low multiplicity processes, while for higher multiplicity processes ( $n \geq 4$ ) FKS becomes more efficient.

## Part II

# Simulating Photon Induced Processes

# Introduction to Part II

In previous chapters the demand for higher accuracy in theoretical calculations of collider processes has motivated a large body of work surrounding the calculation of higher order corrections in perturbative QCD. Indeed, the first round of data taking at the LHC, which in addition to the Higgs-like boson discovery has led to increasingly stringent bounds on new physics beyond the Standard Model, makes it clear that the focus of experimental analyses at the LHC will shift more and more towards precision measurements and on ever more piercing tests of Standard Model dynamics at the highest scales. There is then a likelihood that there will be a number of observables where high level precision in the theoretical understanding will be crucial in order to match experimental accuracy and allow the full advantage of the high-quality data delivered by the LHC collaborations to be taken. Examples for such processes and observables include

- the large-mass tail of the Drell-Yan mass spectrum, which may be influenced by heavy resonances [42], and
- observables based on the leptons in the pair production of  $W$ -bosons and their subsequent leptonic decays, which may help to shed light on anomalous gauge couplings [5], and which of course play an important role as a background to Higgs production and decay into  $W$  pairs.

In the second part of this thesis the contribution of electroweak corrections, and in particular photon-induced processes, to certain processes will be investigated. Standard considerations of perturbative corrections tend to focus on higher-order QCD corrections, some of which are now available at the next to next to leading order

(NNLO) level at fixed order [43] and at next to leading order in Monte Carlo simulations [35]; however it will be argued that such electroweak corrections may play an important role in order to achieve high level precision in predictions. This will ignore the full wealth of NLO electroweak corrections, calculations of which are available for the processes considered here in [44] [45]; the focus will instead be on photon induced processes, which, formally speaking, are part of the NNLO electroweak contribution. The consideration of such corrections is triggered by two observations:

- recently a second and more modern set of parton distribution functions (PDFs) which include QED effects became available, allowing the comparison of results obtained by the MRST2004QED and the NNPDF2.3QED sets [46,47], focusing of course on the impact of the photon PDF ( $\gamma$ PDF);
- in addition to contributions induced by the photon PDFs, there are also quasi-elastic processes, where the intense electromagnetic fields accompanying the protons give rise to the production of charged particles. Such processes are typically described by the equivalent photon approximation (EPA) or Weizsaecker-Williams method [48], and quite often overlooked. It will be argued here, however, that they become fairly significant when vetoes on the central production of additional particles or jets are applied.

Part two of this thesis is structured thus:

The simulational aspects of SHERPA, which is used to generate these results, are discussed; including a summary of the various modelling stages of the generator. This is followed by an overview of parton showering, including various aspects which are important to this thesis such as the MC@NLO method. Other subjects relevant to the simulations such as the merging of matrix elements and partons, and cluster hadronisation models are also very briefly reviewed. A discussion of the photon induced processes is then presented; this focuses on the motivation for, and description of, the two contributions that form corrections of this sort. The first of these contributions comes from the photon component of hadronic PDFs, a component that arises from QED corrections to the PDF evolution kernels, and which can fairly obviously

give a contribution to photon induced cross sections. This photon PDF component is discussed in chapter 8, where the simple extension of factorisation formulae for calculating photon induced cross sections is presented; the QED corrections to PDF evolution kernels that give rise to the photon component are discussed in this chapter, in addition to a very brief overview of the determination of photon PDFs from data.

The second photon component, the equivalent photon approximation of Weizsaecker and Williams, is then briefly discussed; this includes a summary the approximations' assumptions, in addition to a demonstrating the calculation of photonic cross sections with this method. The distribution functions used for the EPA in SHERPA (and hence for this thesis) are then explicitly presented.

In chapter 9 the setup for the simulation of relevant results is given, and there then follows the presentation of results. This is split according to the two processes simulated, lepton pair production and the production of  $W$  pairs (which are subject to leptonic decays only). In both cases results are presented which compare a QCD baseline with the baseline supplemented with both photon induced channels. These are then compared with relevant data from ATLAS and CMS, where available; the details of experimental analyses used in this section are presented in appendix A. In addition the effect of extra jet emissions is investigated, using the same setup of QCD baseline predictions with photon induced channels as for the above case, for both of the processes. For the case of  $W$  pair production, results are also given simulating the same process at LHC run two energies which is undertaken to test the significance of the photon induced channels at these higher energies. This is with regard to, the possibly that the photon induced rate may be slightly increased as a result of the tails of some distributions at these higher energies. The influence of the photon induced channels is discussed for both channels based on the results presented. Finally the findings of this work are summarised and some conclusions drawn.

# Chapter 7

## Simulating Processes in SHERPA

Before specific discussion of photon induced processes is undertaken, the simulation environment, which takes place in the SHERPA event generator, will be outlined in this chapter, although specific cases relating to photon induced cases will be discussed in chapter 8.

### 7.1 Event Generation in SHERPA

The simulation of events in SHERPA is conducted with a series of many theoretical and technological methods necessary for a modern Monte Carlo event generator. The hard process of the event is calculated using the automatic matrix element generators COMIX [49] and AMEGIC++ [6], which collectively allow the calculation of nearly arbitrary processes with up to eight or more final state particles at tree-level to take place; both of these generators are employed for simulations presented later in this work. In AMEGIC++ the construction of matrix elements is based on the method of helicity amplitudes, a formalism for the automatic generation of which is described in [6]; the helicity amplitude formalism employed here is similar to methods found in [50] [51] and [52]. COMIX however employs Berends-Giele recursion relations, see [53] [54] and [55]; this technique, which is for example also used in ALPGEN [56], is generally more efficient for the calculation of matrix elements with large multiplicities.

The processes calculated by the matrix element generators, which are subject

to parton showering and various other modelling phases, must be integrated over the appropriate phase space. To conduct this integration, SHERPA utilizes multiple weighted channels in which Monte Carlo integration is performed, the use of these multiple weighted channels is outlined in [57] and are automatically generated by SHERPA. The parton showering employed with SHERPA is based on Catani Seymour subtraction terms, as originally proposed in [58] and implemented in [59] and, independently, in [60]; parton showering is reviewed later in this chapter and details of the SHERPA showering are provided. Parton showering in SHERPA can be supplemented by merging with real matrix elements, this merging was originally proposed in [61] and [62], and its implementation within the SHERPA setup is described in [63]. This concept, which will be touched upon in the context of the discussion of parton showers presented later in this chapter, is conducted for some simulations presented later in this thesis.

The inclusion of next to leading order calculations within SHERPA is for these simulations conducted with the Catani Seymour subtraction scheme, the implementation into SHERPA is described in [39]. Where NLO QCD predictions are used the parton shower employs the MC@NLO technique [64], the implementation into SHERPA of which is described in [65], to match the higher order correction to the parton shower; this is discussed in the context of parton showers later in this chapter. After the parton shower, the hadronisation model employed within SHERPA kicks in, this is a modified form of the cluster model, [66] and [67], which is described in [68]; some details of this model will be provided later in this chapter.

## 7.2 Parton Showers

The calculation of cross sections based on fixed order perturbation theory is well established practice in perturbative QCD; however calculations of this nature are often not sufficient to describe experimental set ups. The fixed order perturbative approach has two major flaws for this purpose: one is the high multiplicity of processes in colliders, often as a result of parton cascades, which are infeasible to calculate with

perturbation theory. The second is enhanced contributions from higher orders, which are usually logarithmic in nature and are problematic as corrections to the Born term of more than  $\mathcal{O}(\alpha_s^2)$  are somewhat unfeasible to compute.

To model such effects perturbative QCD is, however, of use in the construction of numerical methods to approximate both parton cascades and enhanced logs from higher order; such numerical methods are known as parton showers.

For the moment a brief digression is taken to radioactive decay processes, where it is noted that the no-decay probability for an unstable isotope obeys

$$\frac{dP}{dt} = -\lambda P \quad (7.1)$$

where  $\lambda$  is the decay constant, and identified as the rate of decay per unit time of the isotope. The solution for the no decay probability is then the familiar  $P = \exp\left(-\int_{t_0}^t dt\lambda\right)$ . The example of radioactive decays is illustrative of the treatment of partons in parton showers; where a partonic branching is the equivalent of the radioactive decay. The decay rate,  $\lambda$ , of the radioactive process therefore has its partonic equivalent in the branching probability; in parton showers these branchings are approximated using the kinematic limits of parton splittings, which are described in chapter one. For most parton showers the collinear branching is considered, analogous to the DGLAP evolution of the parton distribution functions; for such splittings the differential branching probability is described by 7.2.

$$d\mathcal{P}_{\text{branching}} = \frac{dQ'^2}{Q'^2} \int dz \frac{\alpha_s}{2\pi} P_{a_i a_j}(z) \quad (7.2)$$

The no branching probability must, based on the radioactive decay analogy, obey

$$\frac{d\Delta}{dQ^2} = -\Delta(Q^2) \int \frac{dz}{z} \frac{\alpha_s}{2\pi} P_{a_i a_j}(z) \quad (7.3)$$

where  $\Delta$ , the no branching probability, must take the form

$$\Delta(Q^2) = \exp \left[ \int_{Q_0^2}^{Q^2} \frac{dq'^2}{q'^2} \int dz \frac{\alpha_s}{2\pi} P_{a_i a_j}(z) \right] \quad (7.4)$$

and is known as a Sudakov form factor [69]. This Sudakov form factor describes the no branching probability of partons, to rewrite this in a more concrete fashion

the probability of no resolvable branching between scales  $Q$  and  $Q'$  is given by the Sudakov form factor described by

$$\Delta(Q^2, Q'^2) = \exp \left[ - \int_{Q^2}^{Q'^2} \frac{dq'^2}{q'^2} \int_{z_{\min}}^{z_{\max}} dz \frac{\alpha_s}{2\pi} P_{a_i a_j}(z) \right] \quad (7.5)$$

The limits on the partonic fraction,  $z$  integral in the Sudakov form factor are somewhat ambiguously given as  $z_{\min}$  and  $z_{\max}$ ; these values can be determined by considering the kinematics of partons splitting.

This connection with probability allows the construction of a Markov chain of partonic emissions, which is known as parton shower. The algorithm for the construction of a simple parton shower simulation will be presented below; however the structure of calculations in which parton showers are used will be briefly outlined. Typically for collider processes that are of interest a fixed order calculation is conducted for a high-momentum transfer process with low multiplicity, the partonic legs of this calculation are then subject to the chain of partonic emissions, simulated in the parton shower.

To demonstrate the methodology of a parton shower, it will be convenient to return to the radioactive decay process example. In such a process it is noted that the probability of a decay at time  $t$ , given the above, must be given by

$$\mathcal{P}_{\text{Decay}}(t) = \lambda(t) \exp \left( - \int_{t_0}^t dt \lambda(t) \right) \quad (7.6)$$

where the instantaneous decay probability is combined with the probability of it not decaying previously. Hence the probability of a decay in a certain period can be written as

$$\mathcal{P}(t_1, t_2) = \int_{t_1}^{t_2} dt \lambda(t) \exp \left( - \int_{t_0}^t dt \lambda(t) \right) \quad (7.7)$$

where  $\mathcal{P}(t_1, t_2)$  represents the probability a decay will occur at time  $t_2$  given it has not decayed a time  $t_1$ . The idea is to use this probability distribution to randomly generate a decay event; this proceeds by generating a random number  $\mathcal{R} \in [0, 1]$  and

by making the identification:

$$\int_0^{t_{\text{Decay}}} dt \mathcal{P}_{\text{Decay}}(t) = \mathcal{R} \int_0^{\infty} dt \mathcal{P}_{\text{Decay}}(t) \quad (7.8)$$

the generation of a random number can therefore be used to 'generate' a decay event; with the decay time calculated from 7.8. In the case of the radioactive decay process, this can be computed to be

$$1 - \exp\left(-\int_0^{t_{\text{Decay}}} dt \lambda(t)\right) = \mathcal{R} \quad (7.9)$$

The decay time of a radioactive nuclei, in this example, can thus be generated by solving the expression

$$\exp\left(-\int_0^{t_{\text{Decay}}} dt \lambda(t)\right) = \mathcal{R}' \quad (7.10)$$

for  $t_{\text{Decay}}$ ; where  $\mathcal{R}' \in [0, 1]$  is another random number, equivalent to  $1 - \mathcal{R}$ . It is seen the expression of the LHS of this equation is the no decay probability. This algorithm can be applied to the branching of partons in an analogous fashion. Therefore to generate partonic branchings at a particular momentum scale the no branching probability, represented by the Sudakov, must be equated to a random value to generate a branching scale. Hence the branching scale of a parton in the parton shower is simulated by generating a random number, and making the identification

$$\Delta(Q^2, Q_{\text{Branch}}^2) = \mathcal{R}' \quad (7.11)$$

[69] where  $\mathcal{R}'$  is also a random number  $\in [0, 1]$  and  $Q$  is the initial momentum scale for the parton in question.

The solution of 7.11 for the scale  $Q_{\text{Branch}}^2$  therefore determines the scale at which a simulated branching will take place. Thus generating random numbers in this context amounts to generating the next branching; these chains of generated branchings then continue until the branching scale  $Q_{\text{Branch}}$  falls below the scale for a resolvable emission. This nicely allows the determination of the branching scales of partons in the final state, however this does not uniquely determine the kinematics of daughter

partons. For collinear branching (which is what is considered by using DGLAP evolution) the kinematics of the daughter partons amounts to a choice of the partonic fraction,  $z$  and again this value is generated by using random numbers. This is simply accomplished by making the identification

$$\int_{z_{\min}}^z dz \frac{\alpha_s}{2\pi} P(z) = \mathcal{R}' \int_{z_{\min}}^{z_{\max}} dz' \frac{\alpha_s}{2\pi} P(z') \quad (7.12)$$

where  $\mathcal{R}' \in [0, 1]$  is a second random number. Therefore a solution of 7.12 for  $z$  determines the generated partonic fraction.

The treatment of initial state radiation is similar to that of final state radiation, however it is complicated by kinematic considerations. For final state branching the scale is simply evolved downwards until it falls below the scale of resolvable emission, however this cannot be simply repeated for initial state branching due to the need to match the kinematics of the initial state partons of the hard process. The parton shower algorithm is modified such that the scale is evolved backwards from the hard scale process towards the hadron. A consequence of this is that the Sudakov form factor is modified by the PDFs; the probability of no branching between two scales in the initial state evolution is given by

$$\Pi(Q^2, Q'^2, x) = \frac{f(x, Q^2)}{f(x, Q'^2)} \Delta(Q^2, Q'^2) \quad (7.13)$$

[9], which is equivalent to

$$\Pi(Q^2, Q'^2, x) = \exp \left[ - \int_{Q'^2}^{Q^2} \frac{dq'^2}{q'^2} \int dz \frac{\alpha_s}{2\pi} P_{a_i a_j}(z) \frac{f(x/z, Q'^2)}{f(x, Q'^2)} \right] \quad (7.14)$$

This gives a modified Sudakov form factor which can be used in an algorithmic fashion similar to the final state forward branching; branching is said to have occurred at scale  $Q'^2$  which is generated from

$$\Pi(Q^2, Q'^2) = \mathcal{R} \quad (7.15)$$

where again use is made of random variables to generate the splitting scale.

The partonic fraction  $z$  is determined by generating a second random variable in the same fashion as for final state radiation; however there is again a slight modification from PDFs which in the expression yields

$$\int_{z_{\min}}^z dz \frac{\alpha_s}{2\pi} \frac{P(z')}{z'} f(x/z') = \mathcal{R}' \int_{z_{\min}}^{z_{\max}} dz' \frac{\alpha_s}{2\pi} \frac{P(z')}{z} f(x/z') \quad (7.16)$$

Where the value  $x$  indicates the partonic fraction of the daughter parton. The solution of 7.16 for  $z$  allows the determination of the partonic  $z$  for initial state splitting.

The Markov chain of parton emissions, as has been described above, gives an approximation for high-multiplicity final states; however, parton showers also provide enhanced contributions from higher orders in addition to an approximation of the leading order matrix element for a high-multiplicity event. These enhanced contributions enter via the Sudakov form factor, which has hitherto been simply treated as a no-branching probability (which it still is at leading order). The enhanced contributions are logarithmic in nature and come from both virtual terms and unresolved emissions. At this point it is worth considering the form of the exponent in the Sudakov form factor, it is fairly clear that this exponent is logarithmic in the scale  $Q$  from simple integration. However an additional logarithmic contribution can result from the integrals of some splitting functions. Considering only these double logarithmic terms the Sudakov form factor can be written as

$$\Delta(Q^2, Q_0^2) \approx \exp\left(-k_F \frac{\alpha_s}{2\pi} \log^2 \frac{Q^2}{Q_0^2}\right) = 1 - k_F \frac{\alpha_s}{2\pi} \log^2 \frac{Q^2}{Q_0^2} + \dots \mathcal{O}\left(\alpha_s^n \log^{2n} \frac{Q^2}{Q_0^2}\right) \quad (7.17)$$

where  $k_F$  is a generic factor from the splitting functions (whose precise form is not relevant for this purpose). It is clear that a series expansion of the Sudakov form factor involves an infinite series of these logarithmic terms. These terms, which as can be seen occur at an arbitrary order of  $\alpha_s$ , represent the enhanced pieces from higher fixed order contributions and can in some regions become large which presents a problem for simple fixed order calculations. However the inclusion of Sudakov will implicitly sum all such contributions to all orders. The technique of including a series

of logarithmic contributions to all orders in  $\alpha_s$  is known as resummation, which is a broader technical field in its own right beyond parton showers; the formal logarithmic accuracy of parton showers is dependent upon the details of the shower, however all include an all orders resummation of the double logarithms shown in the above example [70].

In the above discussion, the definition of the ordering scale,  $Q^2$ , has been left deliberately vague; there is some ambiguity in the choice of this scale which is reflected in different choices in different shower implementations. In earlier versions of the event generator PYTHIA the invariant mass scale of the parton is used, see [71] [72] however later versions are ordered by transverse momenta [73].

Ordering with respect to the angle between branching partons, known as angular ordering, is implemented in the event generator HERWIG++, see [74] and [75]. Angular ordering of showers is a largely used as a result of its ability to approximate some of the soft logarithmic terms present, that for example are not approximated in an invariant mass ordered shower. This is simply the result of the form of matrix elements in the soft gluonic limit. When the angle between the soft gluon and a parton becomes large with respect to the angular 'scale' at which the parton branches, interference effects in the matrix element largely mean that the soft gluonic emission can be neglected. When the opposite is true, the soft gluonic splitting can give a sizeable contribution however, such terms can then be modelled as a previous collinear branching in the angularly order shower. As a result showers ordered in this fashion implicitly approximate large soft contributions (from both branching and higher orders), in addition to the collinear terms.

### 7.2.1 Parton Showering in SHERPA

The parton showering algorithm introduced for the more general discussion above implicitly described the parton shower by using the DGLAP evolution, and therefore implicitly the use of Altarelli-Parisi splitting functions to approximate the par-

ton branching. While it is perfectly possible to construct a modern shower algorithm based in these splitting functions, this is not the choice taken in SHERPA. In SHERPA the place of Altarelli-Parisi splitting functions is taken by Catani Seymour dipole subtraction terms, which are spin-averaged (so there is no tensorial dependence). This choice is taken as the dipole functions, which include both singular limits, allow the resummation of soft logarithmic terms when used in the shower. While this can be achieved in DGLAP showers by angular ordering, this presents its own set of problems. The formulation of dipole showers was first outlined in [58] and [76] and the implementation of this formalism was then made in SHERPA [59]; the key results of which are summarised in this section.

Catani Seymour dipole functions were originally formulated to allow a general method for the construction of subtraction terms for use in the real terms of NLO calculations; as a result of this these dipole functions represent the singular limits of a parton in a cross section. Consequently they can be adapted for use as splitting functions, and given the limit that a branched parton is nearly soft or collinear, can be used to express a  $m + 1$  particle cross section in terms of a  $m$  particle one; this is expressed in 7.18.

$$d\sigma_{m+1} = d\sigma_m \sum_{ij} \sum_{k \neq i,j} \frac{dy_{ij,k}}{y_{ij,k}} dz \frac{d\phi}{2\pi} \frac{\alpha_s}{2\pi} \frac{1}{N} J(y_{ij,k}) \langle V_{ij,k}(z, y_{ij,k}) \rangle \quad (7.18)$$

Where spin-averaged Catani Seymour dipoles are expressed as  $V_{ij,k}(z, y_{ij,k})$ , with a Jacobian factor  $J(y_{ij,k})$  and where the partonic labels  $i, j$  and  $k$  refer to the branching of a parton into partons  $i$  and  $j$  where  $k$  is a spectator. The variables  $z$  and  $y_{ij,k}$  are defined functions of the three partons  $i, j$  and  $k$  momenta; for massless final state partons these are expressed below.

$$z = \frac{p_i \cdot p_k}{p_i \cdot p_k + p_j \cdot p_k} \quad y_{ij,k} = \frac{p_i \cdot p_j}{p_i \cdot p_j + p_i \cdot p_k + p_j \cdot p_k} \quad (7.19)$$

The Jacobian factor  $J(y_{ij,k})$  allows the one particle phase space integral, over the additional parton momenta, to be expressed in terms of the relevant kinematic variables of the dipole function,  $z$  and  $y_{ij,k}$  in addition to an angular integral  $d\phi$ . These

variables define the mapping of kinematics between the mother and daughter partons as well as a shift for the spectator. Shown below is this mapping from mother to daughter partons; the mother kinematics are denoted as  $\tilde{p}$  and daughter kinematics as  $p$ .

$$p_i = z\tilde{p}_{ij} + \frac{k_\perp^2}{z\tilde{p}_{ij}\cdot\tilde{p}_k}\tilde{p}_k + k_\perp \quad (7.20)$$

$$p_j = (1-z)\tilde{p}_{ij} + \frac{k_\perp^2}{(1-z)\tilde{p}_{ij}\cdot\tilde{p}_k}\tilde{p}_k - k_\perp \quad (7.21)$$

$$p_k = (1 - y_{ij,k})\tilde{p}_k \quad (7.22)$$

where  $k_\perp$  is the transverse momenta of the branched partons  $i$  and  $j$  with respect to the mother parton  $\tilde{i}$ ; this can be related to  $y_{ij,k}$  as

$$y_{ij,k} = \frac{-k_\perp^2}{z(1-z)(p_i\cdot p_j + p_i\cdot p_k + p_j\cdot p_k)} \quad (7.23)$$

It is noted that this form of the kinematic variable  $y_{ij,k}$  allows the following identification to be made

$$\frac{dk_\perp^2}{k_\perp^2} = \frac{dy_{ij,k}}{y_{ij,k}} \quad (7.24)$$

This is important as to construct a parton shower algorithm, a scale with which to evolve the shower must be chosen, and the transverse momenta of branched partons can be used as such a scale. Given that the conventional parton shower algorithms are based on approximating the cascade of partonic branching with Altarelli-Parisi splitting functions, the identification of the Catani Seymour dipoles as splitting functions, in both the soft and collinear limits, as described above, motivates the possibility of constructing such a shower based on the dipoles. The construction of such a parton shower algorithm requires a Sudakov form factor, and in analogy with the DGLAP case the Sudakov for dipole showering can be expressed as

$$\Delta_{ij,k}^{(\mathcal{K})}(t, t_0) = \exp \left[ - \int_{t_0}^t \frac{dt}{t} \frac{\alpha_s}{2\pi} \int dz \frac{d\phi}{2\pi} \mathcal{K}_{ij,k}(t, z, \phi) \right] \quad (7.25)$$

where  $\mathcal{K}_{ij,k}(t, z, \phi)$  represent the spin-averaged Catani Seymour dipole functions and the Jacobian factor, and where for convenience transverse momenta is expressed as  $k_\perp^2 = t$ . Again as the dipole function performs the role of approximating the branching

of the cross section, as the Altarelli-Parisi splitting functions do in the collinear case, this Sudakov can be interpreted as a no branching probability. The shower algorithm described in the previous section can therefore be used to construct the dipole shower simply by replacing the Sudakov form factor with the dipole form shown above and utilizing the dipole functions to approximate the branching that occurs, as opposed to the Altarelli-Parisi splitting functions. In addition this formulation of the parton shower requires the ordering of the shower by  $k_{\perp}^2$ .

### 7.2.2 NLO calculations and Parton Showers

The use of parton showers for simulating collider events is well motivated, given the ability of these algorithms to approximate to a high degree large jet multiplicities in such events; in addition to implicitly resumming enhanced logarithmic corrections which are beyond leading order in the strong coupling. However the inclusion, where possible, of NLO corrections to the hard processes simulation are equally well motivated; principally so by reductions in the error associated with certain perturbative scales, which must be introduced into fixed order calculations, such as the renormalisation and factorisation scales. Combining both of these techniques for Monte Carlo simulations is therefore of high importance for providing accurate predictions. However, an NLO hard process calculation cannot be simply supplemented by a parton shower using the parton shower algorithm presented earlier in this chapter for use with Born level processes.

The principle difficulty arises because the parton shower resums the leading logarithmic terms of parts of the NLO calculation, hence to simply attach a conventional parton shower to a hard process, which is calculated at NLO, double counts these terms. To consider this issue it is first prudent to examine the form of an NLO calculation, since all calculations which will be parton showered will be calculated using a subtraction scheme; the form of the NLO calculation considered here will utilize a subtraction scheme. The form of these calculations, which is expressed below, consists of, in addition to the leading order Born term, a virtual term calculated from loop diagrams and a real emission term which is Born like but includes an additional

unconstrained parton; these are supplemented by terms from the subtraction scheme.

$$\sigma_{\text{NLO}} = \int_m d\sigma^{(B)} + \int_m \left[ d\sigma^{(V)} + \int_1 d\sigma^{(S)} \right] + \int_{m+1} \left[ d\sigma^{(R)} - d\sigma^{(S)} \right] \quad (7.26)$$

Given the structure of a parton shower the terms which can cause  $\mathcal{O}(\alpha_s)$  corrections, and hence give an approximation to the NLO calculation, have two components; firstly the Sudakov form factor itself, from the  $\mathcal{O}(\alpha_s)$  term in the expansion of the exponential, and the first branching term, which can approximate part of the real emission term. Considering a parton shower which uses a generic evolution kernel  $\Gamma(\Phi_1)$ , where the Sudakov is represented by 7.27;

$$\Delta(Q^2, Q'^2) = \exp \left( - \int_{Q^2}^{Q'^2} d\Phi_1 \Gamma(\Phi_1) \right) \quad (7.27)$$

then the appropriate terms to consider from the parton shower are given by 7.28.

$$d\sigma^{\text{PS}} = d\sigma^{(B)} \left[ \Delta(Q^2, Q_0^2) + \int_{Q_0^2} d\Phi_1 \Gamma(\Phi_1) \Delta(Q^2, Q_{\Phi_1}^2) \right] \quad (7.28)$$

The scales  $Q^2$ ,  $Q_0^2$  and  $Q_{\Phi_1}^2$  respectively represent the starting scale of the shower, the cutoff scale, and scale of the first emission. To properly match NLO calculations to parton showers, these terms that are double counted in the shower and the NLO calculation must be properly accounted for. A set prescription for this procedure does not exist, but there are two principle methods, known as MC@NLO [64] and POWHEG [77]; generic considerations about matching parton showers to fixed order NLO calculations are considered in [65].

To perform such a matching is not a simple task, as the parton shower approximation does not distinguish between corrections associated from real or virtual corrections but combines elements of both where such double counting occurs; the offending pieces of the parton shower therefore cannot simply be subtracted off the fixed order calculation. To perform an appropriate matching both the MC@NLO and POWHEG methods begin by considering the form of the parton shower evolution kernel  $\Gamma(\Phi_1)$ . This object must, by the construction of a parton shower, approximate

the branching of a partonic cross section and therefore must also approximate to the ratio of real-emission to Born in an NLO calculation; for example the Altarelli-Parisi splitting functions approximate this ratio in the collinear limit. At this point it is appropriate to partition the real emission term into finite and singular pieces;

$$d\sigma^{(R)} = d\Phi_{m+1} \mathcal{R}(\Phi_{m+1}) = d\Phi_{m+1} [\mathcal{R}^F(\Phi_{m+1}) + \mathcal{R}^S(\Phi_{m+1})] \quad (7.29)$$

where the terms  $\mathcal{R}^F(\Phi_{m+1})$  and  $\mathcal{R}^S(\Phi_{m+1})$  are the finite and singular pieces of the real term respectively. It is clear that the approximation of the real to Born ratio by the kernel must occur in the singular limits of the real emission term, so the identification

$$\Gamma(\Phi_1) = \frac{\mathcal{R}^S(\Phi_{m+1})}{\mathcal{B}(\Phi_m)} \quad (7.30)$$

can be made, where  $\mathcal{B}(\Phi_m)$  denotes the Born level matrix element squared.

Using these definitions the NLO calculation with the relevant parton shower double counting subtracted can be schematically described by:

$$d\sigma^{\text{NLO PS}} = \left[ d\sigma^{(B)} + d\sigma^{(V)} + \int_1 d\sigma^{(S)} + d\Phi_{m+1} (\mathcal{R}^S(\Phi_{m+1}) - D^{\text{sub}}(\Phi_{m+1})) \right] \\ \times \left[ \Delta(Q^2, Q_0^2) + \int_{Q_0^2} d\Phi_1 \frac{\mathcal{R}^S(\Phi_{m+1})}{\mathcal{B}(\Phi_m)} \Delta(Q^2, Q_{\Phi_1}^2) \right] + d\Phi_{m+1} \mathcal{R}^F(\Phi_{m+1}) \quad (7.31)$$

where  $D^{\text{sub}}(\Phi_m)$  are the functional form of the subtraction terms defined such that

$$d\sigma^{(S)} = d\Phi_{m+1} D^{\text{sub}}(\Phi_{m+1}) \quad (7.32)$$

The differential form 7.31, when integrated over the full phase space must yield normal NLO cross section. The form of the singular and finite pieces of the real term therefore determine the method of NLO parton showering matching; it is noted that a choice of how this partition occurs will also determine the evolution kernel that is used in the parton shower. The choice employed in the MC@NLO formalism amounts to identifying the singular component of the real term as the subtraction term(s) used

in the NLO calculation, this greatly simplifies the above expression and yields

$$\begin{aligned} d\sigma^{\text{MC@NLO}} = & \left[ d\sigma^{(B)} + d\sigma^{(V)} + \int_1 d\sigma^{(S)} \right] \left[ \Delta^{\text{MC@NLO}}(Q^2, Q_0^2) \right. \\ & \left. + \int_{Q_0^2} d\Phi_1 \frac{D^{\text{sub}}(\Phi_{m+1})}{\mathcal{B}(\Phi_m)} \Delta^{\text{MC@NLO}}(Q^2, Q_{\Phi_1}^2) \right] + d\Phi_{m+1} [\mathcal{R}(\Phi_{m+1}) - D^{\text{sub}}(\Phi_{m+1})] \end{aligned} \quad (7.33)$$

where it is noted that the parton showering must now occur with subtraction terms used in the NLO calculation as evolution kernel. As result the Sudakov form factor must take the form

$$\Delta^{\text{MC@NLO}}(Q^2, Q'^2) = \exp \left( - \int_{Q^2}^{Q'^2} d\Phi_1 \frac{\alpha_s}{2\pi} D^{\text{sub}}(\Phi_{m+1}) \right) \quad (7.34)$$

This summarizes the MC@NLO method first described in [64], although the form that is given here is taken from [65].

The POWHEG method, in the formalism of 7.31 amounts to making the choice of  $\mathcal{R}^S(\Phi_{m+1}) = \mathcal{R}(\Phi_{m+1})$ .

$$d\sigma^{\text{POWHEG}} = d\bar{\sigma}^{(B)} \left[ \Delta^{\text{POWHEG}}(Q^2, Q_0^2) + \int_{Q_0^2} d\Phi_1 \frac{\mathcal{R}(\Phi_{m+1})}{\mathcal{B}(\Phi_m)} \Delta^{\text{POWHEG}}(Q^2, Q_{\Phi_1}^2) \right] \quad (7.35)$$

Where the factor  $d\bar{\sigma}^{(B)}$  is simply the differential form of the NLO cross section.

$$d\bar{\sigma}^{(B)} = d\sigma^{(B)} + d\sigma^{(V)} + \int_1 d\sigma^{(S)} + d\Phi_{m+1} [\mathcal{R}(\Phi_{m+1}) - D^{\text{sub}}(\Phi_{m+1})] \quad (7.36)$$

Again this forces the kernel of the showering algorithm to take the new form, in this case the ratio of the real to Born terms. As result the Sudakov form factor must take the form

$$\Delta^{\text{POWHEG}}(Q^2, Q'^2) = \exp \left( - \int_{Q^2}^{Q'^2} d\Phi_1 \frac{\mathcal{R}(\Phi_{m+1})}{\mathcal{B}(\Phi_m)} \right) \quad (7.37)$$

for POWHEG.

Both of these formalisms force the evolution kernel of the shower to take a particular form, however this can be problematic for defining a parton shower algorithm. This is the case for the MC@NLO method, where the evolution kernel in the Sudakov form factor can take negative values; as a result such a Sudakov could not be used to describe a no branching probability. This issue is addressed by use of a modified form of the well known veto algorithm [78], found in [79]. The veto algorithm, as commonly used in parton shower algorithms, allows for the generation of parton branchings for showers, with evolution kernels that do not have a known integral. The generation of a branching scale proceeds, as given in 7.11 and using the notation of 7.27, is given by

$$\Delta(Q^2, Q_{\text{Branch}}^2) = \exp \left( - \int_{Q^2}^{Q'^2} d\Phi_1 \Gamma(\Phi_1) \right) = \mathcal{R}' \quad (7.38)$$

If the integral of the kernel,  $\Gamma(\Phi)$  is unknown, then computing the branching scale from 7.11 presents difficulties. The veto algorithm resolves this by defining a new function,  $g(\Phi)$  which has a known integral and provides an overestimate of  $\Gamma(\Phi)$  (i.e.  $g(\Phi) \geq \Gamma(\Phi)$ ) and generating branching scales by

$$\exp \left( - \int_{Q^2}^{Q'^2} d\Phi_1 g(\Phi_1) \right) = \mathcal{R}' \quad (7.39)$$

Which, as  $g(\Phi)$  has a known integral, can be used to compute a branching scale. The branchings generated by 7.41 are then accepted as branchings for the parton shower, with a probability  $\Gamma(\Phi)/g(\Phi)$ . The branching probability, using the veto algorithm then takes the form

$$P_{\text{Branch}}(Q'^2) = \frac{\Gamma(\Phi_1)}{g(\Phi_1)} \int_{Q^2}^{Q'^2} d\Phi_1 g(\Phi_1) \exp \left( - \int_{Q^2}^{Q'^2} d\Phi_1 g(\Phi_1) \right) \quad (7.40)$$

To deal with kernels that can take negative values, the algorithm is modified by introducing an additional overestimate function,  $h(\Phi)$ , which is always positive; this procedure also requires that  $\Gamma(\Phi)/g(\Phi)$  remains positive. Branching scales are then

generated with

$$\exp\left(-\int_{Q^2}^{Q'^2} d\Phi_1 h(\Phi_1)\right) = \mathcal{R}' \quad (7.41)$$

and are again accepted with a probability  $\Gamma(\Phi)/g(\Phi)$  (hence this quantity must be positive). The distributions generated from these steps then have weights applied to them; these are expressed below

$$W_{\text{Branch}} = \frac{h(\Phi)}{g(\Phi)} \quad W_{\text{No Branch}} = \frac{h(\Phi) h(\Phi) - f(\Phi)}{g(\Phi) g(\Phi) - f(\Phi)} \quad (7.42)$$

for branched and unbranched events respectively. It is noted that the weighting procedure for the additional overestimate function,  $h(\Phi)$  is applied analytically as opposed to the probabilistic 'hit and miss' of the previous overestimate function  $g(\Phi)$ .

In SHERPA the NLO matching scheme which is utilized for the simulation of results presented in this thesis is the MC@NLO formalism. In the SHERPA implementation the calculation of the NLO term is conducted with Catani Seymour dipoles, and as a result the MC@NLO calculation as presented above also utilizes these subtraction terms. The parton showering therefore must occur using these subtraction terms as the evolution kernel, which SHERPA natively employs for this purpose anyway.

### 7.2.3 Merging Matrix Elements with Parton Showers

The combination of NLO fixed order calculations and parton showers described in the previous section, accomplishes a merging of the NLO calculations and parton showers by removing terms in the parton shower which caused the double counting of certain logarithmic corrections included in the parton shower. A principle part of these corrections relate to the real emission term of the NLO calculation, which in essence is simply a tree level matrix element term with an additional partonic leg (compared to the Born term). While this extra partonic leg, in the NLO case, becomes unresolved for the real correction term, corrections for this term can motivate correcting the parton shower for hard partonic emissions described by tree-level matrix elements. The correction of a leading order parton shower to include the matrix element for the

first partonic emission, above the merging scale  $Q_{\text{MS}}$ , can be motivated by equation 7.31 to take the form 7.43.

$$\begin{aligned} d\sigma^{\text{CKKW}} = d\Phi_{m+1}\mathcal{B}(\Phi_m) & \left[ \Delta(Q^2, Q_0^2) + \int_{Q_0^2} d\Phi_1 \Theta(Q_{\text{MS}}^2 - Q_{\Phi_1}^2) \Gamma(\Phi_1) \Delta(Q^2, Q_{\Phi_1}^2) \right. \\ & \left. + \int_{Q_0^2} d\Phi_1 \frac{\mathcal{R}(\Phi_{m+1})}{\mathcal{B}(\Phi_m)} \Theta(Q_{\Phi_1}^2 - Q_{\text{MS}}^2) \Delta(Q^2, Q_{\Phi_1}^2) \right] \quad (7.43) \end{aligned}$$

Where again the Sudakov form factor is defined with an abstract kernel  $\Gamma(\Phi_1)$ , yielding

$$\Delta(Q^2, Q'^2) = \exp \left( - \int_{Q^2}^{Q'^2} d\Phi_1 \Gamma(\Phi_1) \right) \quad (7.44)$$

It is seen that this expression, for the first emission process in the parton shower, showers normally for emission scales below the merging scale  $Q_{\text{MS}}^2$ ; however if the first emission process is above the merging scale the Born hard process matrix element is replaced by tree-level matrix element for an additional partonic emission (compared to the Born term). Therefore this formalism simply corrects the hard process to include an extra jet emission if this jet emission is sufficiently hard itself. It is noted that performing this procedure has the effect that the parton shower contributions no longer integrate, over the full phase space, to unity; although this effect is not problematic if the merging scale is chosen appropriately.

While this approach is effective, it can be extended beyond the first emission in the parton shower; this can be accomplished by performing the same procedure used to correct the Born level parton shower to the extra emission term. This corrects the first emission for this hard process; the procedure can then be used iteratively to correct for hard emissions (those greater than the merging scale) for any emission in the parton shower. The correction to the real emission hard process term of the

parton shower can therefore be expressed as

$$\begin{aligned}
d\sigma^{\text{CKKW-L}} = & d\Phi_{m+1} \mathcal{R}(\Phi_{m+1}) \Theta(Q_{\Phi_1}^2 - Q_{\text{MS}}^2) \Delta(Q^2, Q_{\Phi_1}^2) \\
& \left[ \Delta(Q_{\Phi_1}^2, Q_0^2) + \int_{Q_0^2} d\Phi_1 \Theta(Q_{\text{MS}}^2 - Q_{\Phi_1}^2) \Gamma(\Phi_1^2) \Delta(Q^2, Q_{\Phi_1}^2) \right. \\
& \left. + \int_{Q_0^2} d\Phi_1^2 \frac{\mathcal{R}_2(\Phi_{m+2})}{\mathcal{R}(\Phi_{m+1})} \Theta(Q_{\Phi_1}^2 - Q_{\text{MS}}^2) \Delta(Q_{\Phi_1}^2, Q_{\Phi_1}^2) \right] \quad (7.45)
\end{aligned}$$

where the term  $\mathcal{R}_2(\Phi_{m+1})$  is the tree-level term with two additional partonic emissions relative to the Born and  $\Phi_1^2$  represents the additional partonic phase space for the second emission. These formalisms for the merging of matrix elements and parton showers are known as the CKKW and CKKW-L procedures for the first and multi emission corrections respectively, and are described by [61] and [62]. The implementation of these procedures into SHERPA is described in [63].

There are various technicalities in this procedure which have been glossed over in this brief overview, examples of which include the running of the strong coupling in the parton shower; for matrix element calculations a consistent value of  $\alpha_s$  must be used while in a parton shower the scale of this coupling changes with the shower and is generally corrected for by an additional weighting factor. Other issues include the corrections for initial state radiation and choices of scale, which are described in [63].

This multi-jet merging scheme can be combined with NLO matching methods to produce hard emissions, usually just the initial process, at NLO. The MENLOPS formalism [80] and [81] combines the POWHEG method, summarised in equation 7.35 with the multi-jet merging described above. While this method is somewhat involved and will not be described in detail, its essentials are as follows; the Born term in equation 7.43 is reweighted to the NLO result, as is done for the POWHEG method in equation 7.35. The Sudakov form factors must take the form of the POWHEG method, as shown in in equation 7.37, and as a result the evolution kernel in 7.43 must also take this form. In MENLOPS this NLO correction is only conducted for the initial Born process.

## 7.3 Hadronisation in SHERPA

Hadronisation is a significant problem for modelling in Monte Carlos as the perturbative components, the partons (quarks and gluons), must become confined within hadrons; since this process must occur in the non-perturbative regime of QCD where the theoretical methods for QCD described in this thesis are not valid, and alternative descriptions must be used. For the description of hadronisation in most Monte Carlo simulations, some sort of phenomenologically motivated model is used. Hadronisation within SHERPA employs a modified form of the cluster model of hadronisation [66] and [67], which is described in [68]. Cluster models of hadronisation are essentially based on the notion of pre-confinement of partons produced from parton showers. Preconfinement is simply the result that the partonic products of the shower can be arranged into colour singlet clusters and thus pre-hadronisation colour singlet objects exist. These colour singlet clusters are therefore the basic objects which will be hadronised.

This idea of preconfinement is best demonstrated in the large colour,  $N_c$ , limit; in this limit the leading colour approximation can be used (leading order in  $\frac{1}{N_c}$ ) whereby the colour structure of a gluon can simply be represented by a colour-anti colour line. During a parton shower the flow of colour can therefore be tracked and colour lines used to determine the colour singlet clusters. The use of these cluster models is interfaced with the parton shower; when the shower evolution reaches below the hadronisation scale, which is usually around 1 GeV, the shower will stop and the partons will be clustered into colour singlets with colour partners.

In practice this means that an enforced splitting into a quark-anti quark pair occurs for all gluons. These colour singlet objects are taken as the proto-hadrons, and the model decays these objects into various hadron species. Usually this decay process occurs by considering these clustered objects to be excited mesonic states; in the simplest employment of the cluster model these simply become the observed hadron species by selecting random two body decays that are allowed by kinematics and flavour.

# Chapter 8

## Photon Induced Processes

The contribution of photon induced processes to production channels, such as Drell-Yan, at the LHC is the emphasis of the second part of this thesis. As such this chapter will present the two contributions to these photon induced process, which are the photon component of the PDFs and Weizsacker-Williams distributions. In both cases the rationale behind these contributions is discussed, and the expressions used to calculate their components to the photon induced cross sections are explicitly given.

### 8.1 Photon PDFs

The photon component of the parton distribution function, will in this section, be motivated and introduced with a view to the use of these objects in later chapters. Some overview of the calculation of the initial distribution functions for photons is given, but this is not pursued in detail. A brief consideration will also be given to QED corrections to the parton shower formalisms which are also included in simulations described in this thesis.

The photonic contribution of a parton distribution function is a key part of the simulation of the photon induced processes. At present there exist two significant PDF sets which include photonic PDFs; the standard MRST2004QED [46] and the more recent set NNPDF2.3QED [47], both of these sets can be obtained from the

LHAPDF [82] package.

The motivation for a photon component of the parton distribution functions arises from considering the QED corrections to the DGLAP evolution kernels; essentially as it is possible for quarks in a hadron to branch photons such a contribution must exist. It is therefore possible to write a modified DGLAP evolution kernel for the evolution of PDFs to include QED splitting effects

$$\mu^2 \frac{\partial f_{a_i}(\eta, \mu^2)}{\partial \mu^2} = \sum_j \int_{\eta}^1 \frac{dy}{y} \left[ \frac{\alpha_s}{2\pi} P_{a_i a_j} \left( \frac{\eta}{y} \right) f_{a_j}(y, \mu^2) + \frac{\alpha}{2\pi} P_{a_i a_j}^{\text{QED}} \left( \frac{\eta}{y} \right) e_{a_j}^2 f_{a_j}(y, \mu^2) \right] \quad (8.1)$$

Where  $e_{a_j}$  is the fractional electric charge of the partonic component, and use is made of the QED equivalent of the Altarelli-Parisi splitting functions, which are listed below.

$$P_{\gamma q}^{\text{QED}}(z) = \left( \frac{1+z^2}{1-z^2} \right) \quad (8.2)$$

$$P_{qq}^{\text{QED}}(z) = \left( \frac{1+(1-z)^2}{z} \right) \quad (8.3)$$

$$P_{\gamma\gamma}^{\text{QED}}(z) = -\frac{2}{3} \sum_i e_i^2 \delta(1-x) \quad (8.4)$$

$$P_{q\gamma}^{\text{QED}}(z) = (z^2 + (1-z)^2) \quad (8.5)$$

As can be seen these are similar to their QCD equivalents, bar some constant factor, with the exception of the  $P_{\gamma\gamma}^{\text{QED}}$  splitting function which, as there are no direct photon-photon couplings in QED, only receives corrections from virtual terms and as a result is proportional to  $\delta(1-x)$ . It can be seen that such an inclusion of QED effects of, particularly the quark to photon splitting, naturally leads to a photon component of the PDF. The set of evolution equations, implicitly defined in the above expression, now includes an evolution kernel for a photon distribution, which can be written out explicitly to be

$$\mu^2 \frac{\partial f_{\gamma}(\eta, \mu^2)}{\partial \mu^2} = \frac{\alpha}{2\pi} \sum_j \int_{\eta}^1 \frac{dy}{y} P_{\gamma a_j}^{\text{QED}} \left( \frac{\eta}{y} \right) e_{a_j}^2 f_{a_j}(y, \mu^2) \quad (8.6)$$

This expression confirms that a photon component of a PDF set, if QED effects are included, must in principle be included, however determining an initial distribution

function for this component requires additional input.

The starting photon distribution functions in the MRST2004QED PDF set [46] are determined by considering the radiation of photons off quarks in the hadron. This set uses the assumption that this effect is dominant in the high  $x$  region, and this component is therefore determined from considering only valence quarks. The photon distribution at the initial scale,  $Q_0^2$  is thus determined from the one photon emissions off the valence quark; if the (collinear) leading logarithmic components of this emission are considered then the photon distributions can be written in terms of the valence quark distributions to be, for a proton

$$f_\gamma(x, Q_0^2) = \frac{\alpha}{2\pi} \int_x^1 \frac{dy}{y} P_{\gamma q}^{\text{QED}} \left( \frac{\eta}{y} \right) \left[ \frac{4}{9} \log \left( \frac{Q_0^2}{m_u^2} \right) u_0(y) + \frac{1}{9} \log \left( \frac{Q_0^2}{m_u^2} \right) d_0(y) \right] \quad (8.7)$$

Note that from [46] that  $u_0(x)$  and  $d_0(x)$  are in fact 'valence-like' distributions and are in fact determined from the valence distributions.

The more recent photon PDF set of NNPD2.3QED [47] adopts a more conventional approach to determining initial photonic distribution function, in that it is more reminiscent of techniques to determine such contributions for quarks and gluons. This is accomplished, essentially, by matching measured data for a process, for example deep inelastic scattering, to distribution function, which is convoluted with the relevant partonic cross section; for the photon PDFs QED effects must be included in this process.

The computation of hadronic cross section, utilizing the photon PDFs proceeds using the factorisation theorem as has been discussed in chapter one for strongly interacting partons; the computation of a photon induced process from hadronic collisions can therefore be computed from

$$\sigma_{\text{Hadronic}} = \int_0^1 d\eta_1 \int_0^1 d\eta_2 f_\gamma^{H1}(\eta_1) f_\gamma^{H2}(\eta_2) \hat{\sigma}_{\gamma\gamma \rightarrow X}(\eta_1 P_1, \eta_2 P_2) \quad (8.8)$$

which is simply the usual factorisation formula with the photon included as a parton. It should be noted that the use of photon PDFs is not exclusive to purely photon

induced process; for example a process  $\gamma q \rightarrow X$  is perfectly calculable, and would simply be given by 8.9.

$$\sigma_{\text{Hadronic}} = \int_0^1 d\eta_1 \int_0^1 d\eta_2 f_\gamma^{H1}(\eta_1) f_q^{H2}(\eta_2) \hat{\sigma}_{\gamma q \rightarrow X}(\eta_1 P_1, \eta_2 P_2) \quad (8.9)$$

However such contributions are not considered in this work, for results contributing Drell Yan or W pair production processes. Partonic processes of this form would constitute part of the NLO EW corrections to either the photon induced or partonic induced processes, which are not considered for this thesis.

### 8.1.1 QED Corrections to Parton Showering

The inclusion of photon PDFs in the simulation setup is supplemented here by the inclusion of QED corrections to the parton shower formalism; a review of parton showers is presented in chapter one of this thesis, and will not be repeated here. The modification of the PDF evolution kernel to include QED effects is described above and forces the inclusion of photon PDFs. It is noted however that the same physics is used to describe a parton shower, and therefore inclusion of QED effects in parton showers can in principle be included by supplementing the QCD splitting kernels with QED ones. For DGLAP evolution the QED splitting functions are described in the above section, and for parton showers based on DGLAP evolution the incorporation of QED splitting in showers simply amounts to the inclusions of these splitting terms in the Sudakov form factors, and in the branching terms where appropriate splittings occur in the shower [83]. The inclusion of the QED effects therefore modifies the Sudakov form factor to include the following term:

$$\Delta^{\text{QED}}(Q, Q') = \exp \left[ - \int_{Q^2}^{Q'^2} \frac{dq'^2}{q'^2} \int dz \frac{\alpha_s}{2\pi} P_{ij}^{\text{QED}}(z) \right] \quad (8.10)$$

However the parton shower algorithm made use of within SHERPA utilizes Catani Seymour dipoles, in their spin averaged form, as the evolution kernels, as opposed to the Altarelli-Parisi splitting functions of DGLAP. To include the QED emissions in a parton shower formulated in this fashion, the QED dipole splitting must be included

in the manner shown above for the Altarelli-Parisi QED splitting functions. The Sudakov form factor is then defined as

$$\Delta^{\text{QED}}(Q, Q') = \exp \left[ - \int_{Q^2}^{Q'^2} d\Phi_1^{ij,k} \mathcal{K}_{ijk}^{\text{QED}}(\Phi_1^{ij,k}) \right] \quad (8.11)$$

where  $\mathcal{K}_{ijk}^{\text{QED}}(\Phi_1^{ij,k})$  are the Catani Seymour spin-averaged dipole splitting functions.

## 8.2 Equivalent Photon Approximation

In the discussion in the previous section concerning the use of photon PDFs to simulate photon induced processes, which is of necessity in determining such corrections, however, this simply gives the inelastic component of the cross section. In the case of the similar QED corrections for elastic processes, this essentially involves electromagnetic fields of the protons interacting and causing particle production. The observation, first made by Fermi [84] and later developed by Weizsaecker and Williams [85] [86], that the electromagnetic field of a ultra-relativistic object can be effectively modelled as a spectrum of real photons is known as the effective photon approximation (EPA). The use of this approximation can be applied for both single and double photon cases; in the first case the approximate photonic interaction only comes from one of the initial state particles whilst the in later from both. In this thesis only the double photon case is relevant, and the former case will not be discussed although the interested reader is referred to [48]. For the double photon case, the equivalent photon approximation causes the complete cross section to factorise in a manner similar to that of the hadronic PDF cross section. It is essentially reduced to a convolution of the double photon cross section with the EPA distribution functions for both initial state particles, the photon distributions are therefore analogous to the PDFs and the photon cross section analogous to the partonic one; it is explicitly given below.

$$\sigma_{\text{EPA}} = \int_0^1 d\eta_1 \int_0^1 d\eta_2 f^{\text{EPA}}(\eta_1) f^{\text{EPA}}(\eta_2) \hat{\sigma}_{\gamma\gamma \rightarrow X}(\eta_1 P_1, \eta_2 P_2) \quad (8.12)$$

Where the photon spectra are described by  $f^{\text{EPA}}(\eta_1)$ .

These spectra were initially calculated in a semi-classical limit, and later this was extended to using Feynman diagrammatic methods. In this formalism the EPA distribution for point-like particles such as electrons can be calculated within the context of the approximation. However for bound states such as protons the calculation of this distribution must be supplemented with empirical modelling of the proton structure. The fitting for this distribution employed within SHERPA for protons is shown below and is based on the formalism given in [48], .

The EPA spectrum function,  $f_{\text{EPA}}(x)$  is then given for a proton by

$$f_{\text{EPA}}(x) = \frac{\alpha}{\pi} \frac{1-x}{x} \left[ \varphi \left( \frac{q_{\text{max}}^2}{q_0^2} \right) - \varphi \left( \frac{q_{\text{min}}^2}{q_0^2} \right) \right], \quad (8.13)$$

wherein  $x = E_\gamma/E_{\text{hadron}}$ ,  $q_{\text{max}}^2 = 2 \text{ GeV}^2$ , and  $q_{\text{min}}^2(x) = (m_p^2 x^2 + p_{\perp,\text{min}}^2)/(1-x)$ . The function  $\phi$  is given by

$$\begin{aligned} \varphi(z) = \frac{(1-b)y}{4z(1+z)^3} + (1+ay) \left[ -\log \left( 1 + \frac{1}{z} \right) + \sum_{k=1}^3 \frac{1}{k(1+z)^k} \right] \\ + c \left( 1 + \frac{y}{4} \right) \left[ \log \frac{1+z-b}{1+z} + \sum_{k=1}^3 \frac{b^k}{k(1+z)^k} \right], \end{aligned} \quad (8.14)$$

with  $y = x^2/(1-x)$  and  $a = \frac{1}{4}(1 + \mu_p^2) + 4\frac{m_p^2}{q_0^2} \approx 7.16$ ,  $b = 1 - \frac{4m_p^2}{q_0^2} \approx -3.96$  and  $c = \frac{\mu_p^2 - 1}{b^4} \approx 0.028$ .  $m_p$  is the proton mass and  $\mu_p^2 \approx 7.78$ ,  $q_0^2 \approx 0.71 \text{ GeV}^2$  [48].

It is this spectrum for the proton that is implemented within SHERPA and is used for the EPA component of photon induced processes in all simulations presented in later chapters.

# Chapter 9

## Photon Induced Processes Results

The addition of photon induced channels to the simulation of certain processes at the LHC is the subject of the second part of this thesis; in previous chapters the motivation for, and calculation of these channels has been described. In this chapter results of simulations which include these channels, in addition to standard QCD components, are presented and discussed; where possible they are compared to data from ATLAS or CMS. The processes used to demonstrate the contribution of photon channels are, as has been discussed, the production of lepton pairs and the production of  $W$  pairs with leptonic decay products. The motivation for the choice of these processes is, as has been discussed already, their use in determining bounds on new physics; in the case of the lepton-pairs bounds on heavy mass resonances and for the case of the  $W$  pairs its status as an important background to a key Higgs production channel. For both of these channels a description of the setup of the simulation will be given, followed by a presentation of this simulation compared with relevant data from ATLAS or CMS; additionally, for both processes results will be presented which indicate the effect of the photon channels on the emission of additional jets. For the  $W$  pair process the simulation is conducted again for 14 TeV collisions, in anticipation of run two of LHC analyses.

## 9.1 Lepton-pair production

The production of lepton pairs is given as the first example for the simulation of photonic processes. The set up for this simulation incorporates a baseline Drell-Yan production at NLO accuracy in QCD, which is obtained using the SHERPA implementation of the MC@NLO formalism. This is supplemented by the addition of the di-photon production of lepton pairs, which occurs in two channels. The first of these is the photonic component of proton PDFs, which is incorporated into the PDF sets MRSTQED2004 [46] and NNPDF2.3QED [47]. The photonic channel here is simulated separately for both sets, resulting in separate photonic contributions which are given for all results in this section. This is justified by the possibly large errors associated with photon PDFs. The second originates from the photons emitted, quasi-elastically, from protons. This channel is simulated with the Equivalent Photon Approximation of Weizsaecker and Williams [48], which is discussed in chapter 8, and which has been implemented within SHERPA. Both of these channels utilize the matrix element for photo-production of leptons,  $\gamma\gamma \rightarrow ll$ , which is calculated within SHERPA at leading order.

### 9.1.1 Inclusive lepton pair production

For the case of Lepton pair production, the simulational set up in SHERPA, described above, is utilized to compare against recent precision Drell-Yan measurements by ATLAS [4] and CMS [2] and [3]. The details of the analysis framework implemented for these results are described, for both ATLAS and CMS, in appendix A. For each experimental set up the relevant analysis framework is implemented in a RIVET analysis [87], which is interfaced with SHERPA to produce a simulation to compare with the relevant data. The theoretical errors on the simulation data have as the dominant contribution the factorisation and renormalisation scale errors (there are additional small contributions from the Monte Carlo integration of the processes); these are computed by the correlated variation of the factorisation and renormalisation scales between  $\mu/2$  and  $2\mu$ , where  $\mu$  is the central value of the scale used.

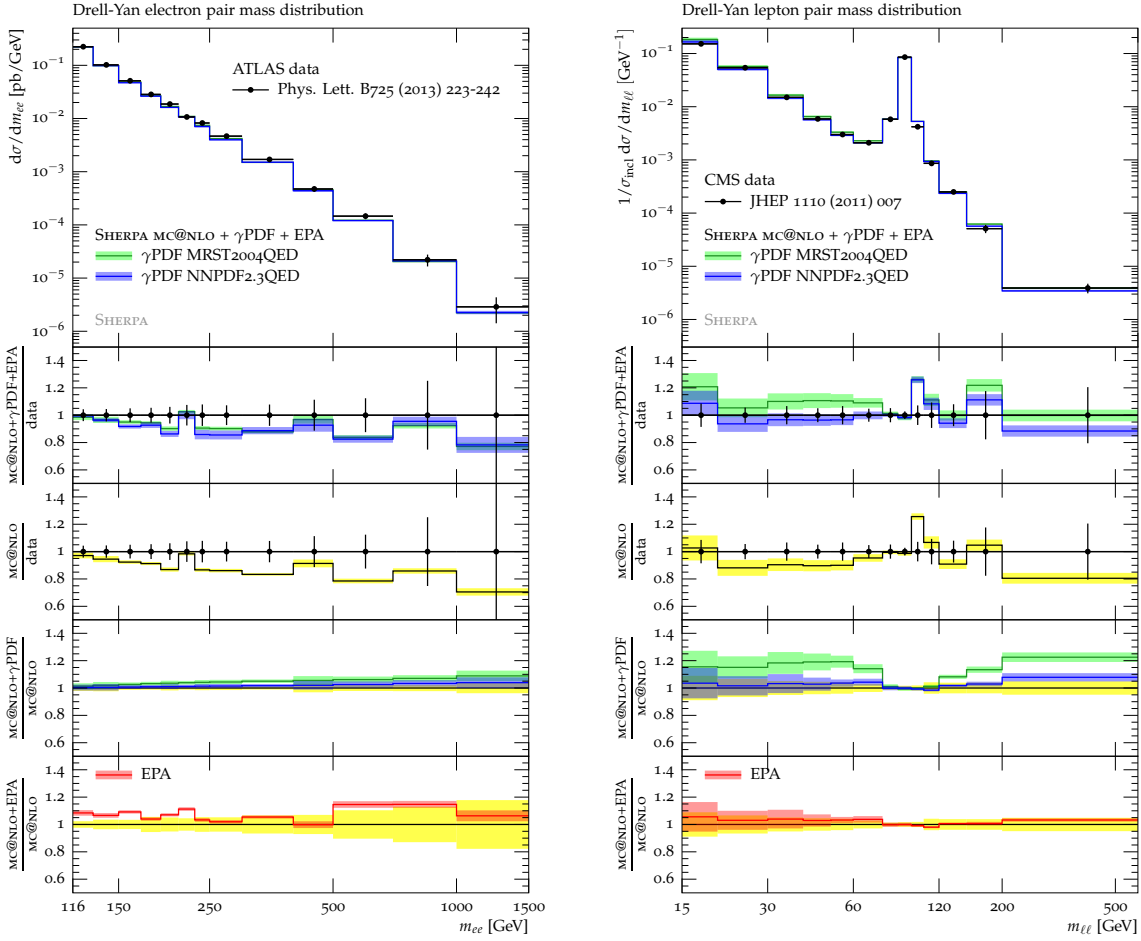


Figure 9.1: Invariant lepton-pair mass spectra as measured by ATLAS [4] (left, and for  $ee$  final states) and by CMS [2] (right, and for lepton-lepton final states). The experimental data is compared with SHERPA simulations, starting from a baseline QCD sample simulated with the MC@NLO implementation in SHERPA (black); the QED PDF (green and blue) and EPA (red) contributions are successively added.

These analyses are presented in figures 9.1 and 9.2, and all show lepton pair invariant mass distributions based on Drell-Yan data and the results of the SHERPA simulations. Figure 9.1 shows the invariant mass distribution of electrons in the high mass tail (116-1500 GeV) based on the ATLAS analysis described in [4] and the invariant mass of lepton pairs in the lower mass region (15-600 GeV) based on the CMS analysis [2]. Figure 9.2 shows the invariant mass distributions for electron and

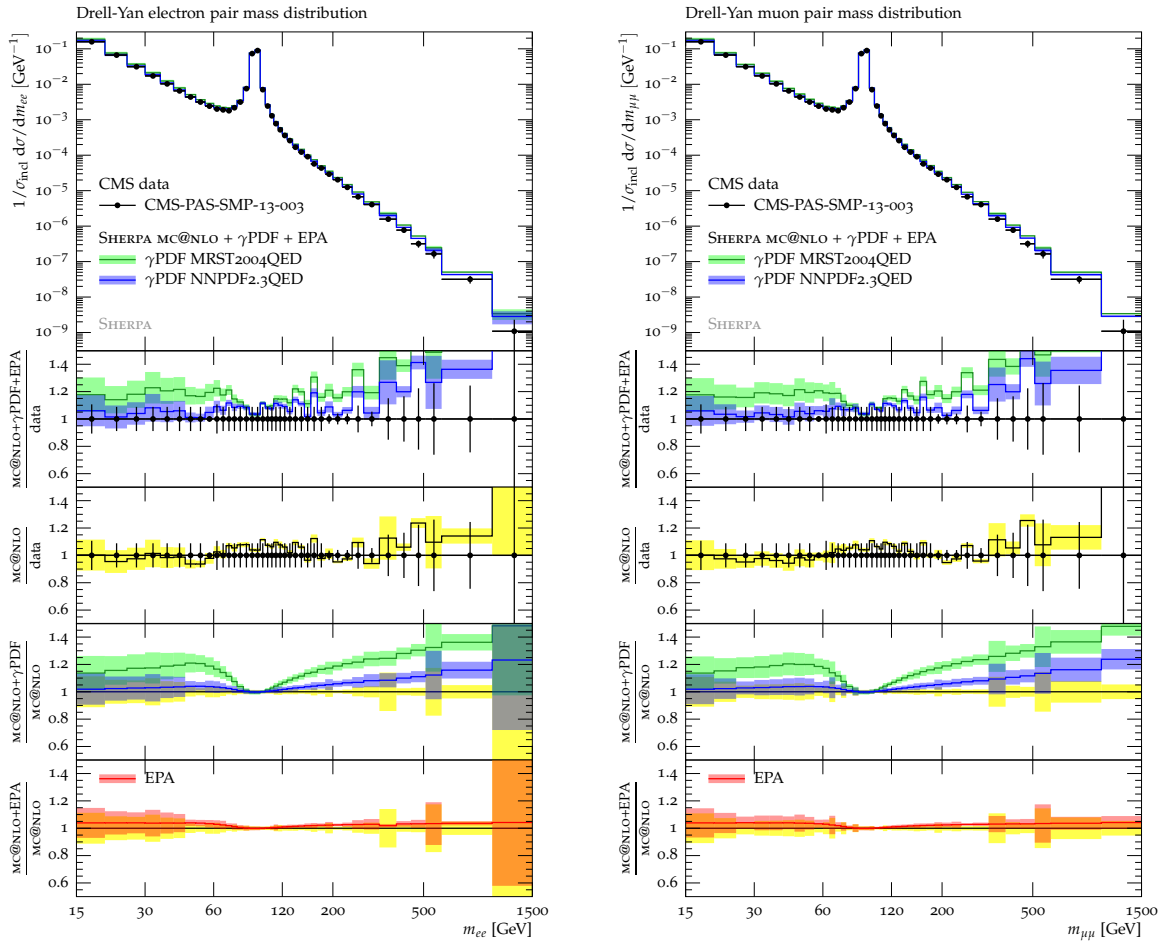


Figure 9.2: Invariant lepton-pair mass spectra as measured by CMS [3] (left for  $ee$ , right for  $\mu\mu$  final states). The experimental data is compared with SHERPA simulations, starting from a baseline QCD sample simulated with the MC@NLO implementation in SHERPA (black); the QED PDF (green and blue) and EPA (red) contributions are successively added.

muon pairs over the combination of the mass regions shown in the previous figure (15-1500 GeV), based on the analysis described in [2]. For the CMS analyses in this section, based on results from [2] and [3], the differential distributions are normalised to the cross section in the  $z$  mass region (defined to be 60-120 GeV). Analyses based on ATLAS results simply give the differential cross section. It is noted, from these figures, that the shapes of these distributions are reasonably described by the QCD baseline contributions; the ATLAS results appear to be undershot by the baseline

by about 10%, whilst such an occurrence is not seen for the CMS results. Here it is worth stressing that normalisation of the CMS processes would remove such an effect, and therefore explain why it occurs only for the ATLAS analysis.

Regarding the photon channels, a number of points can be clearly discerned from these figures. It is apparent that the photon channels can contribute sizeably to this process, and are particularly significant in the high  $m_{ll}$  tail ( $\geq 500$  GeV); for CMS analyses these corrections can be as large as 10-20% whilst for ATLAS they are slightly smaller, though still significant, and of the order of 5-10%. A cautionary note will be struck, given that both theoretical and experimental errors, in the high  $m_{ll}$  region are large ( $\geq 10\%$ ) for these results; however, the enhancement due to this channel is still reasonably significant by this measure.

Additionally it is apparent that there is a clear difference in the size of the photon channel, in relation to the photon PDF set used; again this is an effect more discernible in the high  $m_{ll}$  region. The photon channel for which the MRST photon PDF set is used is visibly enhanced with respect to this channel computed using the NNPDF set; this is particularly clear for the CMS comparisons shown in figure 9.2, although this is less clear for the higher mass region shown in 9.1 for the ATLAS analysis; although the MRST set is still relatively enhanced with respect to the NNPDF set. It is possible that this may be the result of phase space cuts applied in the ATLAS analysis [4], which do not occur for the CMS analyses; which are notionally unfolded for the full phase space. It is also observed that photon channels which utilize the NNPDF set remain in reasonably good agreement with data; however the same channel simulated using the MRST set often does not, and can be sizeably enhanced with respect to the data. This however is not too surprising as the former originates from an actual fit to LHC data, while the latter is an older set which relies on a relatively crude parametrisation to obtain photon distributions; this parametrisation is summarised in chapter 8. It is also noted that the affect of photon channel contributions appear to be dominated by the photon PDF components, which contribute significantly to the process. The component based on the equivalent photon approximation, when compared separately to the QCD baseline, shows relatively lit-

the enhancement over the  $m_{ll}$  mass spectrum none of which is significant with respect to errors.

### 9.1.2 Jet activity

For some searches for new physics, the production of lepton pairs in association with jets can be an important background. In this vein, the setup utilized in the previous section can be modified to consider the effect of photon induced processes on jet activity in lepton pair production. In this task the setup is modified slightly and MC@NLO setup is replaced by using MENLOPS for the QCD baseline process, otherwise all aspects of the simulation are unchanged.

In figure 9.3 the average number of jets  $\langle N_{\text{jet}} \rangle$  is depicted as a function of the invariant mass of the lepton pair. Jets in this plot are defined by the anti- $k_T$  algorithm [24] with  $R = 0.4$  and  $p_{\perp}^{(\text{jet})} \geq 20$  GeV; a full analysis framework used for this simulation is provided in appendix A. Again the theoretical errors on the simulation have, as the dominant contribution, the factorisation and renormalisation scale errors; and as before these are computed by the correlated variation of the factorisation and renormalisation scales.

Generally, including photon induced processes reduces the number of jets by up to 30% for channels using the NNPDF set and up to 35% for the MRST set. Again it is seen that this affect is dominant in the high  $m_{ll}$  tail region but, as expected, it does not influence the number of jets around the  $Z$ -pole, for  $m_{\ell\ell} \approx M_Z$ , since there the QCD baseline entirely dominates the overall production cross section. The effect of the EPA induced contribution, which appears to dominate the photon channel, seems large in that it reduces the average jet multiplicity by between 10-20%, and again has the largest effect in the high  $m_{ll}$  region. It is likely that such a large EPA component is the result of forward lepton production, and as such unobservable in colliders, a region where the EPA cross section is large.

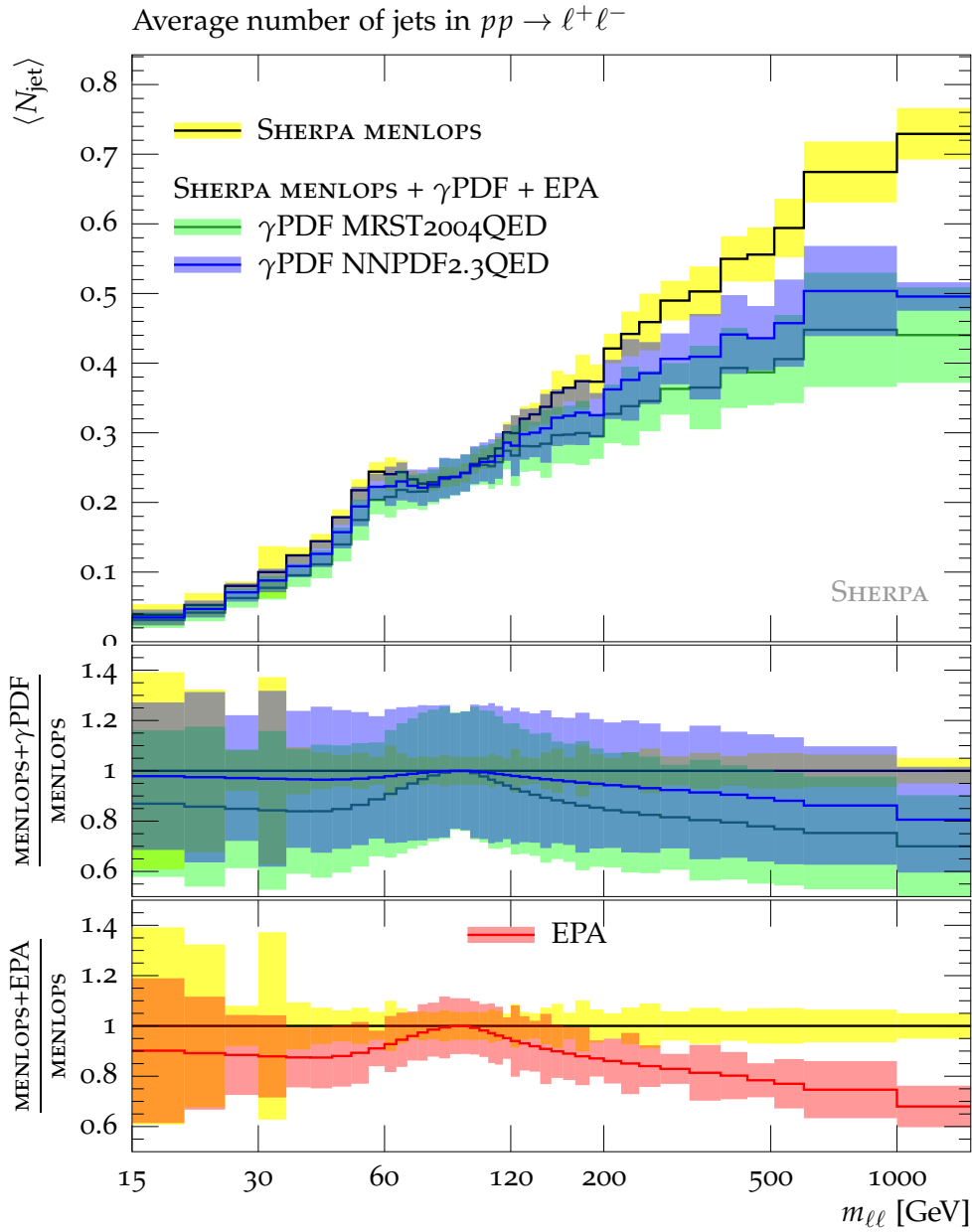


Figure 9.3: Average number of jets emitted per mass bin for Drell-Yan Process. The SHERPA simulations, starting from a baseline QCD sample simulated with the MENLOPS implementation in SHERPA (black); the QED PDF (green and blue) and EPA (red) contributions are successively added.

## 9.2 $W$ -pair production

The process of  $WW$  production at the LHC will be given as another test of the contribution of photon-induced channels. The set up for this simulation incorporates a

baseline  $WW$  production at NLO accuracy in QCD; which is computed using the MC@NLO formalism. The virtual contribution to the  $q\bar{q} \rightarrow WW$  process is calculated in MCFM [88], and interfaced with SHERPA for the calculation of this process. The main baseline process is supplemented by the inclusion of the gluon gluon production channel, which is the result of the effective gluon gluon to  $WW$  vertex, and is included as this channel can become enhanced due to the large gluon PDF. This is then supplemented by the addition of the photon-photon production of  $W$  pairs, which again occurs in two channels. The first of these is the photonic contribution to the PDFs, which is incorporated into the PDF sets MRSTQED2004 [46] and NNPDF2.3QED [47]; the photonic channel is simulated separately for both sets as for the lepton pair production analysis. The second is the result of quasi-elastic emissions of photons from protons, described by the Equivalent Photon Approximation of Weizsaecker and Williams [48]. Both of these channels utilize the  $\gamma\gamma \rightarrow WW$  matrix element, which is calculated within SHERPA at leading order.

For this analysis, the  $W$ -pairs simulated are decayed into lepton-neutrino pairs only; which is the choice employed by most experimental analyses of this process, such as [1]. The simulational set up produces on-shell  $W$  pairs, which are then decayed to produce the leptons used in the analysis.

### 9.2.1 ATLAS analysis

The analysis of  $WW$  production in this section is based on data from the ATLAS experiment described in [1]. As for the case of lepton pair production, discussed in the previous section, the SHERPA simulational set up, including the photon channels, is utilized to give a comparison with these results. The experimental analysis of  $WW$  production in ATLAS given in [1], is based on the measurements of electrons and muons from the leptonic decay channels of the  $W$ . The analyses presented in this section will focus on distributions over observables of one or both of the detected leptons, from the decays of the  $W$  pairs, such as the lepton pair mass or the  $p_{\perp}$  of the lepton pair. The kinematic cuts on this analysis, which are summarized in appendix A, are thus conducted on such variables; as with previous analyses these

are implemented into a RIVET analysis [87], which is then interfaced with SHERPA to produce a simulation of the experimental framework. As for the Drell-Yan processes the dominant source of theoretical error is the factorisation and renormalisation scale errors (there are additional small contributions from the Monte Carlo integration of the processes); these are computed by the standard of variation of the factorisation and renormalisation scales between  $\mu/2$  and  $2\mu$ , where  $\mu$  is the central value of the scale used.

Figure 9.4 shows the normalised leading lepton  $p_{\perp}$  distribution, based upon data unfolded in the ATLAS analysis [1], restricted to the fiducial region as described in appendix one. In addition to this, figure 9.5 shows data from the same fiducial region; however this data is not unfolded. To give a meaningful comparison, the background channels described in [1] are removed, and the SHERPA analysis is subject to global acceptance factors for each of the decay channels, which are again described in [1]. The fit to the shape of these distributions, provided by the QCD baseline, is not unreasonable; however, it does deviate from the data slightly. This is best illustrated in the normalised distribution in figure 9.4 where the vague shape of the distribution appears to agree with data, whilst the simulation disagrees with data for several bins. It is also noted that this baseline undershoots the data by a significant margin of around 20% for the event distributions shown in figure 9.5, an effect that would not appear in the normalised distribution of figure 9.4. This may be the result of this data having only crudely been compensated for detector effects; however, a similar affect was found by [1], which used a similar QCD prediction setup to the baseline simulation conducted for this analysis.

In contrast to the lepton pair production process presented earlier in this chapter, the effect of the photon channels appears less discernible in figures 9.4 and 9.5. The photon channels do not appear to deviate with any significance from the QCD baseline process; whilst a modest effect appears in the tail of the leading lepton  $p_{\perp}$  spectrum in figure 9.5, this is not significant compared to the size of the errors (which are large in the tail region). The contrast between the photon channels, computed using the MRST and NNPDF photon PDF sets, not appear to be discernible, based on these

results; however, this most likely reflects that the photon induced channels are not particularly significant for this process.

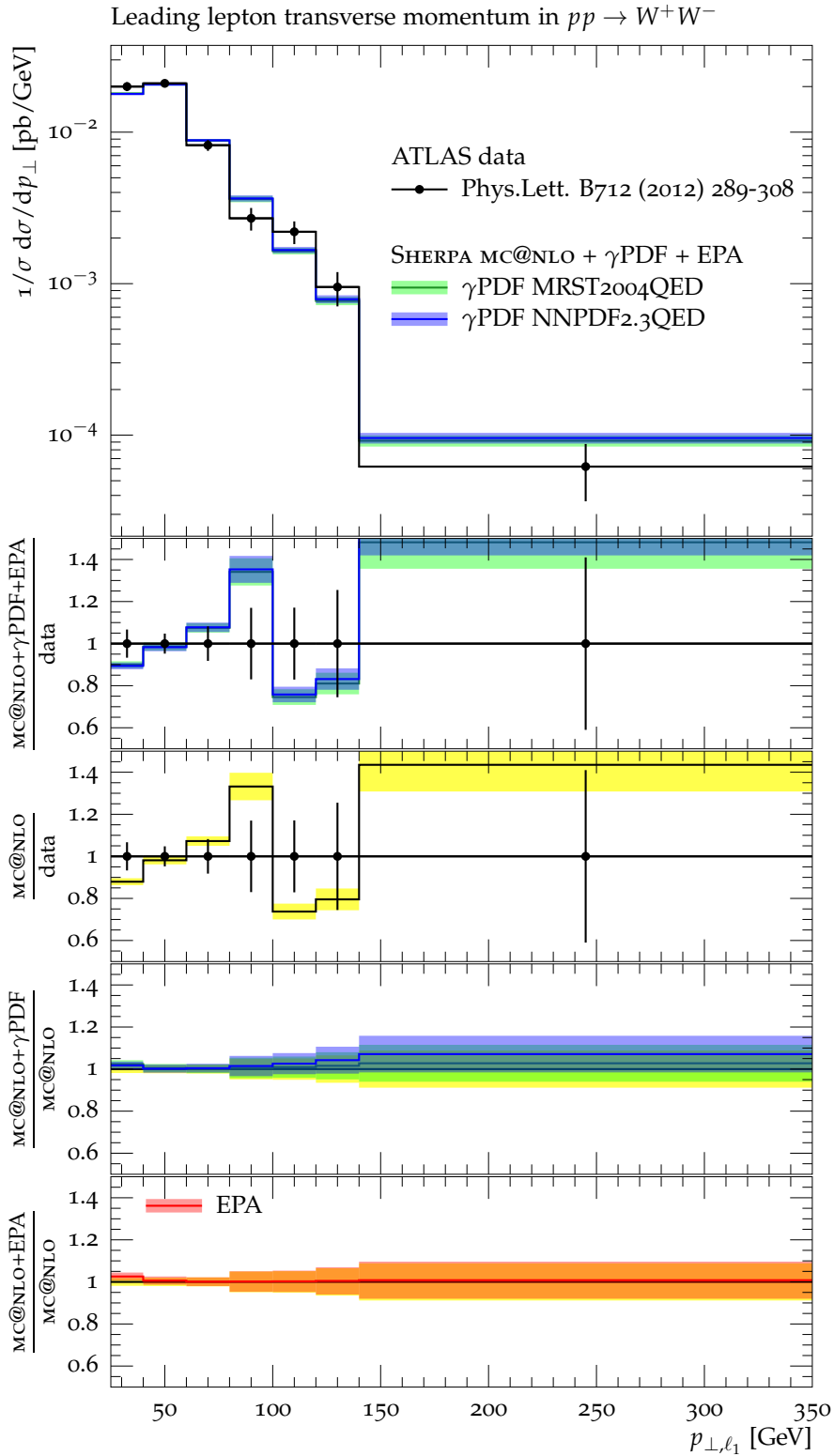


Figure 9.4: The normalised fiducial differential  $WW$  cross section as a distribution in leading lepton  $p_{\perp}$  as measured by [5]. The experimental data is compared with SHERPA simulations, starting from a baseline QCD sample simulated with the MC@NLO implementation in SHERPA (black); the QED PDF (green and blue) and EPA (red) contributions are successively added.

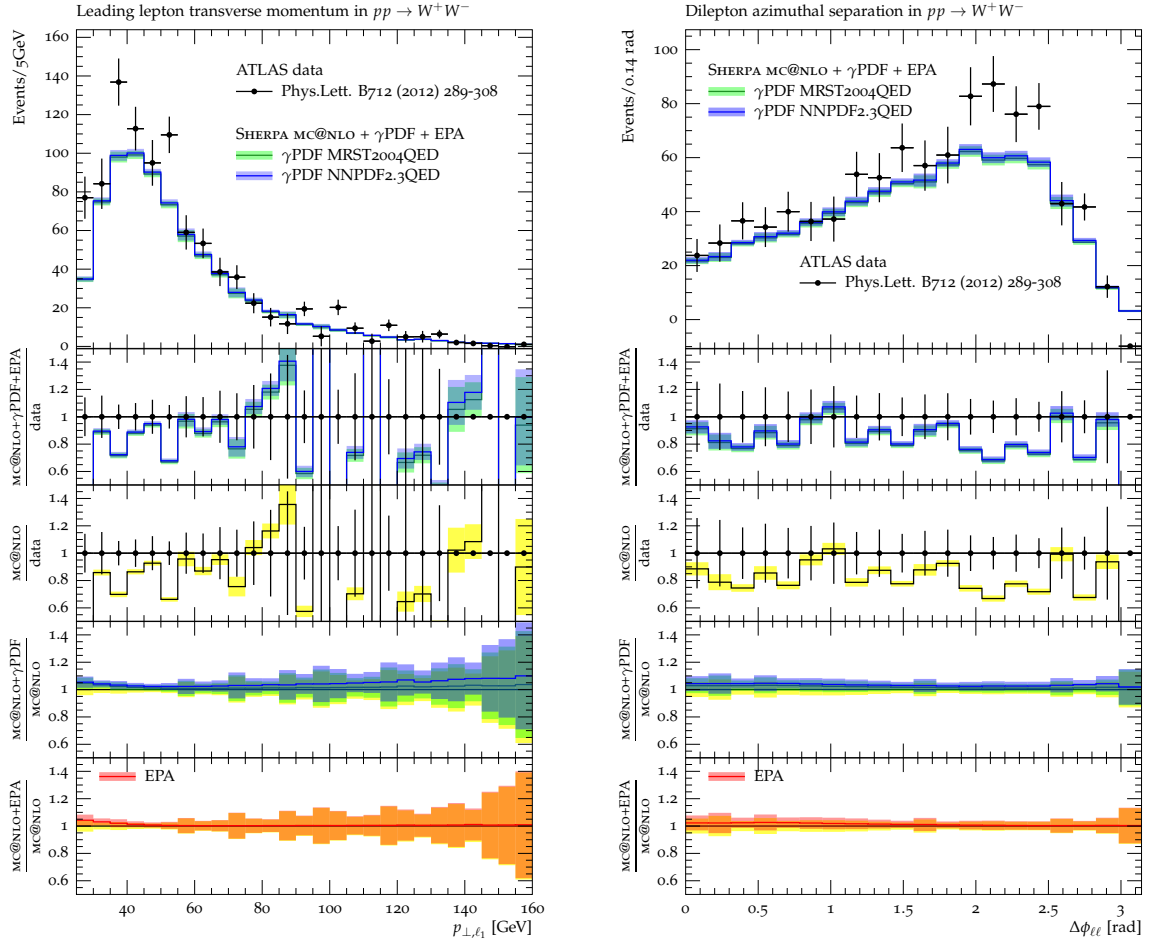


Figure 9.5: Distribution of  $WW$  production events for leading lepton transverse momentum and the azimuthal decorrelation of the lepton pair as measured by [5] (left for  $p_{\perp}$ , right for  $\phi_{ll}$ ). The experimental data is compared with SHERPA simulations, starting from a baseline QCD sample simulated with the MC@NLO implementation in SHERPA (black); the QED PDF (green and blue) and EPA (red) contributions are successively added.

### 9.2.2 High-mass tail

The previous section details the set up and simulation of the  $WW$  production analysis of [1]; in this section, in anticipation of LHC run two energies, the same analysis framework is used for simulation 14 TeV collisions. For this analysis, the simulation will continue to use the phase space cuts identified with the analysis in [1]; which are again implemented via a RIVET analysis, details of which continue to be described in appendix A. It must be stated that this section will present no comparison with data, simply the results of the simulation setup previously described, in an attempt to discern the effect of photon induced channels, if any, on this process. The process therefore is identical to the previous section, namely production of  $WW$  events which then decay leptonically.

Figure 9.6 shows the differential distributions of the lepton pair  $p_{\perp}$  and mass as described by the SHERPA simulation; both include a large tail region, extended up to 1 TeV for the mass and 200 GeV for the  $p_{\perp}$ . except that it is simulated at 14 TeV. Again the dominant source of error is the scale variation error, which is estimated by the correlated variation of the relevant scales in the same fashion as described for previous cases.

Regarding the photon channels in this section, it is seen that they do not appear to be particularly significant relative to the QCD baseline; as was the case for the 7 TeV results. For the lepton pair  $p_{\perp}$  and mass distributions, shown in figure 9.6, a more extended tail region is shown compared to 7 TeV results; the photon channels appear more significant in these tail regions, giving 5% corrections to the lepton mass distribution  $\geq 500$  GeV and similar corrections to the lepton  $p_{\perp}$  spectrum above  $\geq 150$  GeV. However it is noted that such corrections are completely dwarfed by the error, which is scale dominated, for the tail regions. As such, no enhancement of the photon channel of significance is observed. The contrast between the photon channels computed using the MRST and NNPDF photon PDF sets do not appear to be discernibly different, based on these results. This is also the case for the same process at 7 TeV, and there as here this probably reflects that photon induced channels are not particularly significant for this process. Even in the high lepton

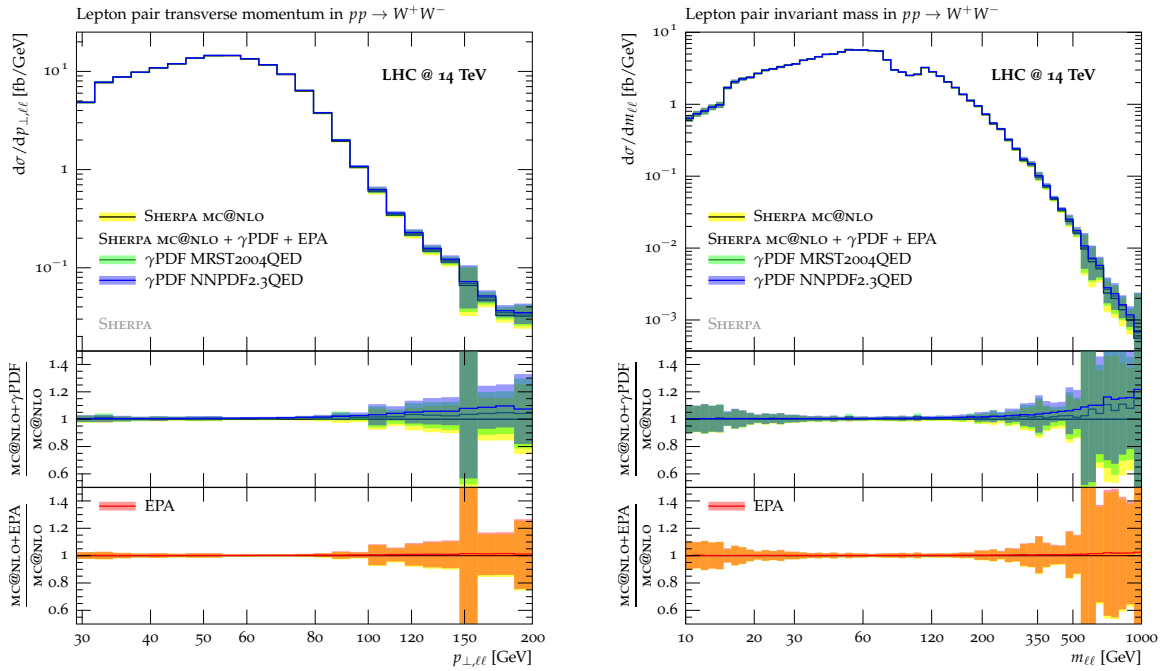


Figure 9.6: Differential cross section for  $WW$  production with respect to the transverse momentum (left) and invariant mass (right) of the lepton pair, simulated at 14 TeV with an analysis framework consistent with [5]. The SHERPA simulations, starting from a baseline QCD sample simulated with the MC@NLO implementation in SHERPA (black); the QED PDF (green and blue) and EPA (red) contributions are successively added.

mass and  $p_{\perp}$  tails where the photon channels do appear to be large, although still dominated by error, there is no significant difference in photon channels computed using the different sets.

### Jet Activity of $WW$ Processes

As with the case of the lepton pair production, the issue of how the photon channels influence the production of additional jets will be investigated for the  $W$  pair channel. For this case the ratio of the one to zero jet rates are simply plotted over the same distributions shown in figure 9.6; the effect of the photon induced channels on this result can be used, in a similar fashion to the analysis shown in figure 9.3, to describe the effect of these channels on jet activity.

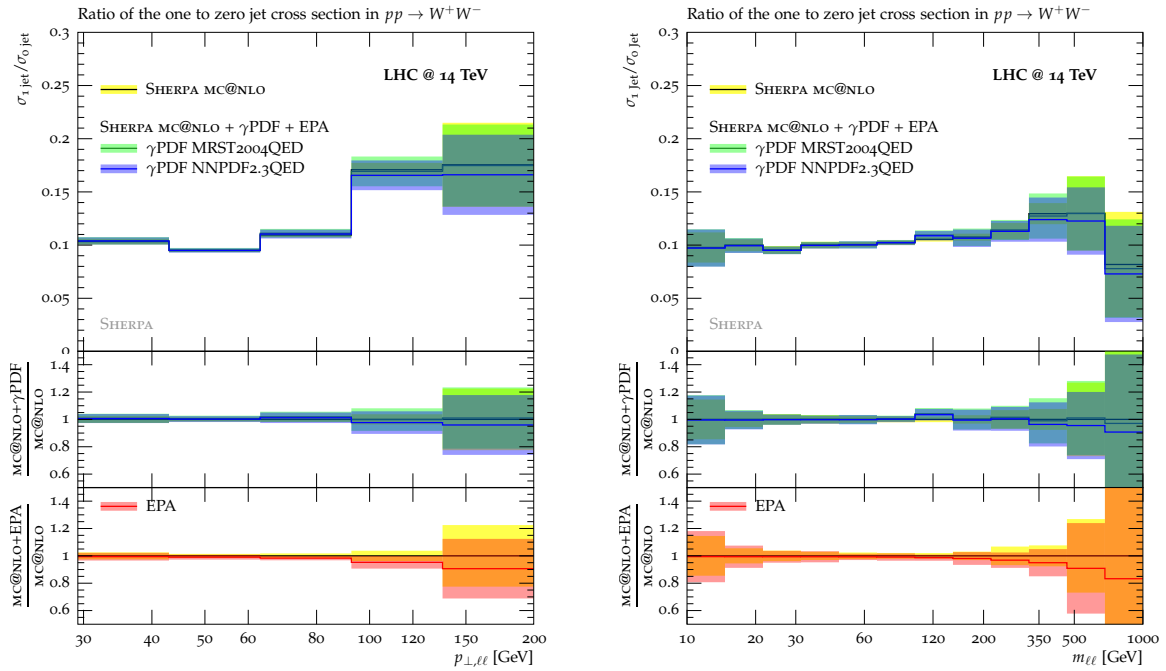


Figure 9.7: Ratio of 1-jet to 0-jet rates in  $WW$  production, shown as a distribution transverse momentum (left) and invariant mass (right) of the lepton pair and simulated at 14 TeV with an analysis framework consistent with [5]. The SHERPA simulations, starting from a baseline QCD sample simulated with the MC@NLO implementation in SHERPA (black); the QED PDF (green and blue) and EPA (red) contributions are successively added.

These analyses are shown in figure 9.7, whereby this ratio is shown for the lepton invariant mass and transverse mass distributions. Again the dominant contribution to the error is the result of scale variation, which is computed identically to all other cases. Given that the effect of photon channels on this process is, as has been discussed, not significant relative to the size of the errors, it is perhaps not surprising that the effect of these channels on the jet ratio is not particularly significant. It is noted however, that as with lepton mass and  $p_{\perp}$  distributions for this analysis, some sizable effects occur in the high mass and  $p_{\perp}$  tail regions; principally these are reductions of the jet ratio of about 5-10% in the tail region for the photon PDF channels, and of about 10% for the EPA channel. However it is noted these effects are dwarfed by large errors.

# Chapter 10

## Conclusions to Part II

In part II of this thesis a study has been presented on the effect of photon induced channels on two key processes, at the LHC, for the bounding of new physics; namely Drell-Yan production and  $W$  pair production. This was accomplished by the use of the Monte Carlo event generator SHERPA, for the simulation of both baseline and photon channel contributions.

The physics behind Monte Carlo event generators, such as SHERPA, is reviewed in chapter 7 and the various modeling techniques used in this study are discussed. Particular attention is paid to aspects of Monte Carlo's that are used directly in this work, and as such discussions are given on parton showering, in addition to combination of parton showering with both NLO calculations and matrix elements; the MC@NLO and CKKW-L formalisms are briefly discussed in this context. A motivation for, and discussion of, photon induced process is then presented in chapter 8. Such processes are composed of two channels; the first of these is the photon component of a PDF, which arises naturally from considering QED corrections to parton evolution kernels, and can in principle become quite large; the two photon PDF sets used in this thesis, MRSTQED2004 and NNPDF2.3QED are briefly described in this context. Additionally the quasi-elastic component of photon process, which arises from photons emitted from protons (which then remain intact for such events), is considered, this is modelled by the Equivalent Photon Approximation of Weizsacker and Williams; the EPA distributions implemented within SHERPA for

protons are explicitly given. In chapter 9 the results of these studies are presented for the production of lepton pairs and  $W$  pair production, in both cases the simulations are compared with data from ATLAS or CMS. For both of these processes the shape of the distributions from data is reasonably well-fitted by the QCD baseline simulation, for Drell-Yan the agreement is excellent whilst for the  $W$  pair process it is less so. The effect of photon induced channels is found to be quite sizeable for lepton pair production, particularly in the high  $m_{ll}$  region for this process, for photon channels computed using the MRST photon PDF set. This enhancement of the mass distribution leads to a disagreement with data from CMS; for the newer NNPDF set no such disagreement is observed. The effect of the photon channels is found to be not particularly significant for the  $W$  pair process; and even when this process was considered at LHC run two energies the photon induced channels do not produce a sizeable contribution, that is significant with respect to the size of the errors. For both processes, the effect of the photon channels is considered for the production of extra jets; for lepton pair production a sizeable reduction in the average jet multiplicity is found. This effect is dominated by the EPA component of the photon channel, a result that is most likely due to enhancement of the EPA cross section in forward region; while for  $WW$  production the effect of photon channels is once again found to be small.

It is concluded that for predictions concerning Drell-Yan processes, particularly discovery searches in the high lepton pair mass region, the inclusion of photon induced channels is recommended for high precision results; particularly the photon PDF component. It is further concluded that the more appropriate photon PDF set to use is the NNPDF set, which is the more recent and found to be in better agreement with data. For searches that are sensitive to extra jet emissions in this process, the inclusion of the EPA channel should also be included. For  $W$  pair production the photon induced channels are small, and therefore can for the most part be overlooked.

# Appendix A

## Details of the Experimental Analyses

The results presented in chapter 9 of this thesis compare simulations against certain experimental analyses. These analyses are subject to certain kinematic cuts and definitions of leptons and jets that were defined for the experimental results; to give a meaningful comparison to such results these constraints must be reproduced for the simulations. This is accomplished, for this thesis by the general Monte Carlo analysis software RIVET [87]. These constraints, as implemented within RIVET will be presented in this appendix for all analyses used in this thesis.

At this point it will be useful to introduce a definition. Throughout this appendix there will be references to radius cones, in both the context of lepton isolation criteria and jet constraints; these are defined, in this context, as the combined radius of pseudorapidity,  $\eta$  and azimuthal angle  $\phi$  expressed below.

$$\Delta R = \sqrt{(\Delta\eta)^2 + (\Delta\phi)^2} \tag{A.0.1}$$

### A.1 ATLAS $WW$ Analysis [1]

The results obtained by the ATLAS experiment for this section will detail the experimental cuts made for the ATLAS experiment analysis for  $W$  pair production events; these events are constrained to include only leptonic decay processes for the

$W$  bosons. This analysis is described in [1], and the analysis details necessary for the simulation and implemented in a RIVET analysis are described below.

The leptonic decay products of the muons are required to obey constraints on transverse momenta and pseudorapidity, which are summarised in table A.1.

Electron pseudorapidity	$ \eta  < 1.37$ or $1.52 <  \eta  < 2.47$
Muon pseudorapidity	$ \eta  < 2.4$
Lepton $p_{\perp}$ threshold	$p_{\perp} > 20$ GeV
Leading lepton $p_{\perp}$ threshold	$p_{\perp} > 30$ GeV

Table A.1: A summary of pseudorapidity and  $p_{\perp}$  cuts on leptons as described in ATLAS analysis [1]

The Leptons are also required to obey isolation criteria, for this analysis cuts are placed on the sum of all transverse energy and momentum within the cone of  $\Delta R < 0.3$  around proto-leptons, the thresholds are given in the table below.

Lepton isolation criteria for transverse energy	$\sum_{\Delta R < 0.3} E_{\perp} < 0.14 E_{\perp}^{\text{lepton}}$
Electron isolation criteria for transverse momentum	$\sum_{\Delta R < 0.3} p_{\perp} < 0.15 p_{\perp}^{\text{electron}}$
Muon isolation criteria for transverse momentum	$\sum_{\Delta R < 0.3} p_{\perp} < 0.13 p_{\perp}^{\text{muon}}$

Table A.2: Isolation criteria on leptons as described in ATLAS analysis [1]. All isolation criteria are taken within a cone of radius  $\Delta R < 0.3$

The jets in this analysis are defined with the anti- $k_T$  algorithm [24] with radius parameter  $R = 0.4$ . These anti- $k_T$  jets are, like the leptons, subject to kinematic cuts which are described in the table below, and which also gives the jet veto criteria. The jet veto criteria simply states the conditions a jet must meet in order to veto an event, and in this context is introduced into the experimental analysis to reduce backgrounds.

Jets	Anti- $k_T$ , $R = 0.4$ , $p_\perp > 20$ GeV, $ \eta  < 4.9$
Jet Veto	$p_\perp > 25$ GeV and $ \eta  < 4.5$

Table A.3: Summary of cuts on jet pseudorapidity and transverse momentum in addition to the jet veto requirements from ATLAS analysis [1]

The relative missing energy,  $p_{\perp, \text{rel}}$  is defined as

$$p_{\perp, \text{rel}}^{\text{miss}} = \left\{ \begin{array}{l} p_\perp^{\text{miss}} \sin(\Delta\phi) \text{ if } \Delta\phi < \frac{\pi}{2} \\ p_\perp^{\text{miss}} \text{ if } \Delta\phi > \frac{\pi}{2} \end{array} \right\} \quad (\text{A.1.2})$$

where  $\Delta\phi$  is the angle between  $p_\perp^{\text{miss}}$  and the nearest lepton or jet and  $p_\perp^{\text{miss}}$  is the sum of all missing transverse momenta.

This definition allows the channel specific cuts to be defined in the table below

The analysis also defines cuts on the specific leptonic decays channels possible for the  $W$  pair, these are simply all the combined individual  $W \rightarrow e\bar{\nu}_e$  and  $W \rightarrow \mu\bar{\nu}_\mu$  decay channels for  $W$  pairs; these cuts are defined in the table below.

	$ee$ channel	$\mu\mu$ channel	$e\mu$ channel
$m_{ll}$	$m_{ll} > 15$ GeV	$m_{ll} > 15$ GeV	$m_{ll} > 10$ GeV
$ m_{ll} - m_z $	$ m_{ll} - m_z  > 15$ GeV	$ m_{ll} - m_z  > 15$ GeV	$ m_{ll} - m_z  > 0$ GeV
$p_{\perp, \text{rel}}^{\text{miss}}$	$p_{\perp, \text{rel}} > 45$ GeV	$p_{\perp, \text{rel}} > 45$ GeV	$p_{\perp, \text{rel}} > 25$ GeV

Table A.4: Summary of channel specific cuts on the mass of leptons pairs and missing energy from ATLAS analysis [1]. The notation ' $e\mu$  channel' defines an event in which the lepton pair has undergone one  $W \rightarrow e\bar{\nu}_e$  and one  $W \rightarrow \mu\bar{\nu}_\mu$  decay

In addition to constraints on various leptonic and jet kinematics, the analysis also requires that the certain leptonic and jet components are clearly separated by certain radius values which if not met cause one or both components to be discarded from the analysis, these are summarised below to be:

- if electrons and a jet are separated by  $\Delta R < 0.3$  the jet is discarded

- if an electrons and muon are separated by  $\Delta R > 0.1$  then the electron is discarded
- For electrons within  $\Delta R > 0.1$  of each other, the lowest  $p_{\perp}$  electron is discarded

## A.2 CMS Drell-Yan Analysis [2, 3]

The results presented in this section give a summary of the analysis used to simulate against Drell-Yan results from CMS using data from 2011 in [2] and 2012 [3], which use a common analysis framework. The results used from these analyses are reconstructed over the entire phase space, and as a result no kinematic cuts are applied in this analysis

The Leptons are also required to obey isolation criteria, for this analysis cuts are placed on the sum of all transverse momenta, with the cone of  $\Delta R < 0.3$  around the proto-lepton, the thresholds are given in the table below.

Electron isolation criteria for transverse momentum	$\sum_{\Delta R < 0.3} p_{\perp} < 0.1 p_{\perp}^{\text{electron}}$
Muon isolation criteria for transverse momentum	$\sum_{\Delta R < 0.3} p_{\perp} < 0.15 p_{\perp}^{\text{muon}}$

Table A.5: Isolation criteria on leptons from CMS analyses [2] and [3]. All isolation criteria are taken within a cone of radius  $\Delta R < 0.3$ .

## A.3 Drell-Yan ATLAS Analysis [4]

The results presented in this section give a summary of the analysis used to simulate against Drell-Yan results from ATLAS as described in [4], unlike the CMS Drell-Yan analyses, this analysis is constrained to measure only electrons. This analysis can, for the purposes of simulating a Monte Carlo comparison, be described by the following set of constraints on lepton kinematics, the electrons are then required to pass a set of isolation criteria; the kinematic constraints are given in the table below.

Electron pseudorapidity	$ \eta  < 2.47$ or $1.52 <  \eta  < 2.47$
Electron $p_{\perp}$ threshold	$p_{\perp} > 25$ GeV

Table A.6: Summary of pseudorapidity and  $p_{\perp}$  cuts on electrons as described by ATLAS analysis [4]

The electrons are also required to obey isolation criteria, for this analysis cuts are placed on the sum of all transverse momenta, with the cone of  $\Delta R < 0.2$  around the proto-electron,

$$\sum_{\Delta R < 0.2} p_{\perp} < 7 \text{ GeV} \quad (\text{A.3.3})$$

The measured data is then extrapolated to the region  $|\eta| \leq 2.5$  and corrected for isolation effects. QED final state radiation off the electrons is treated in two ways: 1) “dressed” leptons, defined through recombination with all photons within  $\Delta R = 0.1$  and 2) “Born” leptons, defined through correcting the data for all final state radiation off the leptons, as extracted from Monte-Carlo modelling. In this thesis, the presented calculation is compared to the data using the “Born” lepton definition.

## A.4 Lepton Pair Jet Analysis

The jet activity plot, shown in figure 9.3 in chapter 9, also contains analysis specific information which requires a description. While this is not an experimental analysis and there is no data compared against, there are choices on jet definitions and isolation which will now be summarised.

- Jets in this analysis are defined to be anti- $k_T$  jets using a radius parameter of the  $R = 0.4$
- Jets are required to have  $p_{\perp} > 20$  GeV
- The jets are required to be separated from the lepton pair by a radius parameter of  $\Delta R > 0.3$ .

The first requirement is required to stop very large jet multiplicities, and is taken from ATLAS jet requirements that are for example defined in [1]. The second requirement is necessary to prevent jets that would, in experimental analysis, become absorbed into lepton momenta by the isolation criteria; the choice of the radius of  $\Delta R > 0.3$  reflects the isolation requirement of the CMS Drell-Yan analysis.

# Appendix B

## FKS Expressions

This appendix simply shows expressions relevant to the FKS subtraction scheme which are not directly included in the text. Principally these are; the integrated soft terms when massive partons are present in the process and the angular components of the collinear limit of the real term.

### B.1 Massive Partons in the Integrated Soft Term

It is recalled that the integrated soft term is given by

$$d\sigma^{(I,S)} = \frac{1}{2} \frac{\alpha_s}{2\pi} \sum_{n \neq m} (\mathcal{I}_{nm}^{\text{div}} + \mathcal{I}_{nm}^{\text{reg}}) d\sigma_{nm}^{(B)} \quad (\text{B.1.1})$$

The result for  $\mathcal{I}_{nm}$  for purely massless partons in the process is quoted in the section 3.1.1, however when massive partons exist in the process, despite their exclusion from being in FKS pairs, they do enter FKS subtraction terms through the soft subtraction term, which includes a double sum over all colour objects. The following expressions involving massive partons can all be found in [36]. For massive  $n$ , with massless  $m$

$$\mathcal{I}_{nm}^{\text{div}} = \frac{(4\pi)^\epsilon}{\Gamma(1-\epsilon)} \left( \frac{\mu^2}{Q^2} \right)^\epsilon \left[ \frac{1}{2\epsilon^2} + \frac{1}{\epsilon} \left( \log \frac{2k_n \cdot k_m}{Q^2} - \frac{1}{2} \log \frac{4m_n^2 E_m^2}{\xi_{\text{cut}}^2 s Q^2} \right) \right] \quad (\text{B.1.2})$$

$$\begin{aligned} \mathcal{I}_{nm}^{\text{reg}} = & \log \xi_{\text{cut}} \left( \log \frac{\xi_{\text{cut}} s}{Q^2} + 2 \log \frac{k_n \cdot k_m}{m_n E_m} \right) - \frac{\pi^2}{12} + \frac{1}{4} \log^2 \frac{s}{Q^2} \\ & - \frac{1}{4} \log^2 \frac{1 + \beta_n}{1 - \beta_n} + \frac{1}{2} \log^2 \frac{k_n \cdot k_m}{(1 - \beta_n) E_n E_m} + \log \frac{s}{Q^2} \log \frac{k_n \cdot k_m}{m_n E_m} \\ & - \text{Li}_2 \left( 1 - \frac{(1 + \beta_n) E_n E_m}{k_n \cdot k_m} \right) + \text{Li}_2 \left( 1 - \frac{k_n \cdot k_m}{(1 - \beta_n) E_n E_m} \right) \end{aligned}$$

For massive  $n$  and  $m$

$$\mathcal{I}_{nm}^{\text{div}} = \frac{(4\pi)^\epsilon}{\Gamma(1 - \epsilon)} \left( \frac{\mu^2}{Q^2} \right)^\epsilon \left( -\frac{1}{2\epsilon} \frac{1}{v_{nm}} \log \frac{1 + v_{nm}}{1 - v_{nm}} \right) \quad (\text{B.1.3})$$

$$\begin{aligned} \mathcal{I}_{nm}^{\text{reg}} = & \frac{1}{2v_n m} \log \frac{1 + v_{nm}}{1 - v_{nm}} \log \frac{\xi_{\text{cut}}^2 s}{Q^2} + \frac{(1 + v_{nm})(k_n \cdot k_m)^2}{2m_n^2} (J^{(A)}(\alpha_{nm} E_n, \alpha_{nm} E_n, \beta_n) \\ & - J^{(A)}(E_m, E_m, \beta_m)) \end{aligned}$$

$$J^{(A)}(x, y) = \frac{1}{2\lambda\nu} \left[ \log^2 \frac{x - y}{x + y} + 4\text{Li}_2 \left( 1 - \frac{x + y}{\mu} \right) + 4\text{Li}_2 \left( 1 - \frac{x - y}{\mu} \right) \right] \quad (\text{B.1.4})$$

$$v_{nm} = \sqrt{1 - \left( \frac{m_n m_m}{k_n k_m} \right)^2} \quad (\text{B.1.5})$$

$$\alpha_{nm} = \frac{1 + \mu_{nm}}{m_n^2} k_n \cdot k_m \quad (\text{B.1.6})$$

$$\lambda = \alpha_{nm} E_n - E_m \quad (\text{B.1.7})$$

$$\mu = \frac{\alpha_{nm} m_n^2 - m_m^2}{2\lambda} \quad (\text{B.1.8})$$

The self eikonal piece,  $\mathcal{I}_{nn}$  which only exists in the massive case is given by

$$\mathcal{I}_{nn}^{\text{div}} = \frac{(4\pi)^\epsilon}{\Gamma(1 - \epsilon)} \left( -\frac{1}{\epsilon} \right) \quad (\text{B.1.9})$$

$$\mathcal{I}_{nn}^{\text{reg}} = \log \frac{\xi_{\text{cut}}^2 s}{Q^2} - \frac{1}{\beta_n} \log \frac{1 + \beta_n}{1 - \beta_n} \quad (\text{B.1.10})$$

## B.2 The Reduced Matrix element from Collinear Limits

In FKS subtraction, the collinear limit is used for the collinear subtraction term. For a collinear limit of 2 particles  $i, j$  with momenta  $k_i, k_j$

$$\lim_{k_i \parallel k_j} \mathcal{M}^{(n+1)}(\{k\}_{n+1}) = \frac{4\pi\alpha_s}{k_i \cdot k_j} P_{a_j a_{ij}}(z) \mathcal{M}^{(n)}(r_{[i]}^{a_{ij}}, \{\hat{k}\}_n) + \frac{4\pi\alpha_s}{k_i \cdot k_j} Q_{a_j a_{ij}}(z) \tilde{\mathcal{M}}^{(n)}(r_{[i]}^{a_{ij}}, \{\hat{k}\}_n) \quad (\text{B.2.11})$$

Where

$$\tilde{\mathcal{M}}(r_{[i]}^{a_{ij}}, \{\hat{k}\}_n) = \frac{1}{2s} \frac{1}{\omega(a_1)\omega(a_2)} \text{Re} \left[ \frac{\langle k_i k_j \rangle}{[k_i k_j]} \sum_{c,s} \mathcal{A}_+ \left( r_{[i]}^{a_{ij}} \right) \mathcal{A}_-^* \left( r_{[i]}^{a_{ij}} \right) \right] \quad (\text{B.2.12})$$

where  $\mathcal{A}_{+/-} \left( r_{[i]}^{a_{ij}} \right)$  is understood to mean the helicity of parton  $a_{ij}$  is + or -. Where  $\langle k_i k_j \rangle$  and  $[k_i k_j]$  are spinor products, with definitions of these spinor products (for Dirac spinors) given in [89] it is fairly trivial to obtain the collinear limit of this ratio.

# Bibliography

- [1] ATLAS Collaboration, G. Aad *et al.*, (2013), 1304.7098.
- [2] S. Chatrchyan and others".
- [3] CMS Collaboration, (2012).
- [4] ATLAS Collaboration, G. Aad *et al.*, (2013), 1305.4192.
- [5] ATLAS Collaboration, G. Aad *et al.*, Phys.Rev. **D87**, 112001 (2013), 1210.2979.
- [6] F. Krauss, R. Kuhn, and G. Soff, JHEP **02**, 044 (2002), hep-ph/0109036.
- [7] M. E. Peskin and D. V. Schroeder, 1995 Westview Press. .
- [8] S. Weinberg., Cambridge University Press, 1996 .
- [9] W. J. S. R. Keith Ellis and B. R. Webber., Cambridge University Press, 1996 .
- [10] S. Frixione, Z. Kunszt, and A. Signer, Nucl.Phys. **B467**, 399 (1996), hep-ph/9512328.
- [11] S. Catani and M. Grazzini, Nucl.Phys. **B570**, 287 (2000), hep-ph/9908523.
- [12] J. C. Collins and D. E. Soper, Ann.Rev.Nucl.Part.Sci. **37**, 383 (1987).
- [13] G. Altarelli and G. Parisi, Nucl. Phys. **B126**, 298 (1977).
- [14] Y. L. Dokshitzer, Sov. Phys. JETP **46**, 641 (1977).
- [15] V. N. Gribov and L. N. Lipatov, Sov. J. Nucl. Phys. **15**, 438 (1972).

- 
- [16] P. M. Stevenson, Phys. Rev. D **23**, 2916 (1981).
- [17] G. Grunberg, Phys. Rev. D **29**, 2315 (1984).
- [18] G. F. Sterman and S. Weinberg, Phys.Rev.Lett. **39**, 1436 (1977).
- [19] G. P. Salam, Eur. Phys. J. **C67**, 637 (2010), 0906.1833.
- [20] S. D. Ellis and D. E. Soper, Phys.Rev. **D48**, 3160 (1993), hep-ph/9305266.
- [21] S. Catani, Y. L. Dokshitzer, M. Seymour, and B. Webber, Nucl.Phys. **B406**, 187 (1993).
- [22] M. Wobisch and T. Wengler, (1998), hep-ph/9907280.
- [23] Y. L. Dokshitzer, G. Leder, S. Moretti, and B. Webber, JHEP **9708**, 001 (1997), hep-ph/9707323.
- [24] M. Cacciari, G. P. Salam, and G. Soyez, JHEP **0804**, 063 (2008), 0802.1189.
- [25] T. Kinoshita, J.Math.Phys. **3**, 650 (1962).
- [26] T. Lee and M. Nauenberg, Phys.Rev. **133**, B1549 (1964).
- [27] R. K. Ellis and J. Sexton, Nucl.Phys. **B269**, 445 (1986).
- [28] S. Catani, Phys.Lett. **B427**, 161 (1998), hep-ph/9802439.
- [29] B. Potter, (1997).
- [30] B. Harris and J. Owens, Phys.Rev. **D65**, 094032 (2002), hep-ph/0102128.
- [31] G. Heinrich, Int.J.Mod.Phys. **A23**, 1457 (2008), 0803.4177.
- [32] S. Catani and M. Seymour, Nucl.Phys. **B485**, 291 (1997), hep-ph/9605323.
- [33] S. Catani, S. Dittmaier, M. H. Seymour, and Z. Trocsanyi, Nucl.Phys. **B627**, 189 (2002), hep-ph/0201036.
- [34] S. Frixione, Nucl.Phys. **B507**, 295 (1997), hep-ph/9706545.

- 
- [35] S. Alioli, P. Nason, C. Oleari, and E. Re, *JHEP* **1006**, 043 (2010), 1002.2581.
- [36] R. Frederix, S. Frixione, F. Maltoni, and T. Stelzer, *JHEP* **0910**, 003 (2009), 0908.4272.
- [37] T. Gleisberg *et al.*, *JHEP* **0402**, 056 (2004), hep-ph/0311263.
- [38] S. Frixione, E. Laenen, P. Motylinski, and B. R. Webber, *JHEP* **0603**, 092 (2006), hep-ph/0512250.
- [39] T. Gleisberg and F. Krauss, *Eur.Phys.J.* **C53**, 501 (2008), 0709.2881.
- [40] S. Frixione, P. Nason, and C. Oleari, *JHEP* **0711**, 070 (2007), 0709.2092.
- [41] C. Chung, M. Kramer, and T. Robens, *JHEP* **1106**, 144 (2011), 1012.4948.
- [42] CMS Collaboration, (2009).
- [43] M. Czakon and A. Mitov, *JHEP* **1212**, 054 (2012), 1207.0236.
- [44] Y. Li and F. Petriello, *Phys.Rev.* **D86**, 094034 (2012), 1208.5967.
- [45] E. Accomando, A. Denner, and A. Kaiser, *Nucl.Phys.* **B706**, 325 (2005), hep-ph/0409247.
- [46] A. D. Martin, R. G. Roberts, W. J. Stirling, and R. S. Thorne, *Eur. Phys. J.* **C39**, 155 (2005), hep-ph/0411040.
- [47] The NNPDF Collaboration, R. D. Ball *et al.*, (2013), 1308.0598.
- [48] V. M. Budnev, I. F. Ginzburg, G. V. Meledin, and V. G. Serbo, *Phys. Rept.* **15**, 181 (1974).
- [49] T. Gleisberg and S. Höche, *JHEP* **12**, 039 (2008), 0808.3674.
- [50] R. Kleiss and W. J. Stirling, *Nucl. Phys.* **B262**, 235 (1985).
- [51] A. Ballestrero, E. Maina, and S. Moretti, *Nucl. Phys.* **B415**, 265 (1994), hep-ph/9212246.

- 
- [52] H. Murayama, I. Watanabe, and K. Hagiwara, (1992).
- [53] F. A. Berends and W. T. Giele, Nucl. Phys. **B306**, 759 (1988).
- [54] F. A. Berends and W. Giele, Nucl. Phys. **B294**, 700 (1987).
- [55] R. Kleiss and H. Kuijf, Nucl. Phys. **B312**, 616 (1989).
- [56] M. L. Mangano, M. Moretti, F. Piccinini, R. Pittau, and A. D. Polosa, JHEP **07**, 001 (2003), hep-ph/0206293.
- [57] R. Kleiss and R. Pittau, Comput. Phys. Commun. **83**, 141 (1994), hep-ph/9405257.
- [58] Z. Nagy and D. E. Soper, JHEP **0510**, 024 (2005), hep-ph/0503053.
- [59] S. Schumann and F. Krauss, JHEP **0803**, 038 (2008), 0709.1027.
- [60] M. Dinsdale, M. Ternick, and S. Weinzierl, Phys. Rev. **D76**, 094003 (2007), 0709.1026.
- [61] S. Catani, F. Krauss, R. Kuhn, and B. R. Webber, JHEP **11**, 063 (2001), hep-ph/0109231.
- [62] L. Lönnblad, JHEP **05**, 046 (2002), hep-ph/0112284.
- [63] S. Höche, F. Krauss, S. Schumann, and F. Siegert, JHEP **05**, 053 (2009), 0903.1219.
- [64] S. Frixione and B. R. Webber, JHEP **0206**, 029 (2002), hep-ph/0204244.
- [65] S. Hoeche, F. Krauss, M. Schonherr, and F. Siegert, JHEP **1209**, 049 (2012), 1111.1220.
- [66] T. D. Gottschalk, Nucl. Phys. **B239**, 349 (1984).
- [67] B. R. Webber, Nucl. Phys. **B238**, 492 (1984).

- 
- [68] J.-C. Winter, F. Krauss, and G. Soff, *Eur. Phys. J.* **C36**, 381 (2004), hep-ph/0311085.
- [69] A. Buckley *et al.*, *Phys.Rept.* **504**, 145 (2011), 1101.2599.
- [70] C. Balazs, J. Huston, and I. Puljak, *Phys.Rev.* **D63**, 014021 (2001), hep-ph/0002032.
- [71] T. Sjostrand, *Phys.Lett.* **B157**, 321 (1985).
- [72] H.-U. Bengtsson and T. Sjostrand, *Comput.Phys.Commun.* **46**, 43 (1987).
- [73] T. Sjostrand and P. Z. Skands, *Eur.Phys.J.* **C39**, 129 (2005), hep-ph/0408302.
- [74] S. Gieseke, P. Stephens, and B. Webber, *JHEP* **0312**, 045 (2003), hep-ph/0310083.
- [75] G. Marchesini and B. Webber, *Phys.Rev.* **D38**, 3419 (1988).
- [76] Z. Nagy and D. E. Soper, p. 101 (2006), hep-ph/0601021.
- [77] P. Nason, *JHEP* **0411**, 040 (2004), hep-ph/0409146.
- [78] T. Sjostrand, S. Mrenna, and P. Z. Skands, *JHEP* **0605**, 026 (2006), hep-ph/0603175.
- [79] S. Platzer and M. Sjodahl, *Eur.Phys.J.Plus* **127**, 26 (2012), 1108.6180.
- [80] S. Hoche, F. Krauss, M. Schonherr, and F. Siegert, *JHEP* **1108**, 123 (2011), 1009.1127.
- [81] K. Hamilton and P. Nason, *JHEP* **06**, 039 (2010), 1004.1764.
- [82] M. R. Whalley, D. Bourilkov, and R. C. Group, (2005), hep-ph/0508110.
- [83] M. H. Seymour, *Z. Phys.* **C56**, 161 (1992).
- [84] E. Fermi, *Z.Phys.* **29**, 315 (1924).
- [85] C. von Weizsacker, *Z.Phys.* **88**, 612 (1934).

- [86] E. Williams, Phys.Rev. **45**, 729 (1934).
- [87] A. Buckley *et al.*, (2010), 1003.0694.
- [88] J. M. Campbell and R. Ellis, Nucl.Phys.Proc.Suppl. **205-206**, 10 (2010), 1007.3492.
- [89] L. J. Dixon, (1996), hep-ph/9601359.